NASA CR-187120

NASA

AN EXPERIMENTAL INVESTIGATION OF HOLLOW CATHODE-BASED PLASMA CONTACTORS

Prepared for

LEWIS RESEARCH CENTER

NATIONAL AERONAUTICS AND SPACE ADMINISTRATION

Grant NAG 3-776

by

John D. Williams

May 1991

Approved by

Paul J. Wilbur
Department of Mechanical Engineering
Colorado State University
Fort Collins, Colorado 80523

NASA
National Aeronautics and Space Administration

Report Documentation Page

1. Report No.	2. Government Accession No.	3. Recipient's Catalog No.
CR 187120		

4. Title and Subtitle

AN EXPERIMENTAL INVESTIGATION OF HOLLOW CATHODE-BASED PLASMA CONTACTORS

5. Report Date
May 1991

6. Performing Organization Code

7. Author(s)

John D. Williams

8. Performing Organization Report No.

10. Work Unit No.

9. Performing Organization Name and Address

Department of Mechanical Engineering
Colorado State University
Fort Collins, CO 80523

11. Contract or Grant No.
NAG 3-776

13. Type of Report and Period Covered

12. Sponsoring Agency Name and Address

National Aeronautics and Space Administration
Washington, D.C. 20546

14. Sponsoring Agency Code

15. Supplementary Notes

Grant Monitor-Joel T. Galofaro, NASA Lewis Research Center, Cleveland, Oh 44135
This report is a reproduction of the Ph.D. dissertation of John Williams. It is submitted to the sponsor and the distribution list in this form both as a presentation of the technical material and as an indication of the academic program supported by the grant.

16. Abstract

Experimental results are presented which describe operation of and the plasma environment associated with a hollow cathode-based plasma contactor collecting electrons from or emitting them to an ambient, low density Maxwellian plasma. A one-dimensional, phenomenological model of the near-field electron collection process, which was formulated from experimental observations, is presented. It considers three regions, namely, a plasma cloud adjacent to the contactor, an ambient plasma from which electrons are collected, and a double layer region that develops between the contactor plasma cloud and the ambient plasma regions. Results of electron emission experiments are also presented. An important observation is made using a retarding potential analyzer (RPA) which shows that high energy ions generally stream from a contactor along with the electrons being emitted. A mechanism for this phenomenon is presented and it involves a high rate of ionization induced between electrons and atoms flowing together from the hollow cathode orifice. This can result in the development of a region of high positive space change and, therefore, high positive potential. Langmuir and RPA probe data suggest that both electrons and ions expand spherically from this hill region. In addition to experimental observations, a one-dimensional model which describes the electron emission process and predicts the phenomena just mentioned is presented and shown to agree qualitatively with these observations.

17. Key Words (Suggested by Author(s))	18. Distribution Statement
Plasma Contactor Hollow Cathode Double Layer	Unclassified - Unlimited

19. Security Classif. (of this report)	20. Security Classif. (of this page)	21. No of pages	22. Price*
Unclassified	Unclassified	114	

NASA FORM 1626 OCT 86

*For sale by the National Technical Information Service, Springfield, Virginia 22161

TABLE OF CONTENTS

LIST OF FIGURES

LIST OF TABLES

I. INTRODUCTION

A plasma contactor is a plasma producing device that enhances the ability of a spacecraft to emit or collect electrons and ions from a surrounding plasma environment. The fundamental expectation that an enhancement will occur is related to the ability of a cool, relatively high density plasma cloud to reduce the space-charge limitations of current flow from the spacecraft. The plasma cloud can eliminate the hazards of a natural spacecraft charging event (both net and differential charging) [1,2] by emitting or collecting a modest electron current. In addition when larger return currents are required, the plasma cloud can expand and thereby increase the effective charged particle collection area of the spacecraft/plasma contactor system. Examples of critical applications of plasma contactors, in which large voltage drops between the contactor and ambient plasma could be particularly undesirable include those involving electrodynamic tethers [3] and spacecraft from which high current, high energy charged particle beams are being ejected [1]. In the case of an electrodynamic tether system where two satellites joined by a connecting tether are involved, a plasma contactor may be placed on each satellite to facilitate connections to the local ionospheric plasma. In addition to the potential drops which can occur at both ends of the tether (between the contactors and local ionospheric plasma) under the imposed current flow, a potential drop can occur through the geo-scale plasma separating the two satellites. However, the work that is presented concentrates only

on the phenomena which occur near each contactor and can be readily studied in modest ground-based vacuum facilities. The question of current closure through the geo-scale plasma is not addressed.

A relatively simple plasma contactor can be based on the hollow cathode--a device derived from ion thruster neutralization applications. The hollow cathode plasma source is well suited to charge control applications because of its robust construction and long lifetime characteristics, high electron emission current capabilities (in excess of 60 A [4]), low power requirements and capacity to produce a cool, neutral plasma. The work presented here will focus on the operation of the hollow cathode device as a plasma contactor. The objective of the presentation will be to describe ground-based experiments and then develop or utilize existing models to explain the important processes that determine the effectiveness of the device.

The most basic ground-based experiments involve biasing a plasma contactor and its associated plasma cloud with respect to an ambient plasma and measuring the current which is conducted under this applied voltage. Two entirely different modes of contactor operation which will be discussed are 1) those that involve biasing the contactor plasma cloud positive and attempting to collect electrons from a surrounding ambient plasma and 2) those that involve biasing the contactor plasma cloud negative and emitting electrons to a surrounding ambient plasma. Fictitious current/voltage characteristic curves, which demonstrate ideal and non-ideal plasma contactor performance, are shown in Fig. 1-1. The contactor potential, plotted on the abscissa in Fig. 1-1, is defined as the potential difference between the contactor and the ambient plasma. The electron emission current is plotted on the coordinate,

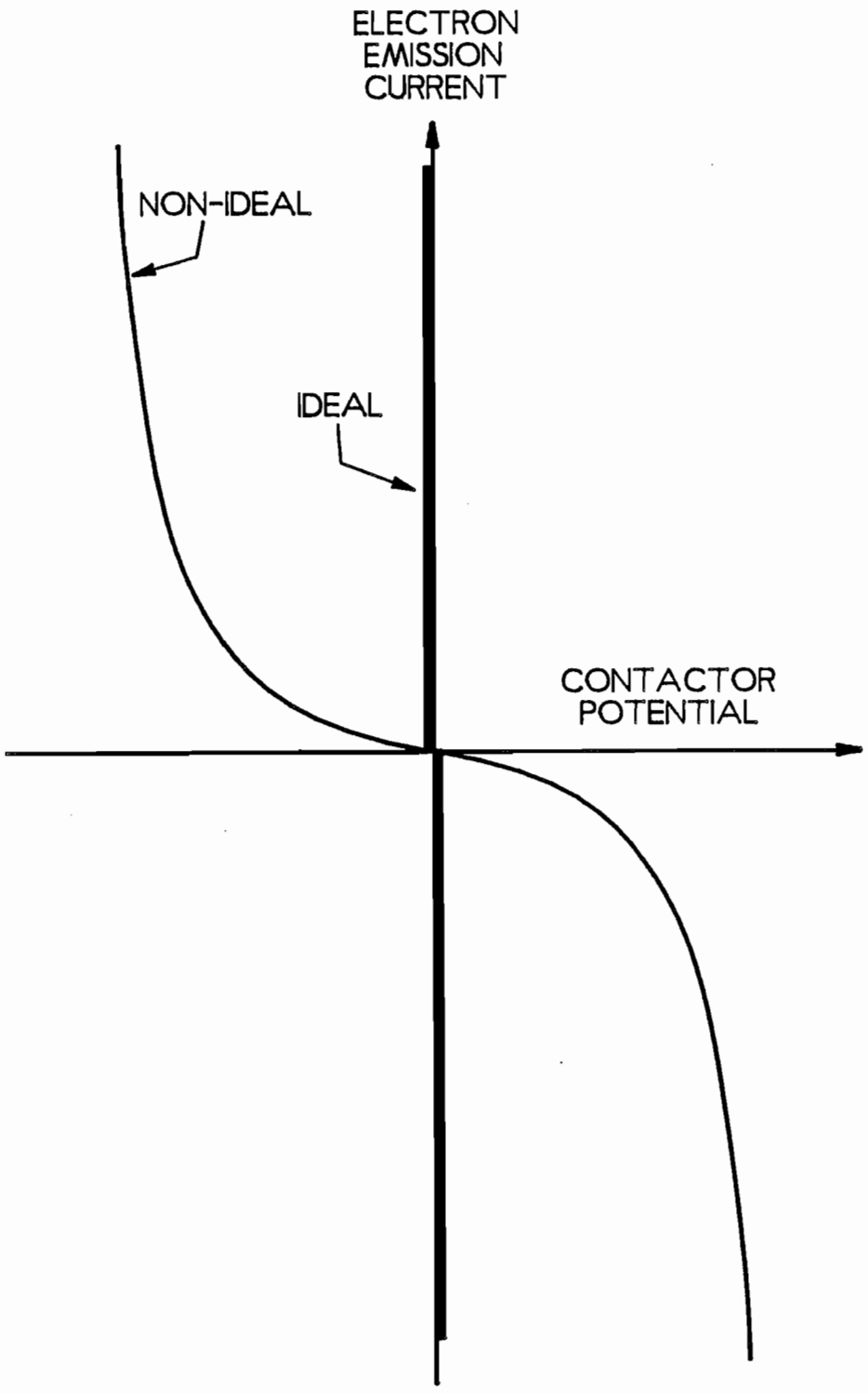

Fig. 1-1 Imaginary Contactor Performance Curves Showing Ideal and Non-Ideal Behavior

and positive and negative values correspond to electron emission and electron collection operation, respectively. The curve labelled "ideal" suggests that only small negative contactor potentials are required to emit large currents and small positive potentials to collect large currents. On the other hand, the curve labelled "non-ideal" suggests that larger contactor potential magnitudes are required at every electron emission current condition. Specifically, poorer performance is indicated in Fig. 1-1 by shifting the curve corresponding to electron collection (4th quadrant) to higher contactor potentials and by shifting the curve corresponding to electron emission (2nd quadrant) to more negative contactor potentials.

Ground-based experiments suggest that a double layer will form between the ambient plasma and the contactor plasma cloud when the contactor is collecting electrons [5,6,7]. Typically, the contactor plasma cloud potential is close to the contactor anode potential and, consequently, the voltage drop experienced across the double layer constitutes a large fraction of the potential difference between the contactor and the ambient plasma. A double layer is essentially two adjacent layers of charge; one, a positive layer at the edge of the high potential plasma (the contactor plasma cloud) and the other negative layer at the edge of the low potential plasma (the ambient plasma). The substantial voltage drops which can develop across this double layer region are generally undesirable because they represent a failure of the plasma contactor to collect electrons efficiently from the ambient plasma.

A thorough review of basic experimental and theoretical work on double layers is given by Hershkowitz [8], and it is interesting to compare this work with double layers observed in plasma contactor experiments. For the most part, double layer

experiments have been conducted in triple plasma devices, but many double layer experiments have also been conducted in discharge tubes and Q-machines (see also [8] and references therein). The triple plasma device consists of two plasma sources (typically equipped with fine wire plasma extraction grids) and a target region. The two plasma sources face each other and are separated by the target region. When the two sources are biased with respect to one another and the amount of plasma released by each is controlled, it is possible to form a double layer (sometimes more than one) in the target region. In general, the results of these tests and theoretical studies have shown that a minimum of four species of particles are involved in stable double layers. These four species include ions and electrons that are accelerated through the double layer from the high and low potential plasmas, respectively ("free" particles); and ions and electrons that are reflected from the double layer and (generally) remain in the low and high potential plasmas, respectively ("trapped" particles).

The study of double layers and their formation has generally been motivated by the postulate that double layer structures formed in the magnetosphere generate high energy electron beams which are responsible for auroral displays. In order to study this proposal, many researchers turned to the triple plasma device for reasons that reflect its 1) relatively simple operation, 2) provisions for some control over the distribution of trapped and free particles, and 3) low target-region plasma densities which ensure rather large double layers (several cm in extent). Most of these researchers have been interested in classifying the high and low potential plasmas in terms of distribution functions which describe the electrons and ions present there and then working out models that describe double layer phenomena [8,9,10,11,12].

Unfortunately, few double layer researchers are interested in the magnitudes of the currents or current densities that flow between the high and low potential plasmas at current levels and potential differences typical of plasma contacting applications. In fact the currents that flow or the effective impedance between the two plasmas is typically not given, and in one double layer experiment potential structures have been observed when no net current was flowing through the double layer region [13]. Consequently, much of this work cannot be applied directly to quantify the performance of a plasma contactor.

However, the phenomena inherent in plasma contactor experiments in which double layers are observed have also been observed in triple plasma experiments. For example, plasma property data taken in the contactor plasma cloud have indicated the presence of a high energy electron beam [5]. This beam forms because ambient plasma electrons are accelerated through the double layer into the contactor plasma cloud region. In addition, high energy ions are detected in the ambient plasma. These ions are presumably accelerated through the double layer from the plasma cloud and into the ambient plasma. Due to the presence of electron and ion beams in the high and low potential plasmas, various plasma instabilities can occur, grow, and cause these plasmas to be turbulent. Some double layer researchers have looked at electrostatic fluctuation spectra and found that, typically, low frequency ion-acoustic (ion beam- or possibly drifting electron-induced) instabilities are present in the low potential plasma, while high frequency electron-beam instabilities affect the high potential plasma [8,9]. These instabilities can cause the high and low plasmas to be very turbulent. Some experimental studies have indicated that the turbulence intensity

and its spectral distribution are important in determining the formation and characteristics of double layers (since the presence of strong turbulence in the high and low potential plasmas can increase effective collision frequencies) and other studies have indicated that turbulence in the low and high potential plasmas does not affect the double layer [8,12]. Regardless of its importance in double layer phenomena, turbulent fluctuations in plasma properties can affect the accuracy and reliability of plasma diagnostics. It has generally been found that emissive probes [8,14] yield the most accurate plasma potentials. Typically the plasma potential is found using the emissive probe and then Langmuir probes are used to determine electron densities and temperatures. In addition to emissive and Langmuir probes, retarding potential analyzers [10] have been used to measure the characteristics of the ions and electrons in the high and low potential plasmas. All of these probes can be affected by the noise levels present in a plasma; more details concerning these affects are contained in Appendix A.

The contactor double layer potential drop and position have been observed to be affected by contactor flowrate, anode size, and electron collection current; and double layer potential drops measured under typical experimental conditions have been in the range from 10 to 80 V [15]. Typically, the electron temperature in the contactor plasma cloud is about 3 eV, and when this temperature is used to non-dimensionalize the double layer potential drop (i.e. $\Delta\phi = eV_i/kT_{ei}$) values of double layer strength ($\Delta\phi$) ranging from 3 to 25 have been observed. This strength range has been classified by Hershkowitz [8] as weak (< 10) to strong (> 10). In addition to the properties listed above, plasma densities on the high potential side of the double

layer have been observed to be higher than those on the low potential side. This property of plasma density enhancement across double layers has been observed by many other researchers [8,9,10,12] and it suggests that the double layer boundaries between the high and low potential plasmas are oriented like two spoons fitted front to back with their focal points on the side of the high potential plasma.

In addition to experimental studies of plasma contactors, there are several theoretical studies [16,17,18] that have focused on the problem of controlling spacecraft electric potential with respect to an adjacent environment using plasma producing devices. Most of this work concentrates on the processes that occur at the positively biased "plasma contactor" (i.e. the one collecting electrons from and emitting ions to the space plasma); and little attention has been given to the negatively biased contactor that emits electrons. A chapter of this thesis addresses this deficiency by focusing on the processes that occur near a plasma contactor emitting electrons to a simulated space plasma in a laboratory environment. Observations of the particles coming from a contactor emitting electrons made using a retarding potential analyzer (RPA) show that relatively high energy ions stream away along with the electrons being emitted. A mechanism is postulated that could explain this observation--an important part of the mechanism is the high rate of ionization that occurs when atoms and electrons are expelled simultaneously through a small orifice as they are in a hollow cathode discharge [4,19]. A similar mechanism for the creation of high energy ions has also been proposed by investigators [20,21] studying various electric arcs. The electron emission process chapter describes recent results obtained from experiments conducted on a hollow cathode emitting a net electron

current to a surrounding ambient plasma and presents a first order, one-dimensional model of the process.

II. APPARATUS AND PROCEDURES

A simplified schematic of a hollow cathode-based plasma contactor is shown in Fig. 2-1. The contactor utilizes a 6.4 mm dia. hollow cathode tube that contains an electron emitting insert fabricated by rolling 0.013 mm thick tantalum foil into the shape of a hollow cylinder and treating it with a low work function coating (containing a double carbonate [$BaCO_3$, $SrCO_3$]). An orifice plate with a ~ 1 mm dia. orifice caps the downstream end of the hollow cathode tube. The contactor anode is constructed of a stainless steel flat plate with a 1 cm O.D./0.5 cm I.D., toroidal tantalum insert positioned near its center. The tantalum anode insert is aligned with the hollow cathode orifice and positioned ~ 2 mm downstream of it. The diameter of the stainless steel flat plate anode can be adjusted to 1, 3, 7, or 12 cm. A discharge is initiated between the anode and cathode by flowing xenon through the hollow cathode, applying power to the heater to raise the insert temperature to ~ 1100 K and applying a bias to the anode of a few hundred volts. Once the insert begins to emit electrons, a dense plasma forms within the cathode and a discharge is established between this plasma and the anode through the orifice. As suggested in Fig. 2-1, the electrons accelerated from the plasma in the interior of the cathode and through the orifice can ionize neutral atoms downstream of the orifice and generate a second plasma, which is essential to the plasma contacting process. A

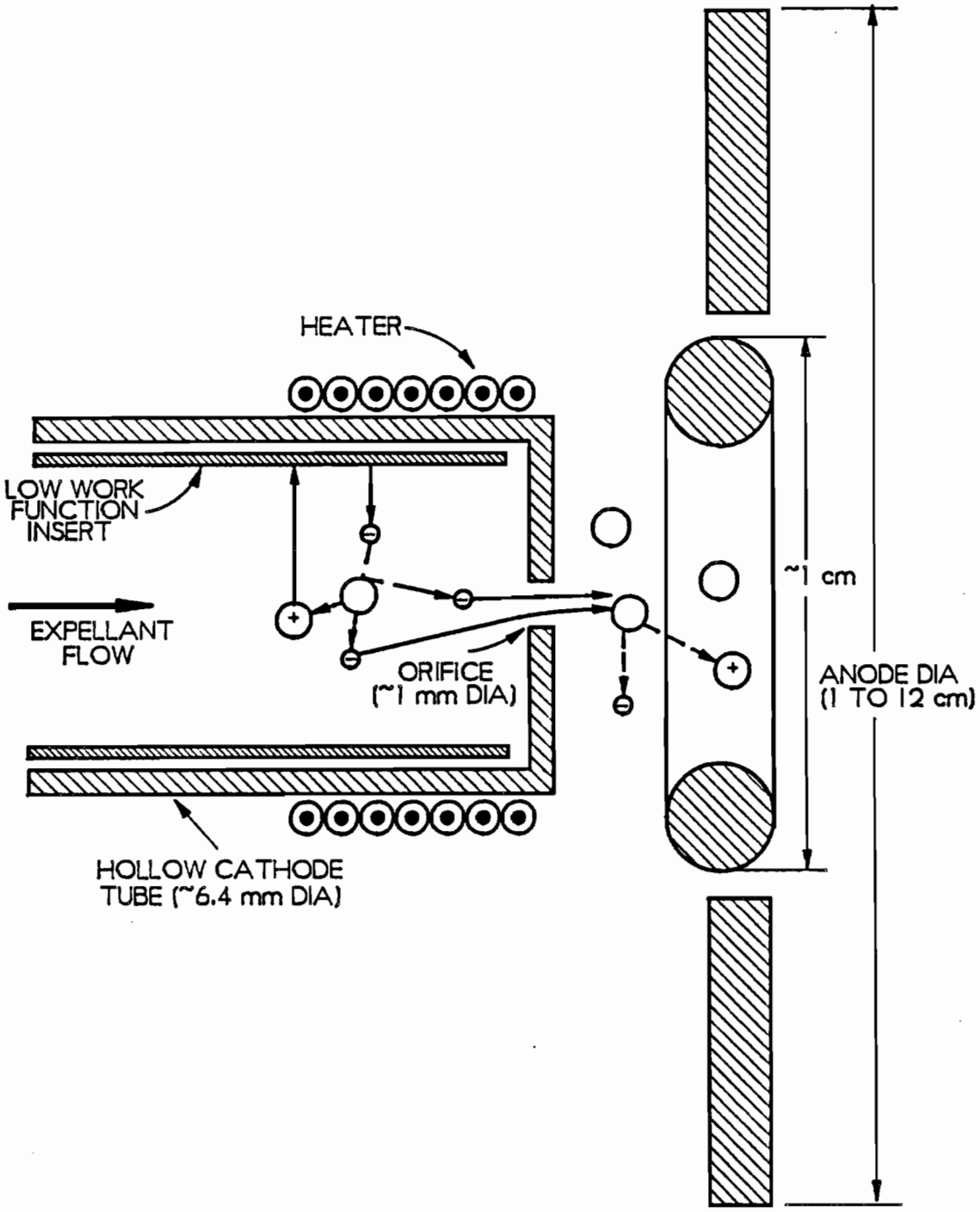

Fig. 2-1 Simplified Schematic of a Hollow Cathode-Based Plasma Contactor

more detailed study and review of orificed hollow cathode operation is presented in Ref. [19].

In order to study the plasma contacting process, the apparatus shown schematically in Figs. 2-2 and 2-3 was constructed. Physically this apparatus consists of two plasma producing devices. The one shown at the right and labeled "simulator" generates a simulated ionospheric plasma. The other device, shown on the left and labeled "plasma contactor", is the focus of study. It is biased relative to the ambient plasma to induce electron emission or electron collection. Also shown are the power supplies and instrumentation needed to sustain and measure the characteristics of the plasmas produced. The simulator and contactor devices are separated by 2.7 m and are located within a 1.2 m dia. by 5.3 m long stainless steel vacuum chamber.

The simulator indicated schematically in Figs. 2-2 and 2-3, which resembles a ring-cusp ion source used in ion thruster applications [22], is shown in more detail in Fig. 2-4a. Plasma is generated within it by collisions between energetic discharge electrons and neutral atoms. In order to increase the efficiency of this process, magnetic fields are used to shield anode surfaces and chamber walls against direct loss of discharge electrons. The ring-cusp magnetic field used in the simulator is induced by samarium cobalt magnets. In order to ensure good coupling between the plasma produced within the source and the ambient plasma region, the device was operated without plasma extraction grids. The simulator is equipped with a tungsten wire cathode which is stretched diagonally across the 9.2 cm dia. open end of the source. When it is heated to thermionic emission temperatures it emits electrons that are eventually collected at the simulator body, which serves as the anode for this

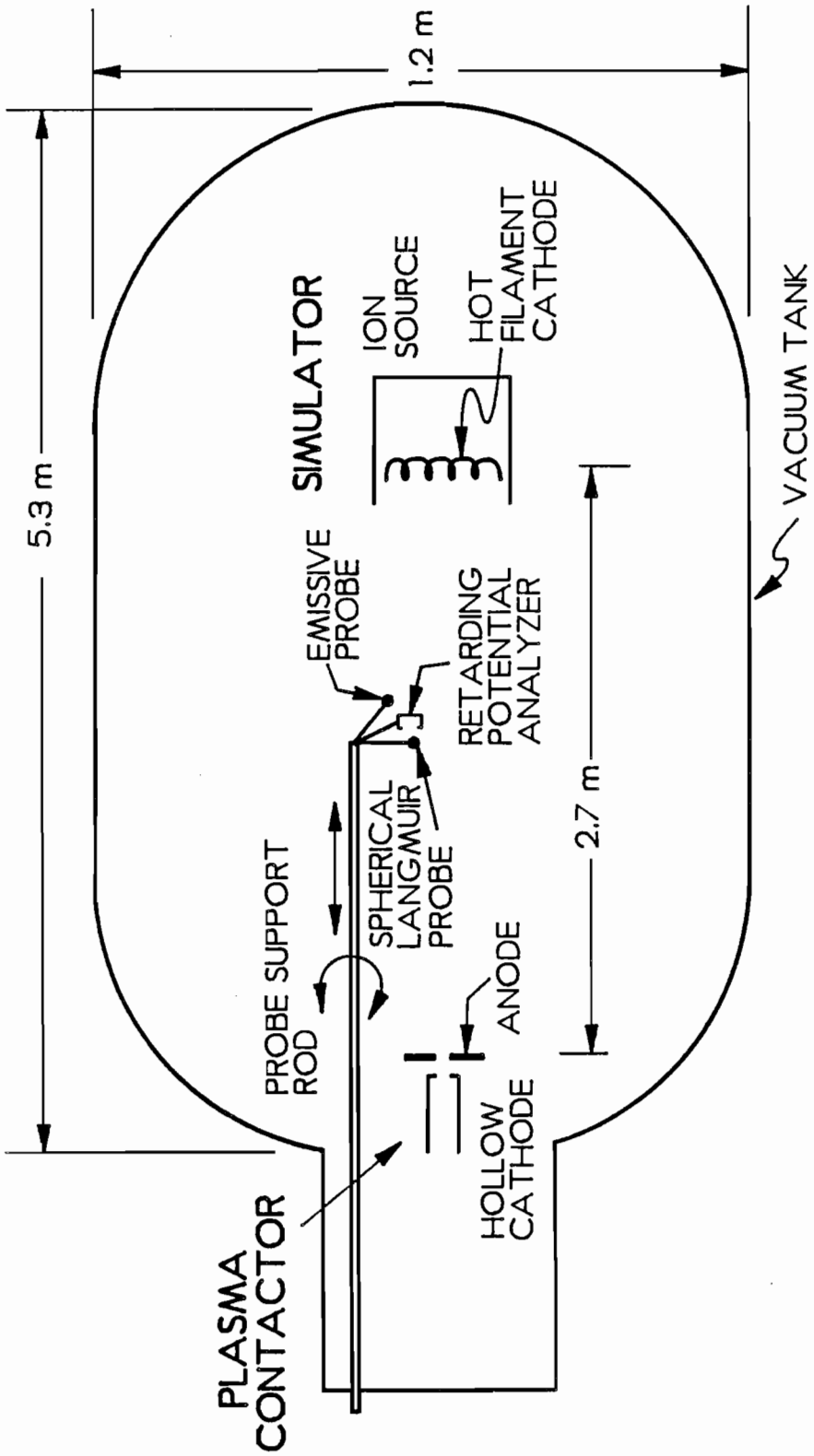

Fig. 2-2 Vacuum Tank Facility Equipped with Plasma Contactor, Simulator, and Plasma Diagnostic Probes

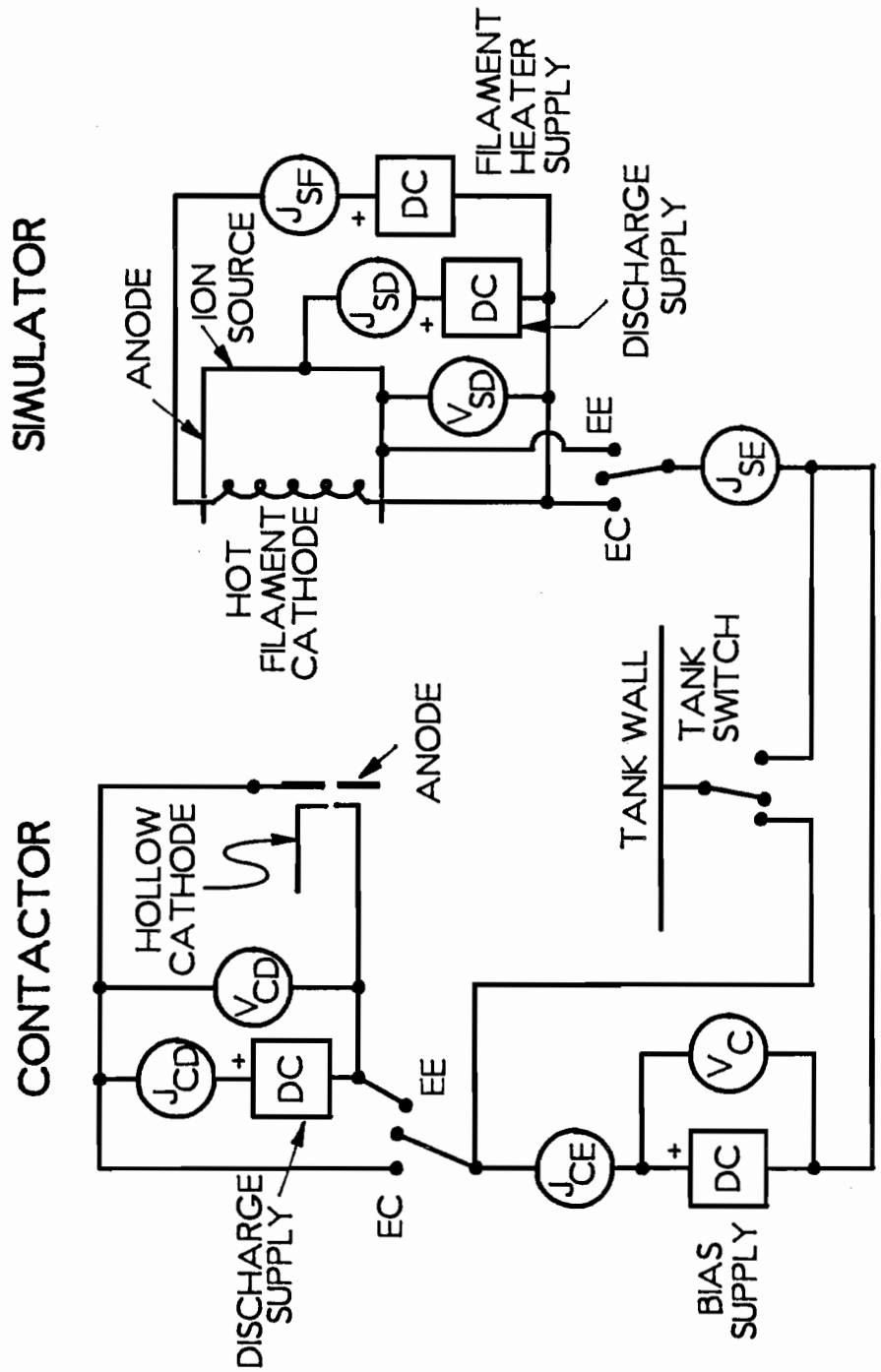

Fig. 2-3 Electrical Schematic Showing how the Plasma Contactor is Biased with Respect to the Vacuum Tank and Simulator

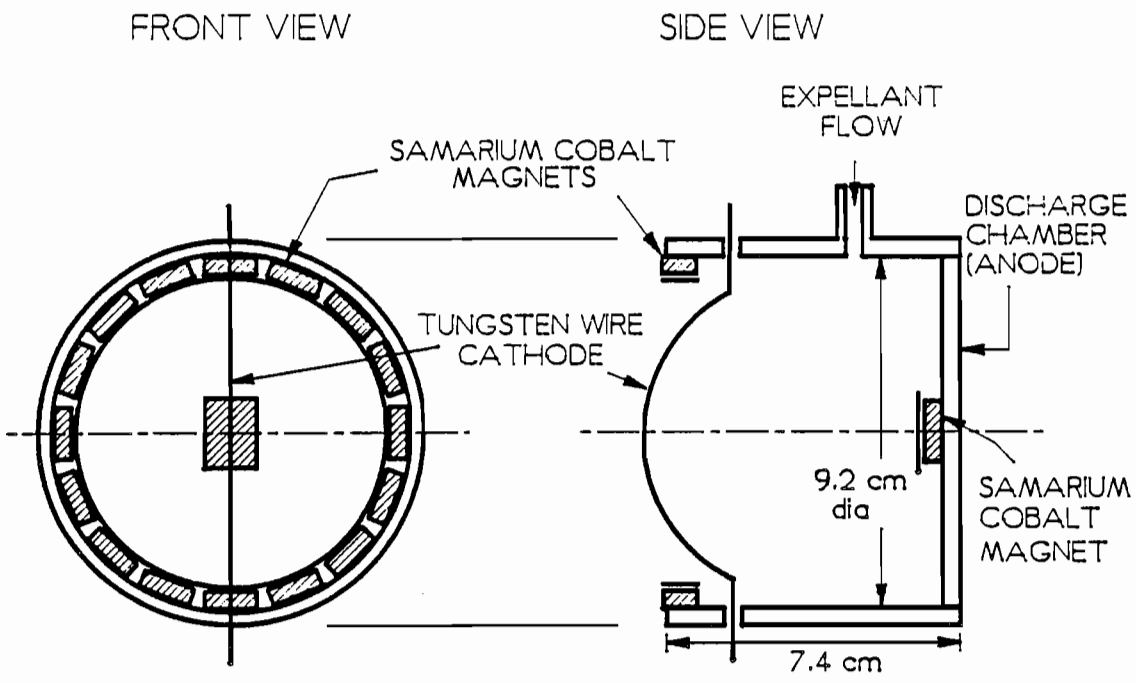

a. Hot Filament Cathode-Based Simulator

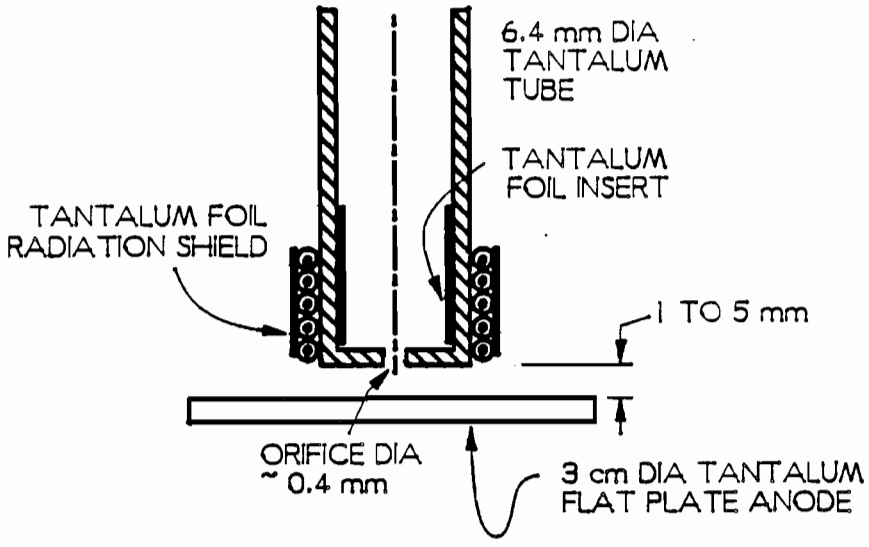

b. Hollow Cathode-Based Simulator

Fig. 2-4 Simplified Schematics of Simulators

device. For most of the experimental results presented in this study, the simulator shown in Fig. 2-4a was operated at a discharge current and voltage of 0.5 A and 40 V, respectively, and a simulator flowrate of 2.7 sccm (Xe). In addition to the hot filament cathode-based simulator, a simple hollow cathode device was also used in some experiments and it is shown in Fig. 2-4b. The hollow cathode tube was 6.4 mm in dia. and it was capped with an orifice plate that contained a $\sim$0.4 mm orifice. The simulator hollow cathode axis was oriented perpendicular to the line joining the contactor and simulator. This simulator utilized a 3 cm dia., flat plate anode that was positioned between 1 and 5 mm downstream of the orifice plate. The simulator discharge current and voltage were typically 0.5 A and 20 V, respectively, and its flowrate was set at 2.7 sccm (Xe).

Typical tests were conducted by starting the simulator and contactor discharges and selecting the desired contactor flowrate and discharge current. Next, the contactor was biased relative to the simulator using the bias power supply; and voltage, current and probing instrument data were collected. The voltages and currents measured during typical tests are designated by the symbols shown within the circles in Fig. 2-3 and defined in the nomenclature list contained in Appendix C. These quantities include the contactor and simulator discharge currents and voltages, the bias voltage between the contactor and simulator, and the contactor and simulator electron emission currents.

The tank bias switch shown in Fig. 2-3 was installed so the vacuum tank could be allowed to float relative to the contactor/simulator system or could be connected to the contactor or simulator. The two additional switches shown directly below the

contactor and simulator were both positioned in the EC location when the contactor was collecting electrons and in the EE location when it was emitting them. The effects of the vacuum tank wall on experimental results were minimized when the vacuum tank was floated. However, its effects were also small when it was connected to the simulator cathode during contactor electron collection experiments, or when it was connected to the contactor cathode during contactor electron emission experiments. In both of these conditions, the vacuum tank walls were at a potential substantially negative (typically 20 to 40 V) of the simulated ionospheric plasma. When the vacuum tank walls were connected in the manner just described, the ammeters (located below the simulator and contactor in Fig. 2-3) labeled J_{SE} and J_{CE} typically agreed within 20%.

The plasma environment produced between the contactor and the simulator was probed using the various instruments shown in Fig. 2-2. They include an emissive probe [14,23], a Langmuir probe [24], and a retarding potential analyzer (RPA) [4,25]. The emissive probe was used to measure plasma potential and the Langmuir probe was used to determine electron temperatures and densities. The RPA consists of a cylindrical Faraday cage with an orifice plate at one end, and it was operated by first sighting its orifice at the plasma contactor and then recording the ion current to the probe collector as the voltage was swept from 10 V below contactor cathode potential to about 100 V above it. This current/voltage data could then be used to determine the energy characteristics and current densities of ions flowing away from the contactor plasma cloud region. The details of RPA current/voltage traces and their analysis and interpretation are discussed in Appendix A, which also contains a

detailed description of emissive and Langmuir probes. In addition, Appendix A contains estimates of measurement errors associated with the use of these plasma diagnostic instruments.

III. THE ELECTRON COLLECTION PROCESS

A. Experimental Observations

The electron collection performance of a hollow cathode plasma contactor tested under typical conditions can be characterized using a plot like the one shown in Fig. 3-1. It shows a 4th quadrant plot of electron emission current versus contactor potential. The contactor was operated at the conditions listed in the legend and the tank switch (shown in Fig. 2-3) was connected to the simulator. The contactor is shown to exhibit poor electron collection performance until a sufficiently high potential is reached--~40 V. At this potential the electron collection current increases quite suddenly. This increase in current is associated with the "transition to the ignited mode," and it is linked to ionization of neutrals in the plasma immediately adjacent to the contactor by electrons streaming toward it from the ambient plasma.

Extensive data have been collected when the contactor is collecting electrons and a typical plasma potential structure that develops in the region surrounding a contactor is shown in Fig. 3-2. A steep and well-defined "double layer" region is shown where a majority of the potential difference between the contactor plasma cloud and ambient plasma developed. In this particular example, the contactor was collecting 750 mA of electrons from the ambient plasma, and the double layer potential drop was about 40 V. The plasma contactor was operating at a relatively low discharge power of 5.4 W and the flowrate of neutral xenon atoms through the

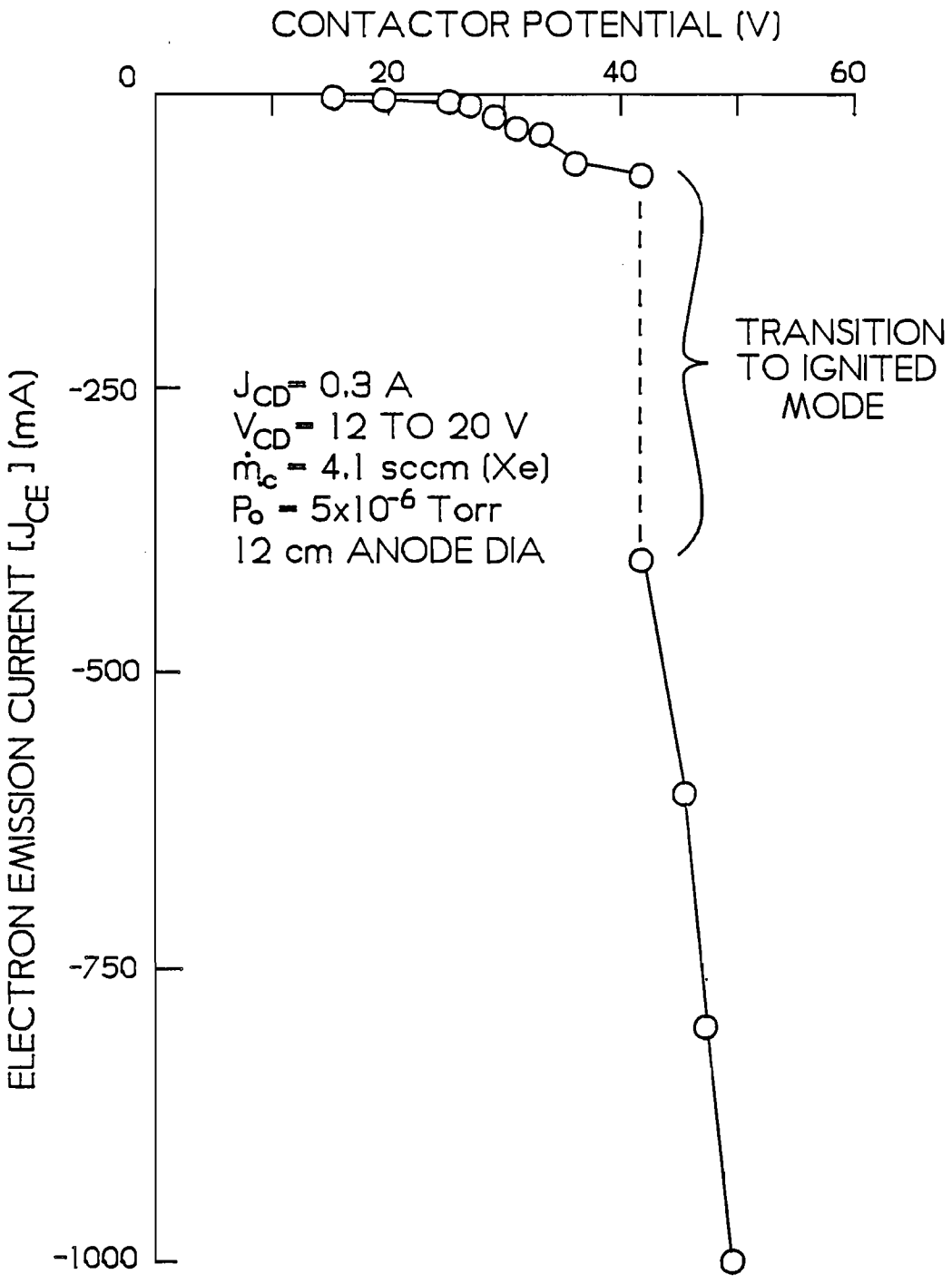

Fig. 3-1 Typical Plasma Contactor Performance Curve

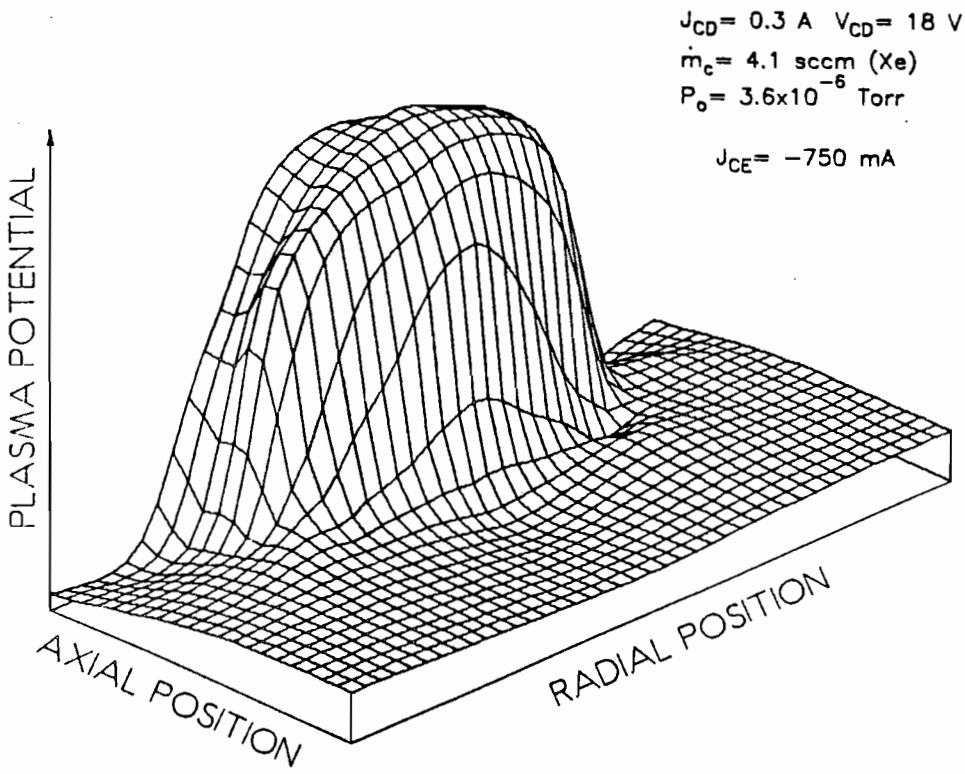

a. Raised Potential Map

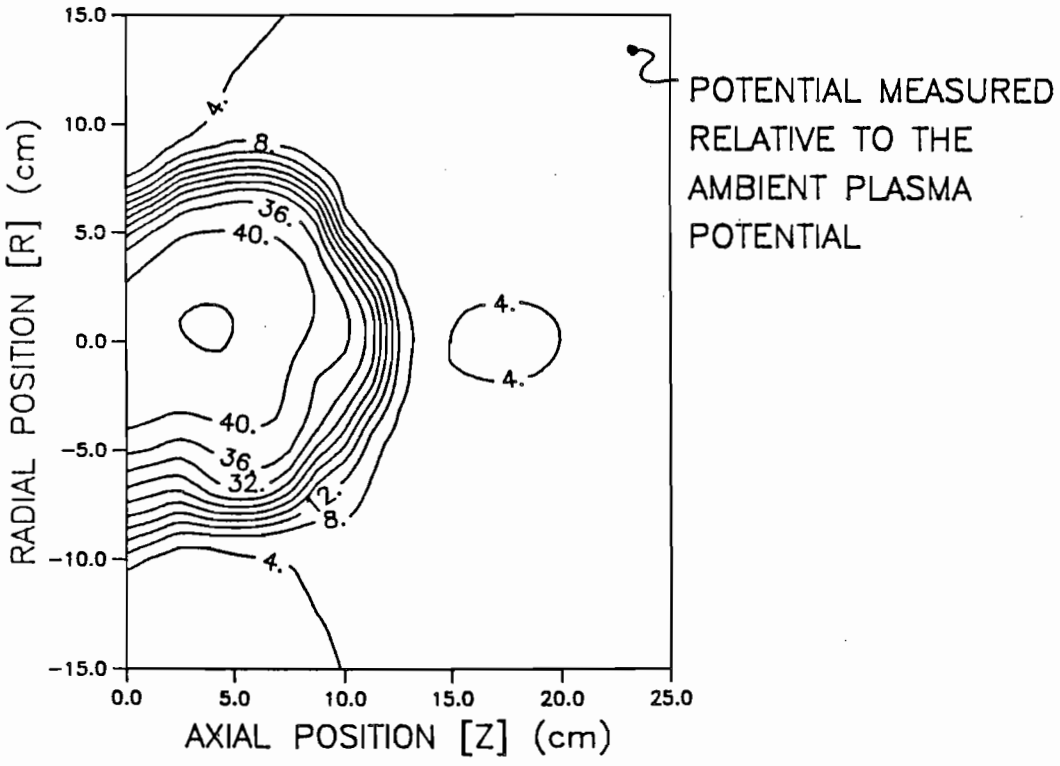

b. Equipotential Contour Map

Fig. 3-2 Typical Plasma Potential Variation near a Contactor Collecting Electrons

contactor hollow cathode was at a typical value of 4.1 sccm (Xe). This flowrate along with the simulator flowrate of 2.7 sccm (Xe) induced a vacuum system background pressure of 3.6×10^{-6} Torr.

On the basis of the typical data of Fig. 3-2, one can propose the phenomenological description of the electron collection process suggested by Fig. 3-3. This figure shows a relatively high density plasma cloud adjacent to the contactor which is separated from a lower density ambient plasma by a double layer. As the centerline plasma potential profile in this figure suggests, electrons and ions counterflow through the double layer. The ion and electron currents that can be drawn through the double layer region are assumed to be limited by the space-charge effects which are suggested by the regions of net accumulations of positive and negative charge shown, respectively, upstream and downstream of the double layer midpoint in the bottom sketch of Fig. 3-3.

When plasma properties are measured along the vacuum tank centerline, data such as those shown in Fig. 3-4 are obtained. These results suggest plasma conditions do vary in a way that is consistent with those displayed in Fig. 3-3. Figure 3-4a displays how plasma potential varies, and a well-defined double layer is shown to be located between 10 and 15 cm. The potential drop across the double layer is about 20 V, and it is noted that the contactor anode was about 10 V positive of the contactor plasma cloud. It is noted that the plasma potential plotted in Fig. 3-4a was measured with respect to the vaccuum tank and simulator cathode. It is noted that the plasma potential plotted in Fig. 3-4a was measured with respect to the vacuum tank wall. The inner (r_i) and outer (r_o) locations of the double layer

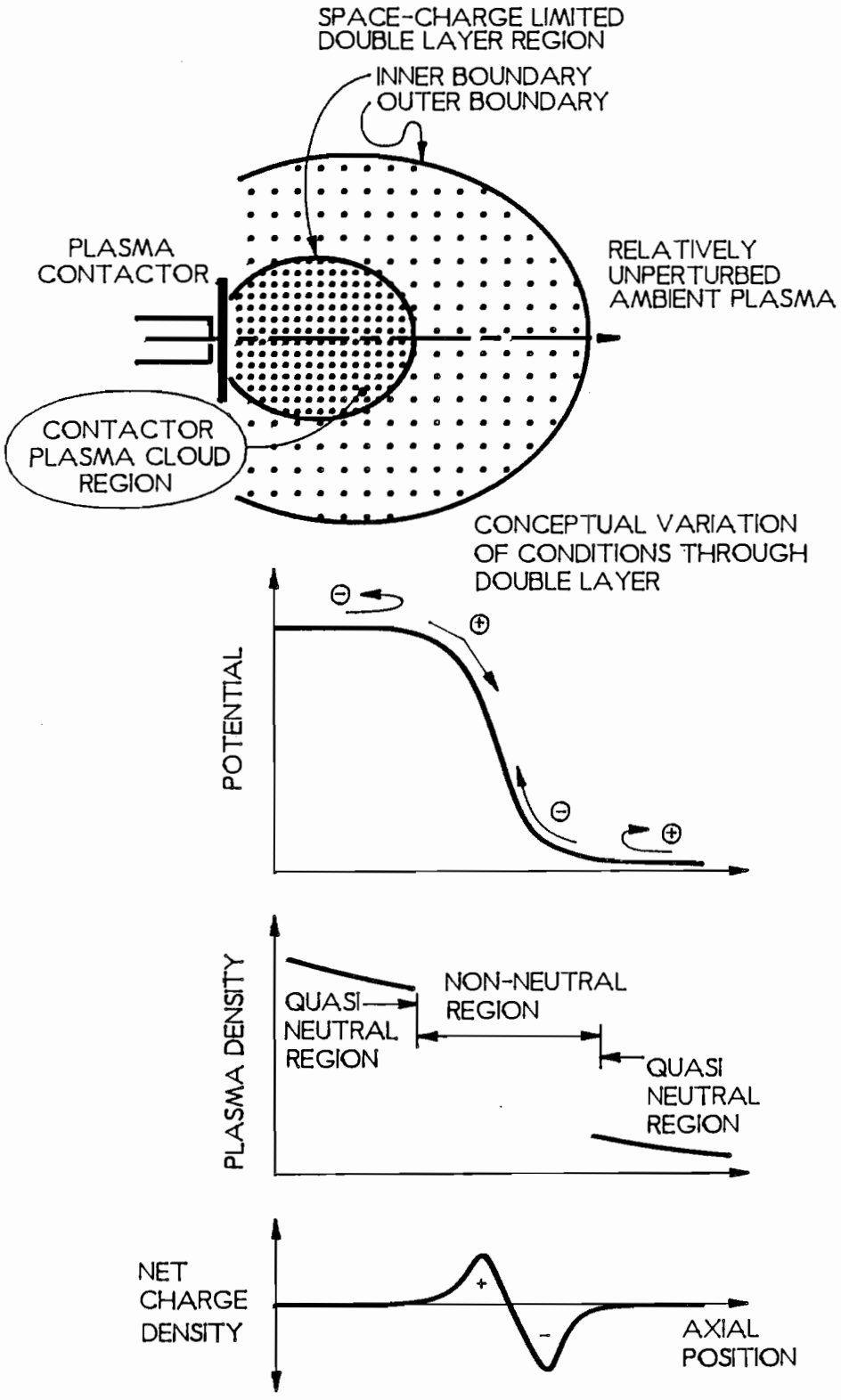

Fig. 3-3 Conceptual Description of the Electron Collection Process

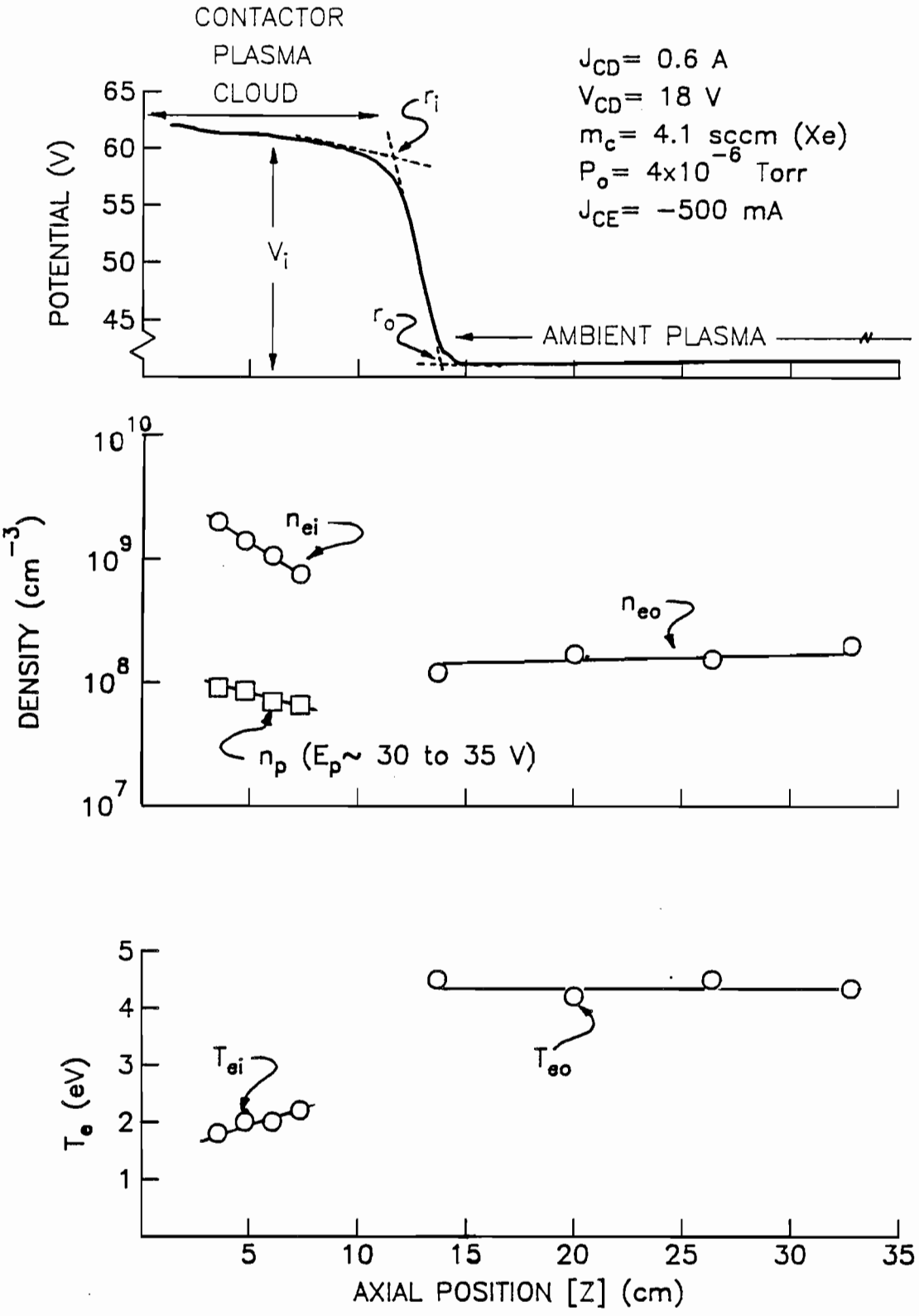

Fig. 3-4 Typical Plasma Properties Measured along the Centerline

boundary were found by drawing lines through the double layer, contactor plasma cloud and ambient plasma regions and finding the intersection points as shown on Fig. 3-4a.

Figure 3-4b displays axial profiles of electron densities in the contactor plasma cloud and ambient plasmas. The electron densities were calculated from Langmuir probe traces using a two-electron group analysis procedure [24,26] which is explained in more detail in Appendix A; i.e. electrons in the plasmas were assumed to have a Maxwellian plus primary (mono-energetic) energy distribution. The data labeled n_{ei} and n_{eo} in Fig. 3-4b correspond to Maxwellian electron group densities in the contactor plasma cloud and ambient plasmas, respectively. The data labeled n_p, on the other hand, correspond to primary electron group densities in the contactor plasma cloud. This high energy group of electrons ($E_p \sim 30$ eV) is believed to be composed of ambient electrons that have been accelerated from the ambient plasma through the double layer and into the contactor plasma cloud region. It is noted that the primary electron energy is of order T_{eo} plus the $\sim$20 eV energy that ambient plasma electrons would acquire after being accelerated across the double layer. Some primary electrons were also detected in the ambient plasma, but their properties were difficult to determine because of their low densities ($<$ 5 to 10 % of n_{eo}) and their relatively low energies ($E_p \sim$ 10 to 20 eV). The higher plasma densities in the contactor plasma cloud compared to the ambient plasma is consistent with other experimental results obtained in basic double layer experiments [8,9,10,12].

Finally, Fig. 3-4c displays the axial variation of Maxwellian electron temperature in the contactor plasma cloud and ambient plasma regions. The electron

temperature is shown to be about 2 eV in the contactor plasma cloud and 4.5 eV in the ambient plasma. In this case the temperature of the electrons in the higher potential plasma (the contactor plasma cloud) is less than that in the lower potential one (the ambient plasma). This result has also been observed by Guyot and Hollenstein [9]. However, a higher electron temperature in the high potential plasma than in the low potential plasma is typically observed in a majority of basic double layer experiments conducted in triple plasma-based systems [8]. Chan, et.al. [27] discuss this apparent inconsistency in more detail, and suggest through energy balance, geometry and anomalous collision arguments that some types of double layers might shield two plasmas thermally, while other plasma conditions might enhance thermal conduction across them.

In addition to the data shown in Fig. 3-4, the relative noise level in the ambient plasma was also measured and found to be about 0.2 to 0.3 which can cause errors in Langmuir probe data interpretation. Noise measurements and their affect on Langmuir probe data are discussed in more detail in Appendix A along with other details concerning the plasma diagnostic apparatus and procedures. Additional information about the ambient plasma conditions is summarized and compared to the plasma conditions in low Earth orbit in Appendix B.

B. Phenomenological Model of the Electron Collection Process

A model, which describes electron collection from an ambient neutral plasma, was developed by assuming that the current being drawn through the circuit is conducted almost entirely by electrons and that the current flows through each region via a spherical segment of solid angle ($0 < \psi < 4\pi$) in the manner suggested in

Fig. 3-5. The ambient plasma region in Fig. 3-5 is characterized by an electron (and ion) density n_{eo} and an electron temperature T_{eo}. The neutral atom pressure and temperature reach ambient values P_o and T_o far from the contactor in the ambient plasma region. The neutral atom density n varies from a minimum, corresponding to the ambient pressure and temperature, to a maximum at the contactor where neutral atoms at temperature T_c are being supplied from a point source at a rate of $\dot{n}$.

The electron current flowing from the ambient plasma into the contactor plasma cloud is assumed to be equal to the random ambient electron current incident on the outer boundary of the double layer region located at r_o and is given by

$$|J_{CE}| = \frac{1}{4} e n_e \psi r_o^2 \sqrt{\frac{8kT_{eo}}{\pi m_+}} \quad . \quad (3\text{-}1)$$

Both the ion and electron currents shown counter flowing through the double layer region in Fig. 3-5 are assumed to be space-charge limited. The assumptions made to obtain the solution of the spherical double-layer problem together with the pertinent equations and figures are summarized from Ref. [28] for completeness. The basis of the development is that an inner spherical surface of radius r_i and potential V_i is supplying an ion current from an infinite supply of zero velocity ions at the inner surface (the contactor plasma cloud boundary). Simultaneously, electrons of negligible velocity are drawn from the outer spherical surface of radius r_o (the ambient plasma region boundary). In order to simplify the analysis, it is assumed that no collisions (elastic or inelastic) occur within the double layer region. When equations describing conservation of energy and conservation of charge are used in conjunction with Maxwell's formulation of Gauss' Law, equations describing the

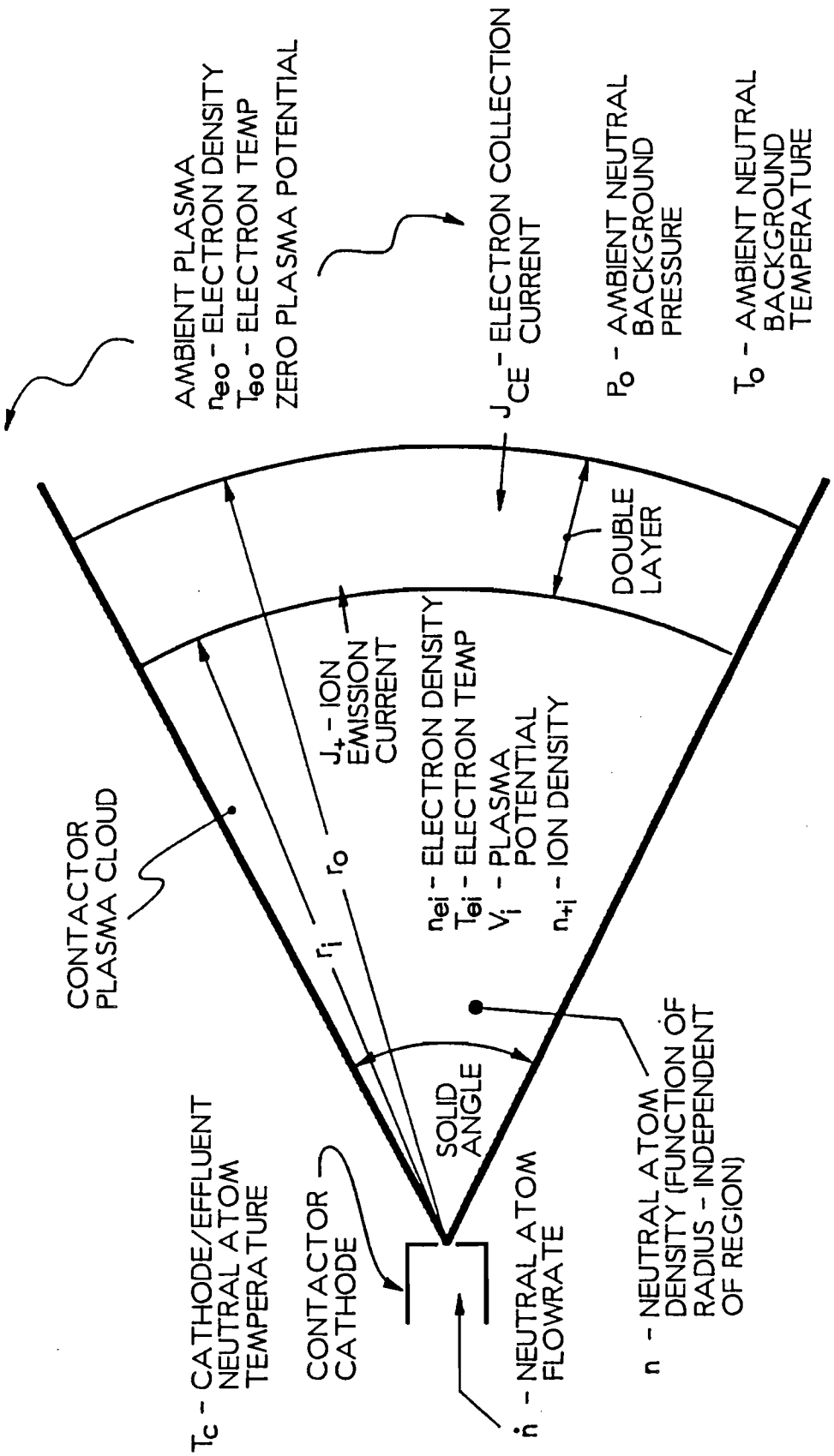

Fig. 3-5 Physical Model of Electron Collection

maximum flow of ions from the inner sphere (J_+) and electrons from the outer sphere (J_{CE}) can be expressed in terms of the applied potential difference and the radius ratio of the two spherical segment surfaces. These limiting maximum currents, which are achieved when the potential gradients at the edges of both spherical surfaces are zero, are given in Ref. [28] as

$$|J_{CE}| = \psi\, \varepsilon_o \sqrt{\frac{2e}{m_e}}\; V_i^{3/2}\, j_o \tag{3-2}$$

$$J_+ = \frac{|J_{CE}|}{\alpha} \sqrt{\frac{m_e}{m_+}} \tag{3-3}$$

The quantities j_0 in Eq. 3-2 and α in Eq. 3-3 are parameters that depend only on the double layer radius ratio r_i/r_0. The variation of the parameters α and j_0 with radius ratio have been determined numerically [28] and these relationships are shown in Figs. 3-6 and 3-7. Typically, radius ratios close to 1 are desired because this implies large j_0, and, at a given electron collection current, low double layer potential drops. It is also noted that Fig. 3-7 shows α to be nearly 1 at radius ratios close to 1, and that α is not a strong function of radius ratio. This suggests (through Eq. 3-3) that the ion emission current should be nearly proportional to the electron collection current.

The model further presumes the double layer develops between the radii r_i and r_0 and the ion current that flows through the double layer (given in Eq. 3-3) must be supplied from the contactor plasma cloud. The plasma properties of this region are listed in Fig. 3-5 as an electron density and temperature of n_{ei} and T_{ei} and a plasma potential V_i (measured relative to the ambient plasma potential). The ion density n_{+i},

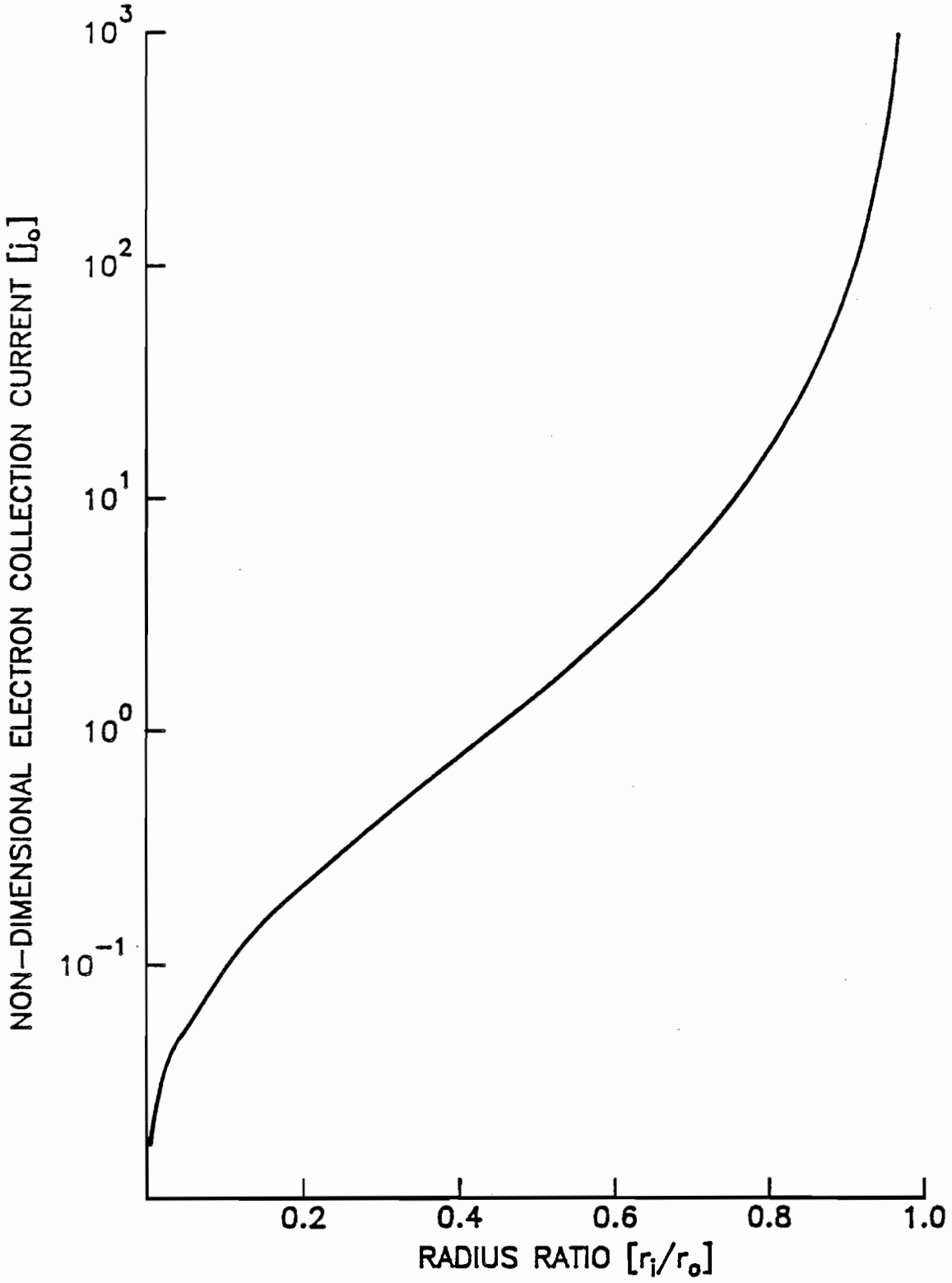

Fig. 3-6 Non-Dimensional Electron Collection Current Versus Double Layer Radius Ratio (from Wei and Wilbur, 1986)

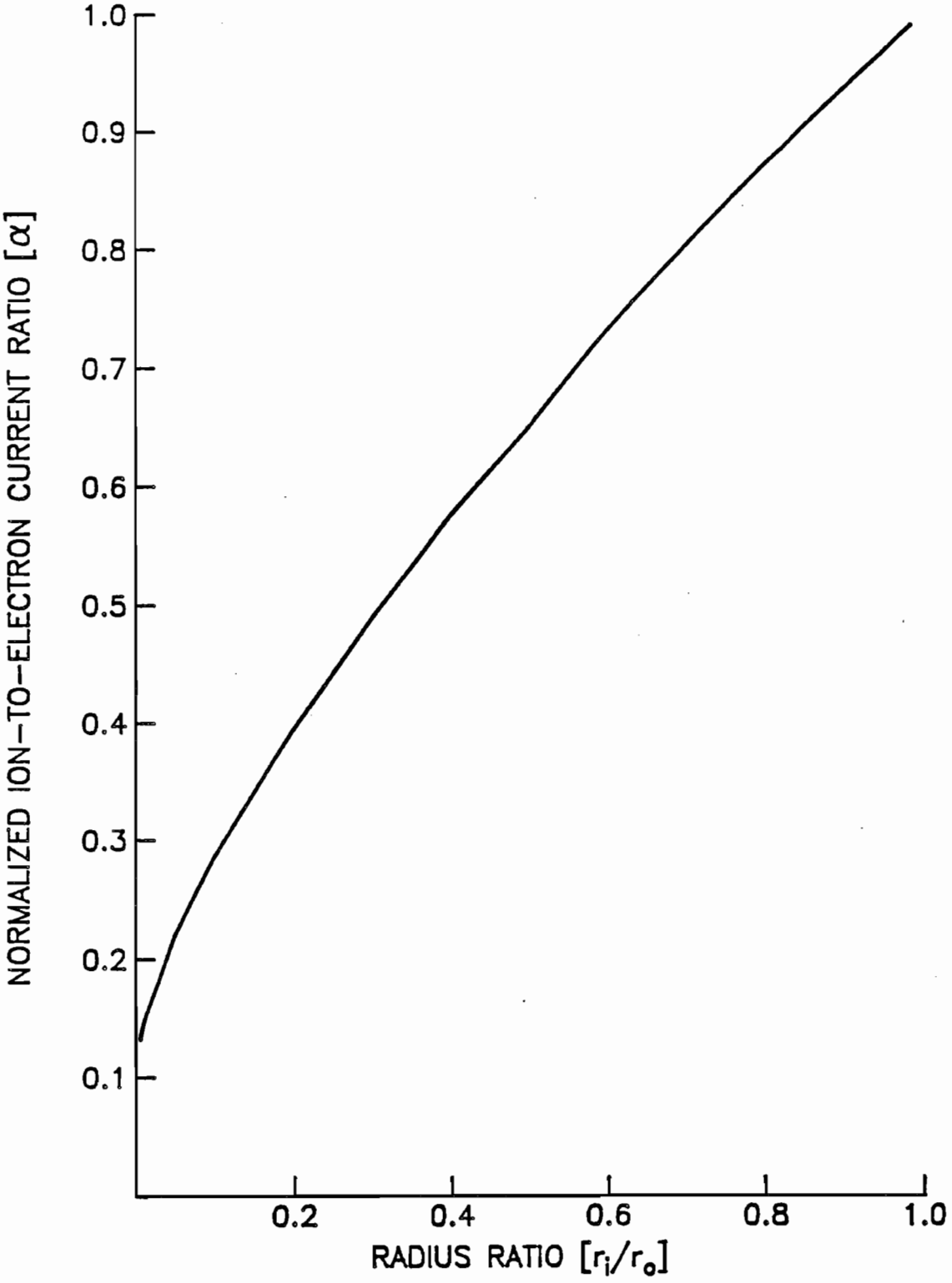

Fig. 3-7 Normalized Ion-to-Electron Current Ratio Versus Double Layer Radius Ratio (from Wei and Wilbur, 1986)

which is equal to the electron density in this region, is sufficiently high so ions can be extracted through the double layer at the current J_+. This ion current can be written in terms of the plasma density in the contactor plasma cloud if it is recognized that the ion loss rate to the double layer is controlled by the Bohm criterion [29] for a stable sheath defined by the equation

$$J_+ = e\, n_{+i}\, \psi\, r_i^2 \sqrt{\frac{k T_e}{m_+}}\, \gamma \qquad (3\text{-}4)$$

In Eq. 3-4, γ is a correction factor that accounts for the effects of pre-sheath acceleration of ions from the contactor plasma cloud toward the double layer, and it will be set equal to 0.3. Bohm suggests a value of ~ 0.6 for this factor [29], however, other work has suggested that its value can vary from 0.1 to 1 [19].

Ion production will occur within the contactor plasma cloud when contactor discharge electrons experience ionization collisions with neutral atoms near the orifice of the hollow cathode. Because these ions are formed near the cathode and anode of the contactor, many can recombine on these surfaces and do not escape through the double layer. Ions can also be produced in the contactor plasma cloud by electrons streaming from the ambient plasma which experience ionization collisions with neutral atoms before they are collected at the contactor anode. It is believed that the streaming electrons produce ions closer to the inner boundary of the double layer than do the discharge electrons and it is suggested therefore that ions produced by streaming electrons are more likely to escape from the high density plume region through the double layer. It is noted that the production of ions at a significant rate by the streaming electrons is accompanied by the development of luminosity within

the contactor cloud and as a result operation in this condition has been termed the "ignited mode" (shown in Fig. 3-1).

Substantial ion production induced by the streaming electrons occurs when 1) streaming electrons acquire sufficient energy as they pass through the double layer to induce ionization and excitation of neutrals and 2) the density of expellant atoms in the contactor cloud is relatively high so the probability that these collisions will occur is significant. An expression that gives the ion production rate due to streaming electrons is

$$J_{+p} = |J_{CE}| \frac{\sigma_+}{\sigma_{in}} \left[1 - \exp\left[-\sigma_{in} \left\{ \frac{\dot{n}}{\psi_o \nu_n} \left(\frac{1}{\delta} - \frac{1}{r_1} \right) + \frac{P_o}{k T_o} (r_i - \delta) \right\} \right] \right] \quad .(3\text{-}5)$$

Equation 3-5 was originally derived in Ref. [30] by assuming that the streaming electrons converge upon a region near the contactor cathode orifice in a spherically symmetric manner. Streaming electrons which experience an inelastic collision are assumed to be thermalized into the contactor cloud plasma, and the ratio of ionization-to-total inelastic collision cross-sections at the energy of the streaming electrons is assumed to represent the ratio of ion production-to-total inelastic collision rate. In Eq. 3-5, δ represents a small distance downstream of the contactor within which ions that are produced fall toward and recombine on the contactor rather than being drawn toward the double layer. At sufficiently high neutral flowrate and streaming electron current and energy conditions, the contactor cloud region can exhibit a large ion production rate. Operation at this "ignited mode" condition induces a large increase in electron collection current corresponding to the increased ion emission current.

This mode of operation is accompanied by luminosity of the contactor cloud region due to neutral atom excitation/de-excitation reactions which occur along with the ionization reactions.

C. Comparison Between Theory and Experiment

There are some aspects of the simple model, presented in the preceding section, that can be compared to experimentally measured quantities. They include model elements associated with 1) electron current collection at the outer double layer boundary, 2) space-charge limited ion and electron current flow through the double layer itself and 3) ion current emission across the inner double layer boundary. While the model has been couched in terms of a variable solid angle ψ, the value of this angle will be assumed to be 4π in all of the comparisons that follow (i.e. the processes will be assumed to be occurring within a full spherical segment).

Equation 3-1 can be rearranged to give the radius of the outer double layer boundary

$$r_o = \left[\frac{4\ |J_{CE}|}{e\ n_{eo}\ \psi} \sqrt{\frac{\pi m_e}{8 k T_{eo}}} \right]^{1/2} \quad . \quad (3\text{-}6)$$

Measurements of electron collection current, ambient plasma density n_{eo} and electron temperature T_{eo} were made under various operating conditions. The plasma property measurements taken at most electron collection current conditions showed that the density and temperature were quite uniform throughout the ambient plasma region so unambiguous values of the current and the ambient plasma properties could be put into Eq. 3-6 and an outer double layer radius based on this aspect of the theoretical

model could be determined. At each operating condition the outer double layer radius could also be measured directly from a corresponding potential profile like the example shown in Fig. 3-4. Figure 3-8 presents a comparison of directly measured experimental and theoretical outer double layer radii over the range of conditions listed in the legend. The straight line drawn on the figure shows where the data would fall if the experiment agreed perfectly with the model. Although the data show considerable scatter about this line, presumably because of errors associated with plasma property measurements and/or a non-spherical double layer boundary, the data suggest the model generally yields values of the outer radius to within about 25%.

The validity of the assumption that the double layer is space-charge limited can be checked by comparing measured radius ratios (i.e. inner radius-to-outer radius ratio for the double layer) with those the model predicts should exist at corresponding electron collection current and double layer potential drop conditions. The radius ratio can be expressed in terms of the normalized current parameter j_o in Fig 3-6. This parameter is in turn related to the electron collection current $|J_{CE}|$ and the double layer potential drop V_i by the following rearranged form of Eq. (3-2)

$$j_o = \frac{|J_{CE}|}{\psi \varepsilon_o V_i^{3/2}} \sqrt{\frac{m_e}{2e}} \quad . \quad (3\text{-}7)$$

Using Eq. 3-7 together with the data of Fig. 3-6, measured electron collection currents and double layer voltage drops, radius ratios associated with a particular operating condition can be computed and compared to experimentally measured ratios determined from corresponding emissive probe plasma potential profiles (i.e. see

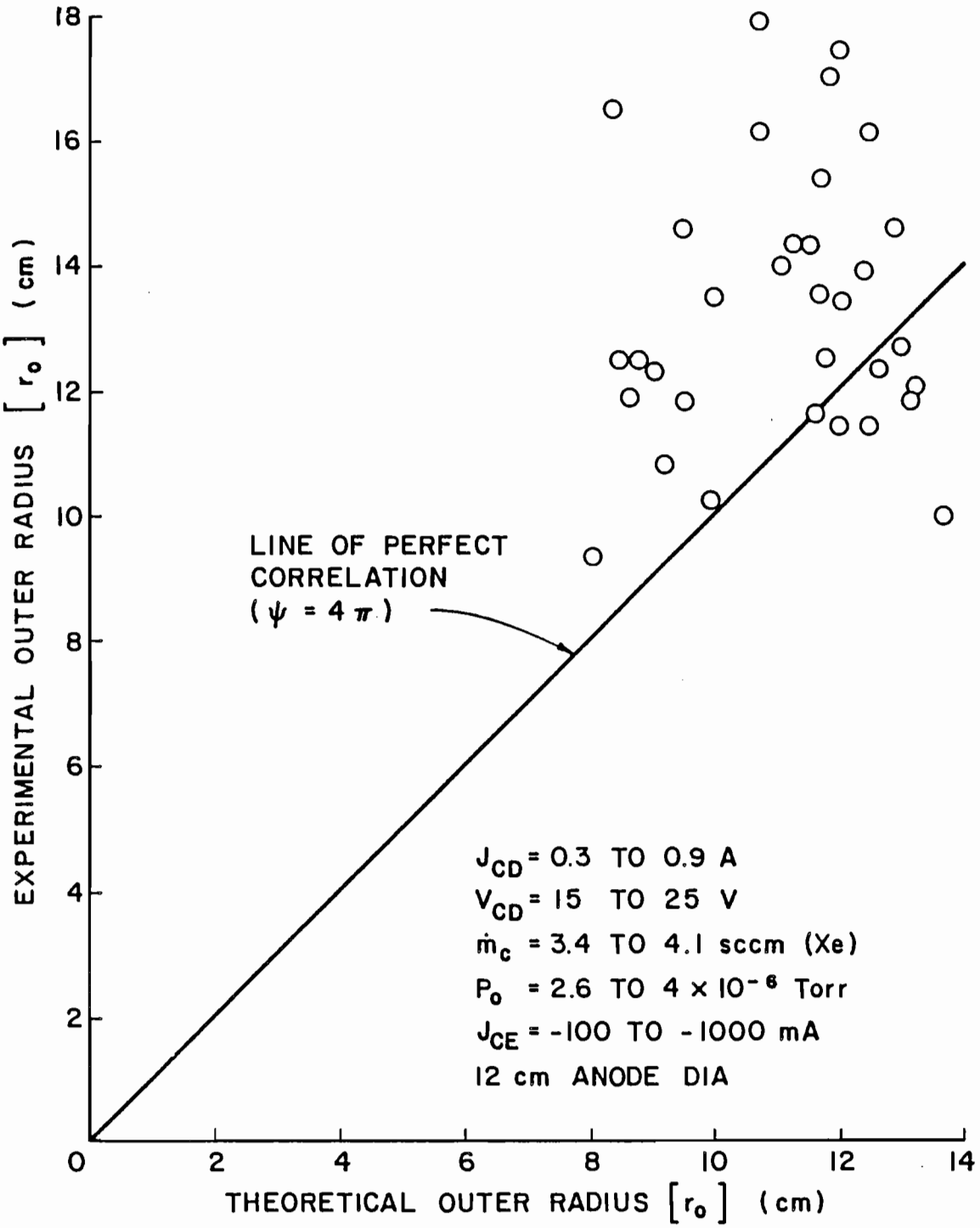

Fig. 3-8 Correlation of Measured and Computed Outer Double Layer Radii

Fig. 3-4a). Figure 3-9 shows this comparison for data obtained over a wide range of test conditions. The circular data points correspond to a contactor anode diameter of 12 cm and to the data and operating condition ranges listed in Fig. 3-9. In addition, other data points are shown on the figure which correspond to smaller anode diameters. As indicated by the perfect fit and 25% error boundary lines, the model predicts radius ratios with reasonable accuracy over a rather large range of operating conditions. It is interesting to note that the 12 cm anode dia data typically fall above a 0.75 radius ratio value while the smaller diameter anode data extend over greater ranges in the region below 0.8 with the 1 cm anode dia covering the largest radius ratio range. It is also noted that all of the circular data points were obtained when the contactor was operating in the ignited electron collection mode. In this mode large electron collection currents are observed and, for typical double layer voltage drops, this implies the radius ratios approaching unity that are observed on the figure.

Equation 3-4, which expresses the constraint on the ion current condition that must be satisfied in order to assure a stable inner sheath (i.e. the Bohm criterion), can be combined with Eq. 3-3 to obtain

$$r_i = \left[\frac{|J_{CE}|}{e\, n_{ei}\, \psi\, \alpha\, \gamma} \sqrt{\frac{m_e}{k\, T_{ei}}} \right]^{1/2} \quad . \quad (3\text{-}8)$$

At a particular operating condition where the electron collection current and the double layer voltage drop are known, the radius ratio associated with that operating condition can be determined from Eq. 3-2 and Fig. 3-6 using the procedure described above. This radius ratio can be used to enter Fig. 3-7 to determine the value of the

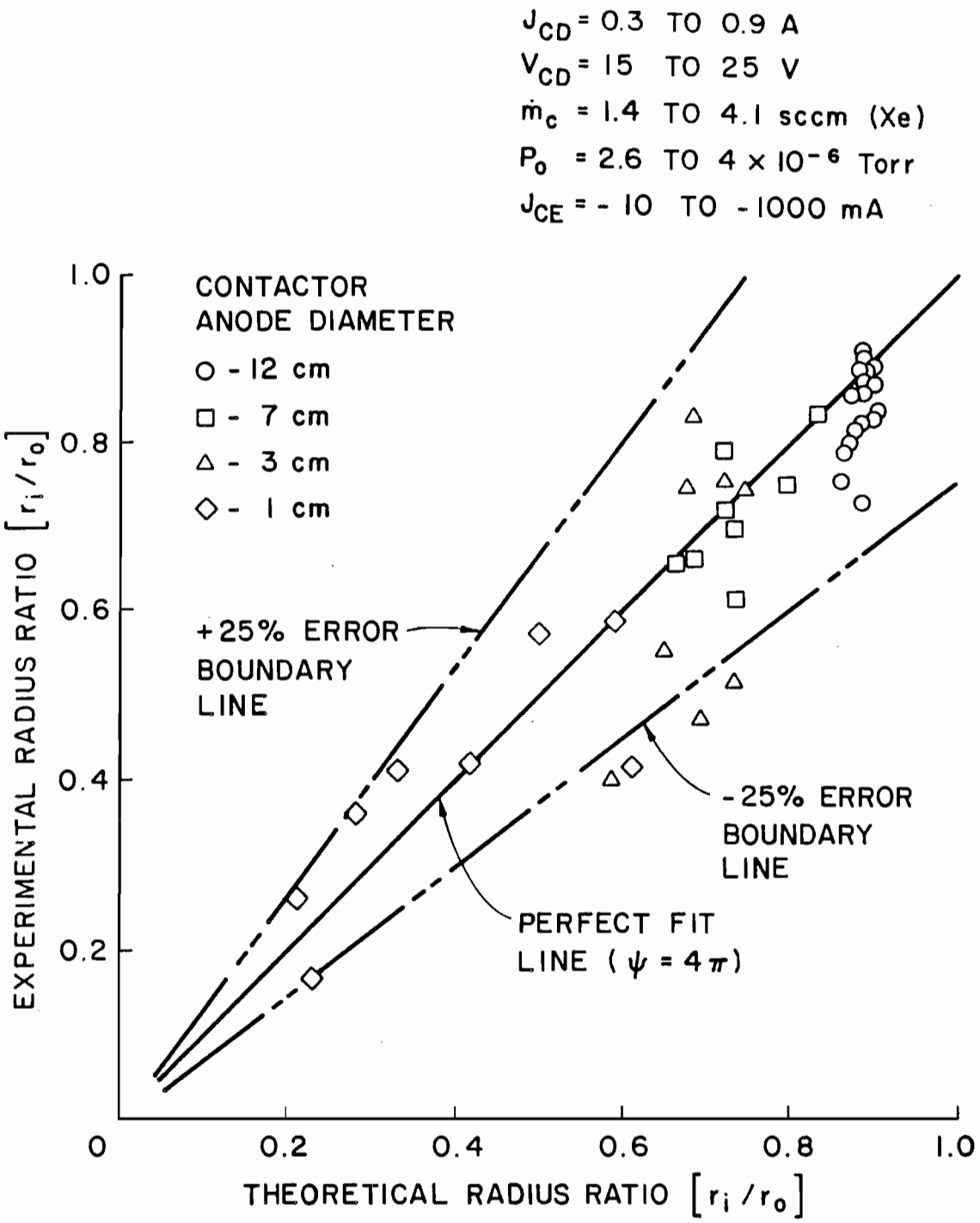

Fig. 3-9 Correlation of Measured and Computed Radius Ratios Based on Space-Charge Limited Double Layer Criteria

parameter α--required in Eq. 3-8. The plasma density n_{ei} and electron temperature T_{ei} in the contactor plasma cloud were also measured just upstream of the double layer boundary, and these data were used in Eq. 3-8 to compute a theoretical inner double layer radius. The value of the pre-sheath correction factor γ which is also required in Eq. 3-8 was assumed to be 0.3. Figure 3-10 presents a comparison of the double layer inner radius computed from Eq. 3-8 and that measured directly from typical data like those shown in Fig. 3-4a. The proximity of the data points to the perfect fit line suggests that the model describes the experimental results to within 25%. It is concluded from these results, therefore, that the Bohm criterion can be applied to determine the radius of the inner boundary of a double layer.

The RPA could be used to measure the ion emission current density as a function of the electron collection current by holding the collector of the RPA slightly positive of the ambient plasma potential. When this was done, the azimuthal variation of the ion emission current density (ions directed away from the contactor plasma cloud) could be measured, and a typical data set is shown in Fig. 3-11. Note that the ion emission current density is a maximum on the centerline and that it drops to lower values on either side of the centerline. One can integrate the ion emission current density data contained in Fig. 3-11 over a hemispherical surface with the radius of the RPA sweep arc (18 cm) to determine the overall ion emission current flowing from the contactor to the ambient plasma. The result is 4.2 mA for this case which is about 3 times more than Eq. 3-3 would predict. Although this error seems large it is probably within the experimental error of the RPA. The RPA could also be used to measure the ion emission current density as a function of the electron collection

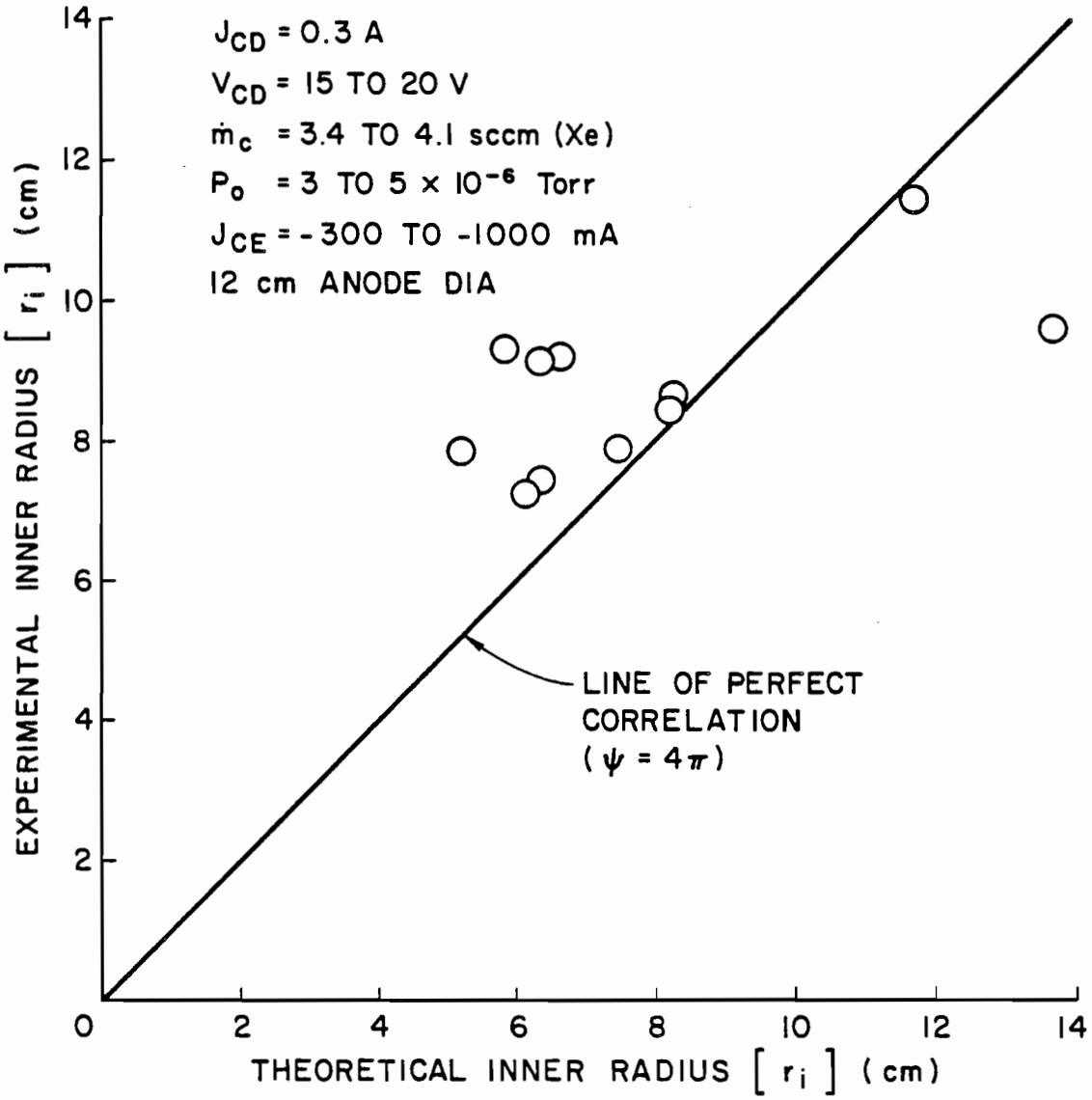

Fig. 3-10 Correlation of Measured and Computed Inner Double Layer Radii

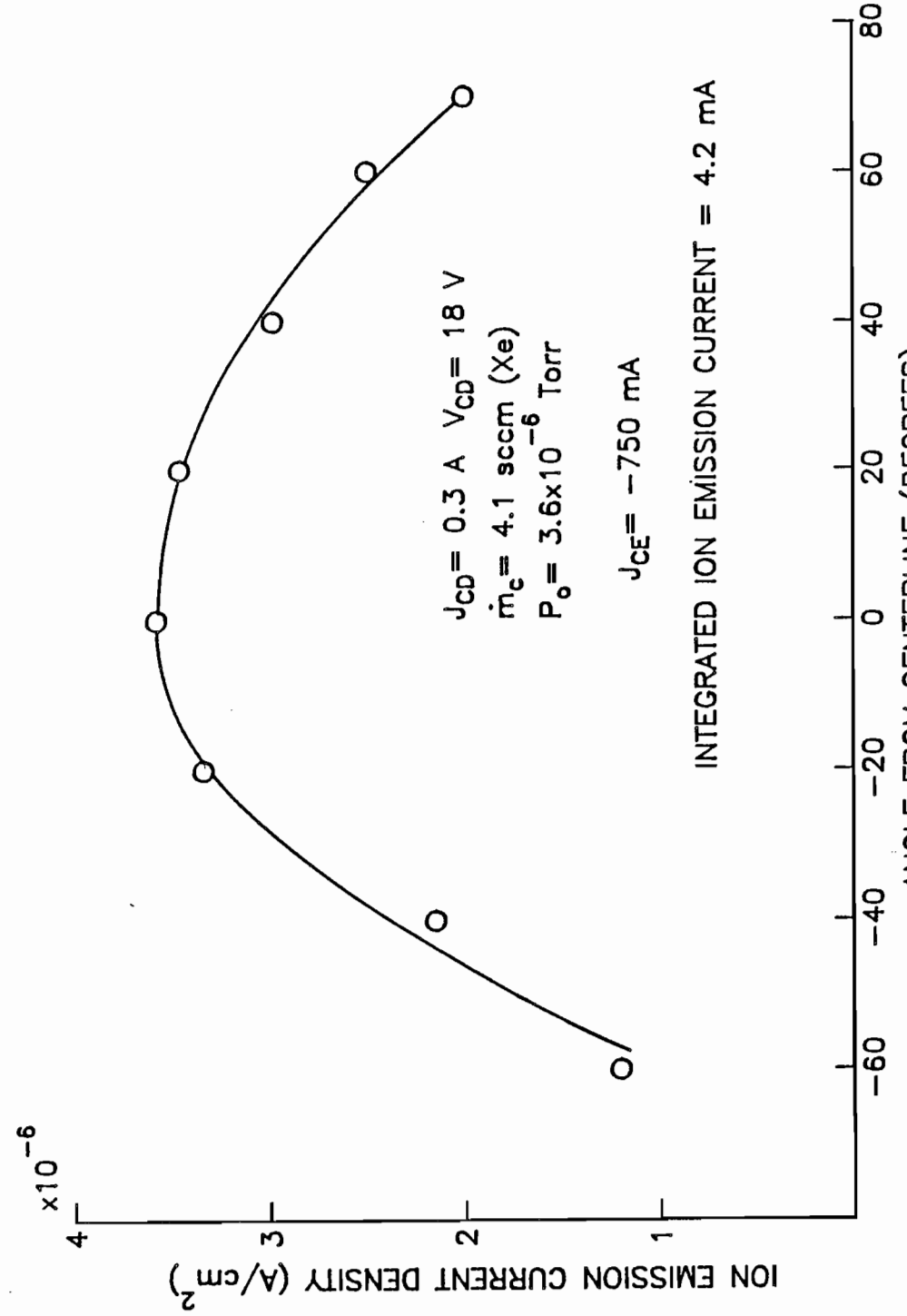

Fig. 3-11 Azimuthal Variation of Ion Emission Current Density

current. When this was done and the RPA was positioned on the centerline at ~18 cm downstream of the contactor, the data shown in Fig. 3-12 were obtained, and they display a linear dependance. On the basis of data like those shown in Fig. 3-11, one can assume that the centerline ion emission current density is proportional to the total ion emission current. If this assumption is true, then Fig. 3-12 implies that the ion emission current varies linearly with electron collection current. This is in agreement with Eq. 3-3.

One can change the size and geometrical conditions of the double layer by changing the flowrate to the contactor [26]. Figure 3-13a shows that an increase in flowrate induces improved contactor performance at a 750 mA emission current by reducing the double layer potential drop. Figure 3-13b indicates, however, that the ion emission current density remains relatively constant over the range of flowrates investigated. These data suggest that ion emission current density is relatively insensitive to flowrate, and this observation is in agreement with Eq. 3-3 which suggests that the ion emission current should depend mostly on the electron collection current. However, the potential difference across the double layer does vary with flowrate and Fig. 3-13 shows that it drops from 66 V at a flowrate of 2.9 sccm (Xe) to 24 V at 6.3 sccm (Xe). This trend is supported by Eq. 3-5 which suggests that higher ionization and total inelastic cross sections are necessary at lower expellant flowrates and background neutral pressures in order to supply the necessary ion emission current. This in turn means that the double layer potential drop must increase at lower flowrates since this potential drop determines the energy of the streaming electrons and, consequently, the cross section magnitudes.

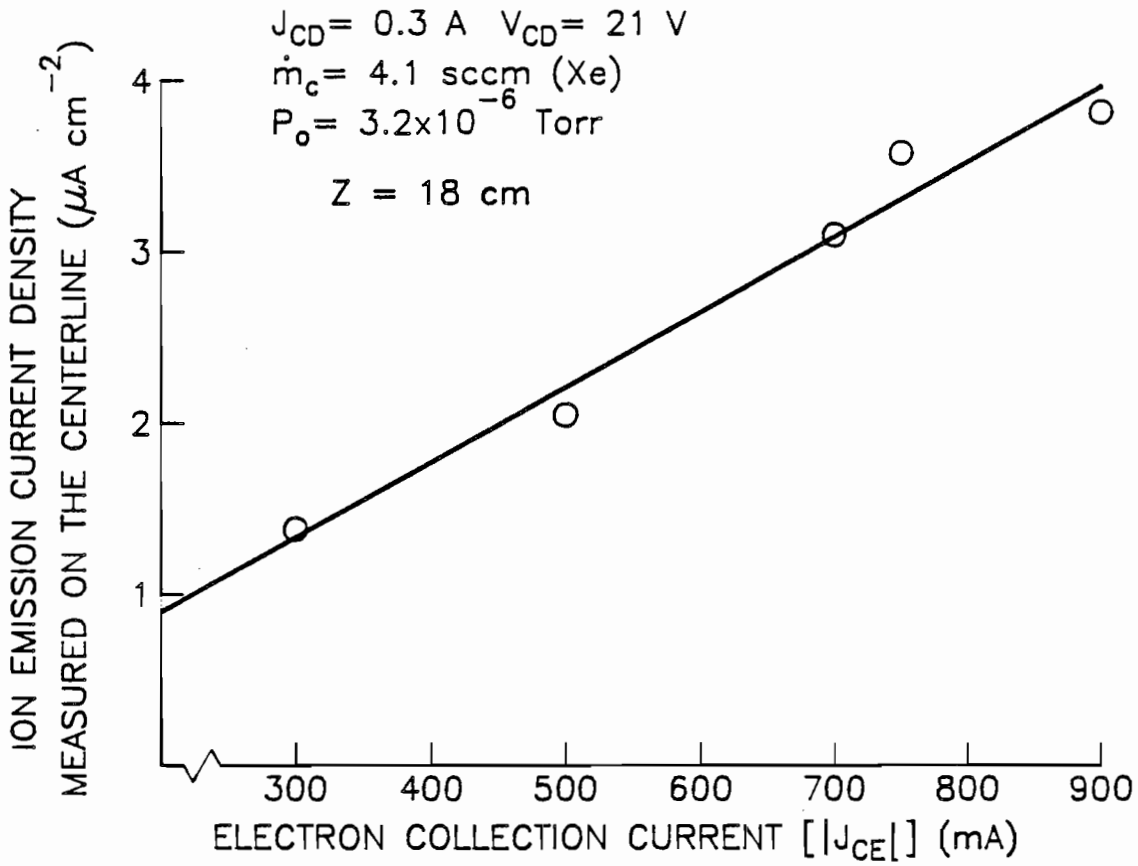

Fig. 3-12 Effect of Electron Collection Current on Centerline Ion Emission Current Density

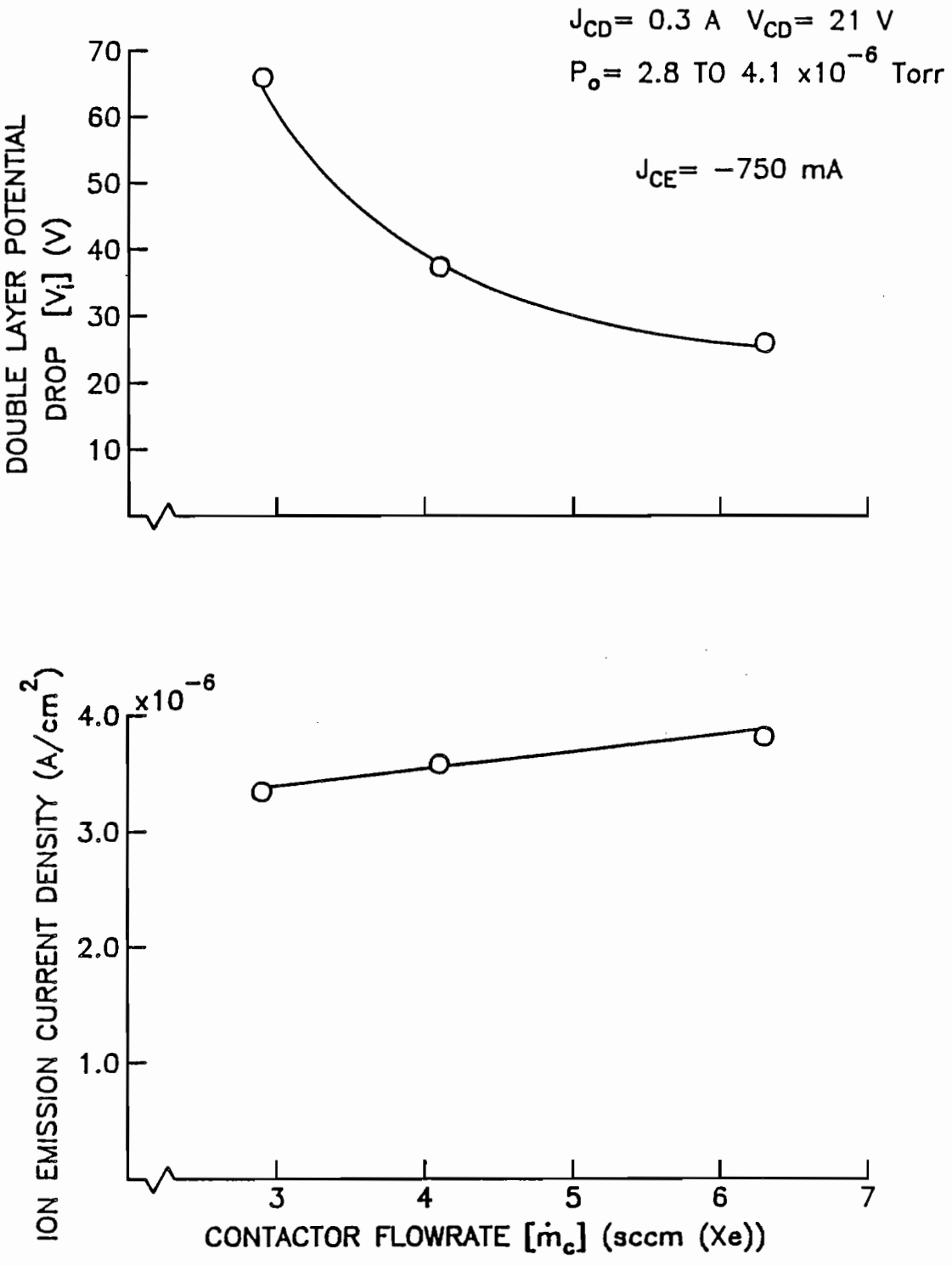

Fig. 3-13 Effect of Contactor Flowrate on Double Layer Potential Drop and Centerline Ion Emission Current Density

The effect of flowrate on the contactor performance is shown in Fig. 3-14. The circular data points correspond to the lowest flowrate of 4.1 sccm, and this curve transitions into the ignited mode at contactor potential of about 30 V. The ignited mode transition is shown to move to lower contactor potentials as the flowrate is increased. Note that the ambient neutral density in the vacuum chamber increased with flowrate, and could have affected the ignited mode transition potential. Separate experiments that were performed at NASA Lewis using a 12 cm anode, hollow cathode-based contactor under lower neutral pressures conditions suggested that lower pressures increase the ignited mode transition potential [15]. However, the same trend of improving performance with increasing flowrate was observed.

In addition to flowrate, the anode diameter was observed to affect the contactor performance. Results of an experiment conducted to demonstrate this are presented in Fig. 3-15. The data in this figure show that small anode diameters require much larger contactor potentials than large anode diameters at similar collection current levels. (It is noted that the 1 and 3 cm dia. data sets do not extend past 250 and 550 mA of electron collection because of bias power supply limitations.) It is possible that this trend is caused by the fact that electron focusing to smaller anodes may begin to be limited by angular momentum considerations as suggested by Davis and Katz [18]. In addition, smaller anode diameters have been observed to cause the contactor plasma cloud and double layer boundaries to be non-spherical (i.e. two- or three-dimensional) [33]. These observations imply that the simple, one-dimensional, spherical model presented earlier does not reflect the effects of changes in anode diameter properly.

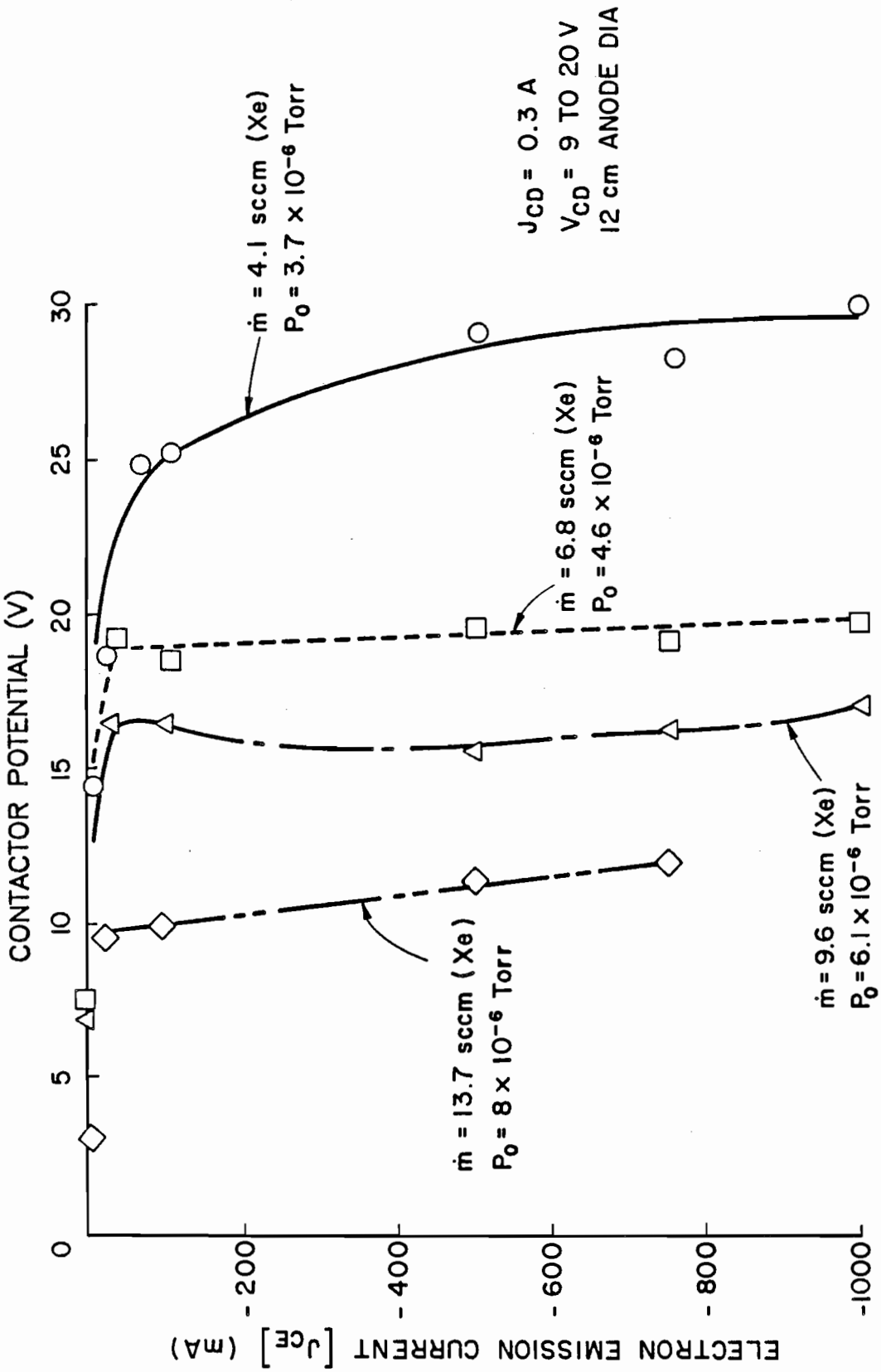

Fig. 3-14 Effect of Contactor Flowrate on Contactor Performance Curves

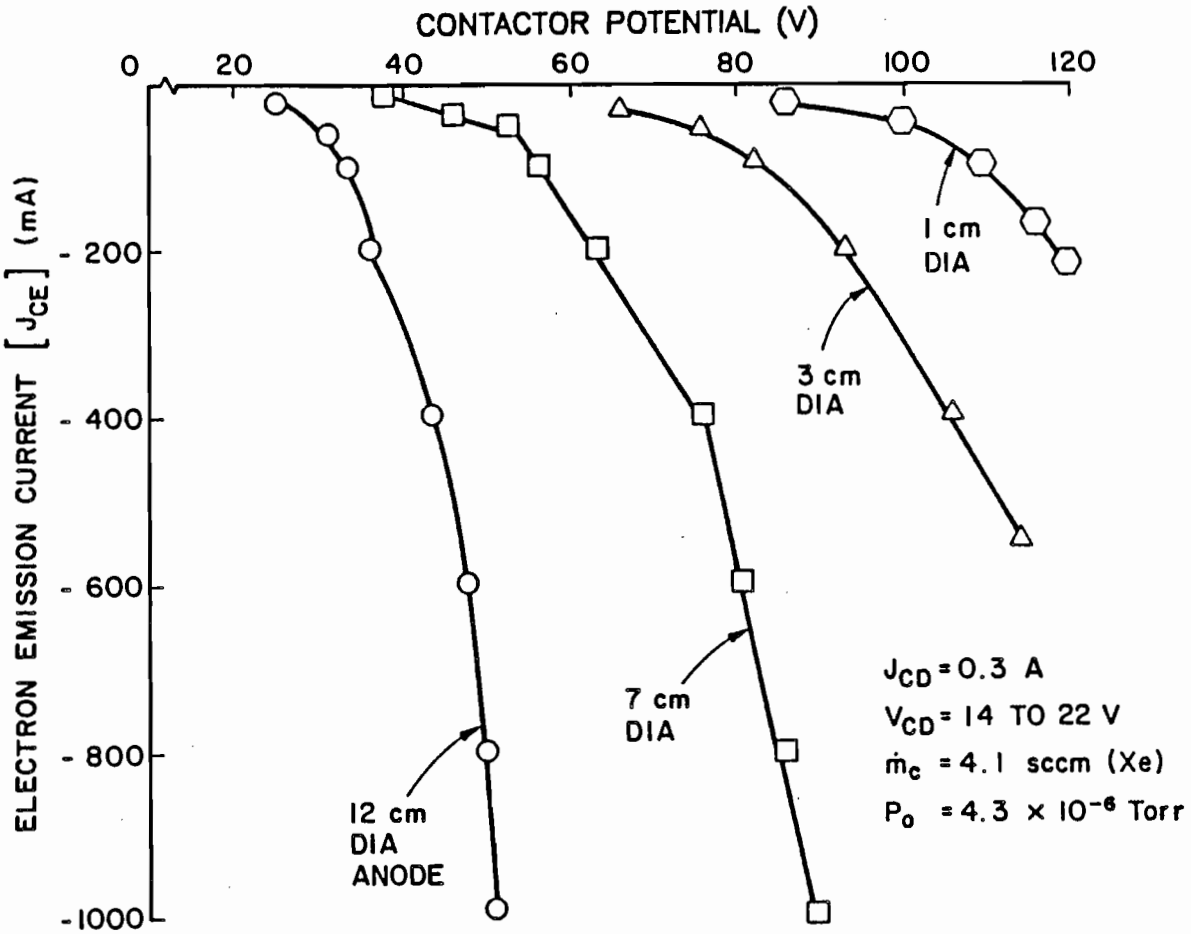

Fig. 3-15 Effect of Contactor Anode Diameter on Contactor Performance Curves

More elaborate one- and two-dimensional models have been developed of the electron collection process by Katz and Davis [17,18] which incorporate the phenomena observed in the ground-based experiments presented here. These models are in good agreement with experiment similar to the simple model presented in the preceding section. However, the more detailed models have predictive capabilities and, once they are calibrated against ground-based experiments, they can be used to model plasma contactor performance under space plasma conditions.

IV. THE ELECTRON EMISSION PROCESS

A. Experimental Observations

Some of the phenomena observed in ground-based studies of the process of electron flow from a hollow cathode-based plasma contactor to a low density ambient plasma can be explained using the typical plasma potential profile shown in Fig. 4-1. The contactor cathode, which was at zero axial position, was emitting 61 mA of electrons into an ambient background plasma located about 1 m downstream of the contactor. In the particular case of Fig. 4-1, the contactor cathode was actually 26 V below the ambient plasma potential. However, this is not obvious in Fig. 4-1 because potentials are shown as measured relative to the vacuum tank wall. A noteworthy feature of this potential profile is the hill structure that is present immediately downstream of the contactor. It is postulated that this potential hill develops because the densities of both neutrals and electrons (with sufficient energy to ionize them) are high near the cathode orifice. Under this condition, electrons that cause the ionization and the electrons produced would typically be expected to have substantial kinetic energies after the ionization event, and they would be expected to leave the region of ionization quickly. However, the more massive ions would be left behind thereby creating a region in which the ion density would tend to be greater than the electron density. This net positive space-charge density region would induce a potential hill like the one shown in Fig. 4-1. It should be noted that the plasma potential data of

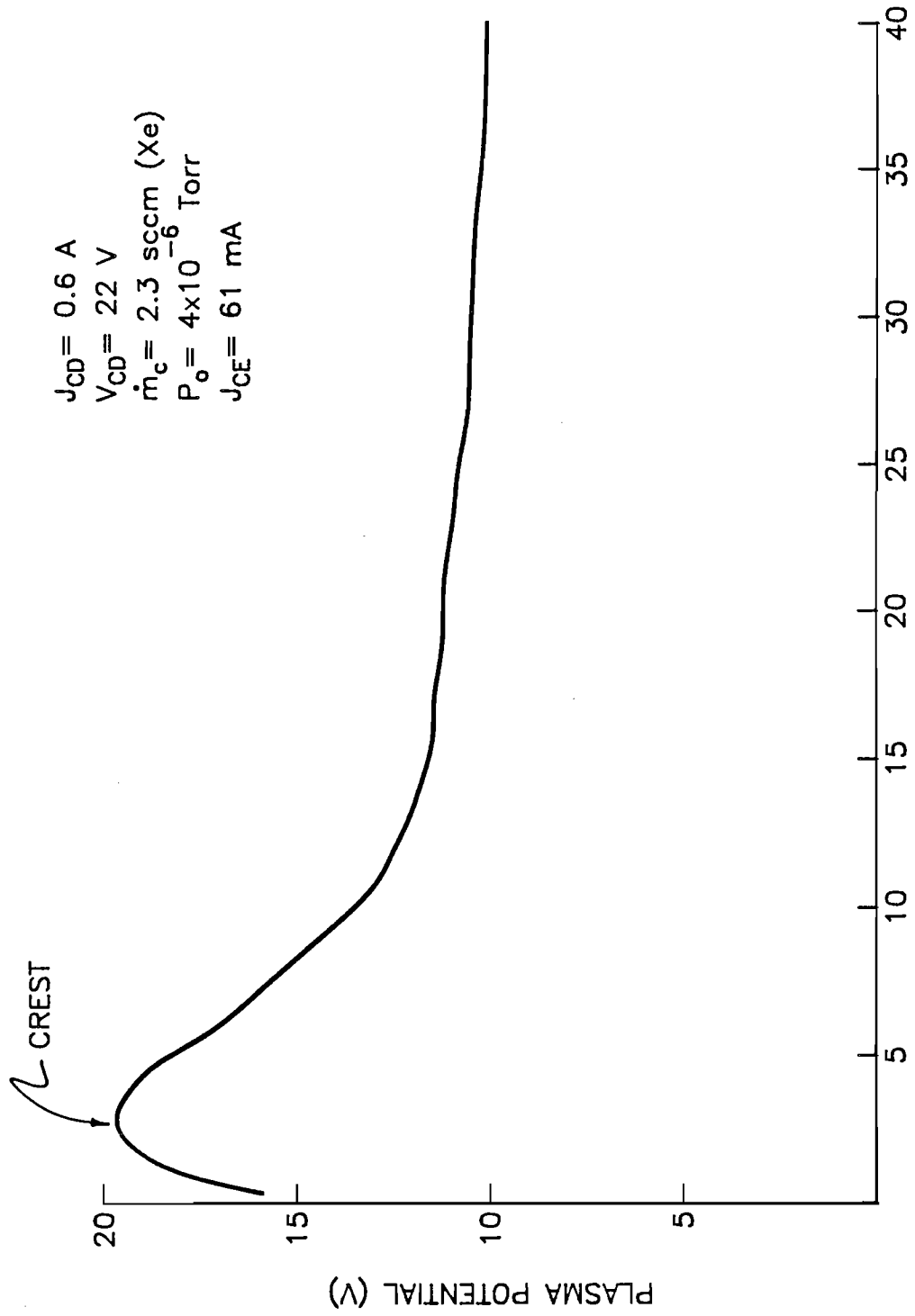

Fig. 4-1 Plasma Potential Profile on the Contactor/Vacuum Tank Centerline (Contactor Emitting Electrons)

Fig. 4-1 were obtained using a floating emissive probe, and these probes indicate potentials that fall progressively further below true plasma potential as they are moved into higher density plasmas [31]. Because plasma density is greatest at the hollow cathode orifice, the emissive probe probably indicates potentials that fall below actual values as the cathode is approached at Z=0. Hence, it is possible that the true crest of the hill is higher and located at a different axial position than the one indicated in Fig. 4-1.

A sufficiently low plasma density near the cathode was obtained for the operating condition shown in Fig. 4-1 by selecting a relatively low flowrate (2.3 sccm [Xe]) and electron emission current (61 mA). At this low plasma density condition it was possible to detect the potential hill using the emissive probe. As flowrate and/or electron emission current were increased, however, the potential hill sensed by the emissive probe began to disappear. In order to determine if this was due to emissive probe inadequacy or an actual reduction in the height of the potential hill, an RPA was positioned 20 cm from the contactor cathode, sighted on it and used to measure the energy characteristics of the ions coming from the vicinity of the contactor. Two typical traces recorded with the RPA so positioned along with their corresponding derivatives are shown in Fig. 4-2. These data were obtained with the contactor operating at a high flowrate (9.6 sccm [Xe]), where emissive probe measurements showed no evidence of potential hills at either the 130 or 1000 mA electron emission levels. The RPA curve and corresponding derivative for the high emission current case (J_{CE}= 1000 mA) indicate that two groups of ions are indeed present. The first group induces the peak occurring near 15 V in the lower plot and

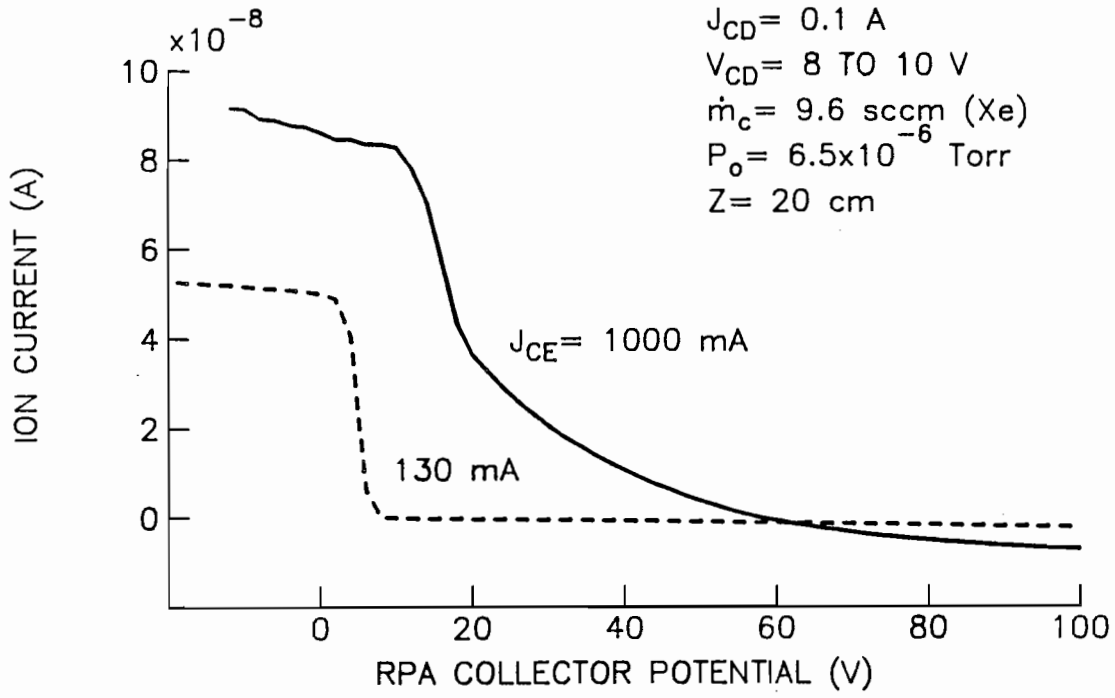

a. Current/Voltage Traces

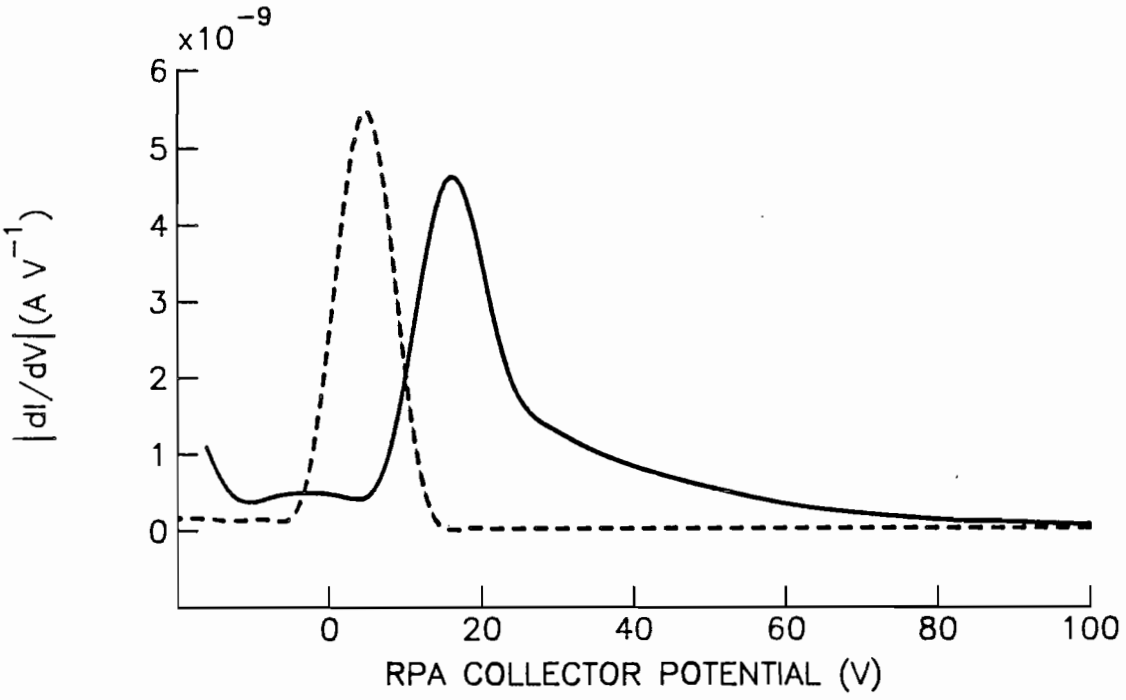

b. Derivatives of Current/Voltage Traces

Fig. 4-2 Retarding Potential Analyzer Data Measured in the Expanding Plasma Region (High Contactor Flowrate Condition)

represents low energy, thermal ions present in the expanding plasma. The second group which exhibits a greater energy spread is present as the tail on the solid curve extending from 20 to 100 V (Fig. 4-2b). It is postulated that the high energy ions associated with this tail are created on a potential hill located near the contactor cathode and that they flow from there to the RPA where they are detected. The RPA data corresponding to contactor operation at a low electron emission current of 130 mA shown in Fig. 4-2 displays only the one, low energy group of ions. Hence it is concluded that the potential hill is still present at the 1000 mA emission current operating condition and that it is not present at the 130 mA one.

There are other differences between the plasmas measured downstream of contactor at the 130 and 1000 mA emission currents and one of these, the difference in normalized electron energy distribution functions sensed by a Langmuir probe, is illustrated in Fig. 4-3. At a high emission current, the solid curve suggests that two electron groups exist. One group, associated with the lower energy peak, probably represents the thermal electrons present in the expanding plasma. The other, higher energy group contains electrons that have been accelerated from the contactor cathode through the potential hill region and into the expanding plasma without experiencing many energy dissipating collisions. The electron distribution function corresponding to the low emission current condition (J_{CE}=130 mA) indicates, on the other hand, that only one, low energy group of electrons is present. Thus, Figs. 4-2 and 4-3 show that both ions and electrons in the expanding plasma region exhibit distribution functions that have thermal and high energy components at a high emission current, while only the thermal component is present at a lower electron emission current.

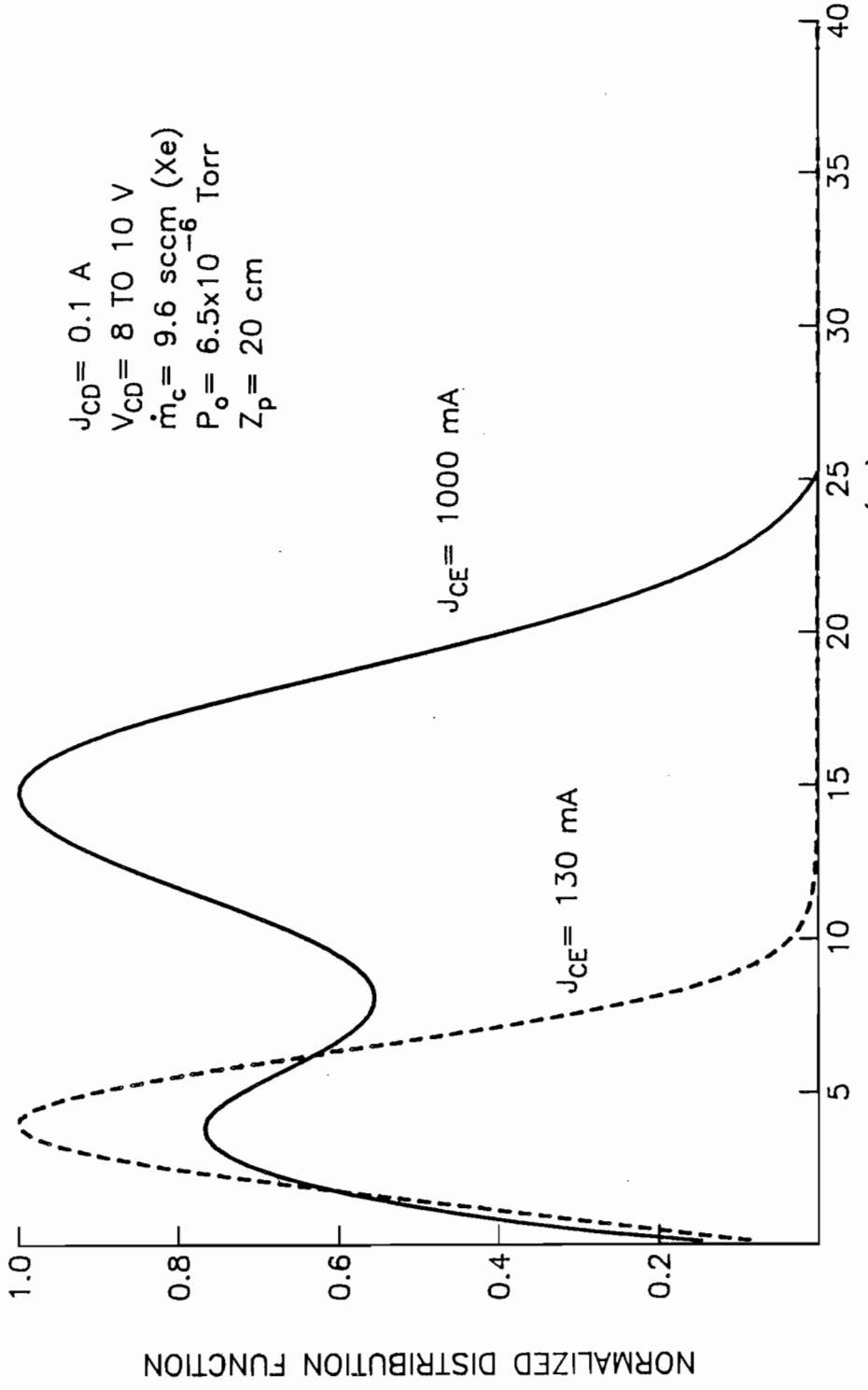

Fig. 4-3 Electron Energy Distributions Measured in the Expanding Plasma Region (High Contactor Flowrate Condition)

It is also of interest to examine the effect of electron emission current on the axial profiles of the high energy ion current density sensed by the RPA and the high energy (or streaming) electron current sensed by the Langmuir probe. These profiles have been measured over a range of electron emission currents and the results are shown in Fig. 4-4. The data in this figure correspond to a lower flowrate (4.1 sccm [Xe]) than those of Figs. 4-2 and 4-3. At this lower flowrate, high energy ions were detected flowing from the contactor at all four of the electron emission current levels shown (i.e. at J_{CE}= 126, 500, 1000 and 1500 mA). The lines drawn on the two plots in Fig. 4-4 correspond to an inverse square dependence with axial position.

The high energy ion current density is shown to follow the inverse square dependence (Fig. 4-4a) and this suggests that the high energy ions are expanding spherically from their point of creation. In addition, the streaming electron current flowing to the Langmuir probe also decreases as the inverse square of distance as shown in Fig. 4-4b. Eventually Fig. 4-4b shows that the streaming electron current begins to decrease faster than the inverse square at large values of axial position and high electron emission currents. This may be occurring either because the streaming electrons are being thermalized or their presence is being masked by thermal electrons. In general, however, the data presented in Fig. 4-4 suggest ions and electrons are expanding from what is essentially a point source near the potential hill. Because of this expansion behavior the region immediately downstream of the hill region is called the plasma expansion region.

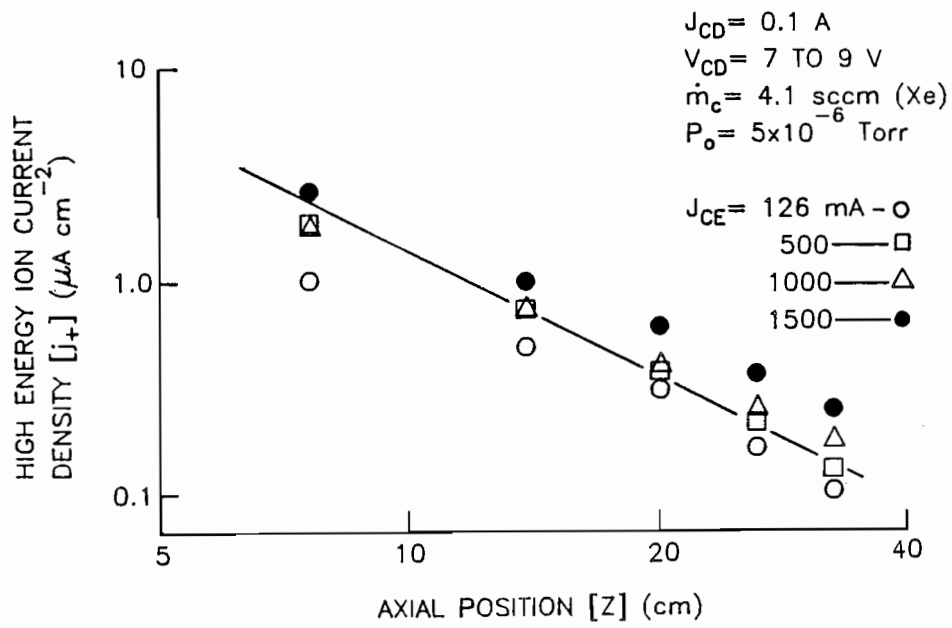

a. Effect of Electron Emission Current on High Energy Ion Current Density Profiles

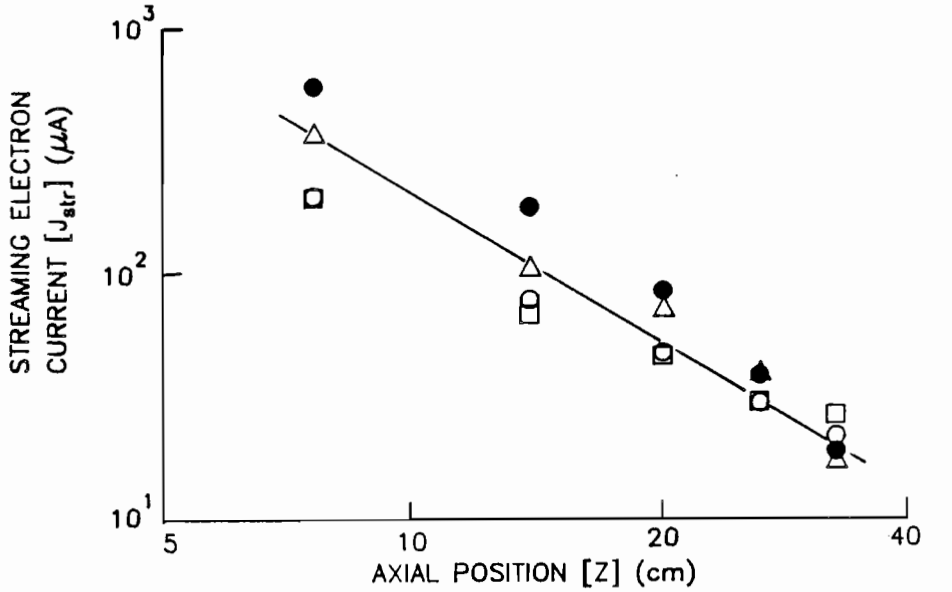

b. Effect of Electron Emission Current on Streaming Electron Current Profiles (streaming current flow to a 3.1 mm dia, spherical Langmuir probe)

Fig. 4-4 Experimental Observations Suggesting Spherical Expansion in the Region Downstream of the Potential Hill Structure

Both the high energy, directed ions and electrons present in the plasma expansion region can induce instabilities as they pass through the thermal plasma there and this can cause the plasma to be noisy or turbulent. A coarse measure of the turbulent intensity (the fraction of the energy in the expanding plasma that is in the form of turbulent electrostatic fluctuations) is equal to the square of the ratio of the rms plasma density fluctuation to the mean plasma density. This density ratio can be measured qualitatively in the low density expanding plasma by monitoring the current to a Langmuir probe when it is held near plasma potential and recording the rms noise amplitude/mean current ratio. Figure 4-5 shows rms-to-mean current ratio versus axial position data measured at the operating conditions of Figs. 4-2 and 4-3. The data for the 1000 mA operating condition suggest that the plasma is very noisy near the plasma contactor (turbulent intensity $\sim [0.32]^2 = 10\%$) and less noisy ($\sim 2\%$) further downstream. The opposite trend is indicated for the 130 mA operating condition. The noise levels at 33 cm are shown to be comparable at both currents thereby suggesting that phenomena occurring in the ambient plasma region determine the noise level at axial positions greater than ~ 30 cm.

B. Theoretical Development

In order to gain some understanding of the potential hills that have been measured at low emission currents and postulated at higher ones, a simple model of the electron emission process has been developed. Figure 4-6 shows a sketch of the postulated physical arrangement in spherical geometry and a hypothetical potential profile. The power needed to sustain the hill is assumed to come from the electron emission current J_{CE} flowing from the hollow cathode through the potential hill to a

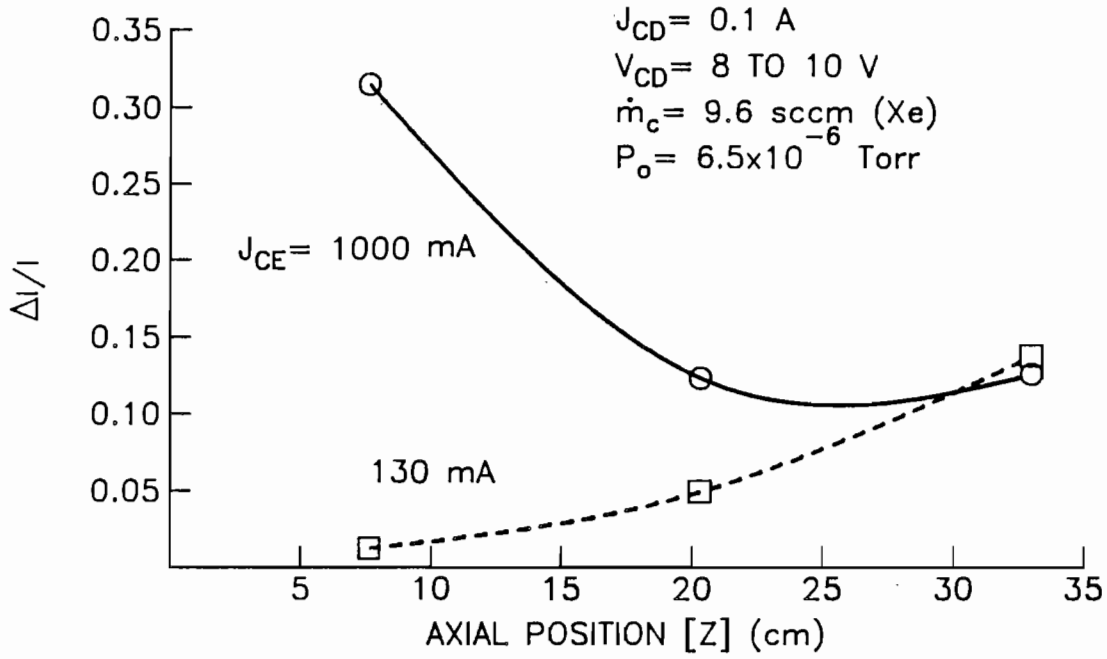

Fig. 4-5 Langmuir Probe Noise Levels at High and Low Electron Emission Currents (High Contactor Flowrate Condition)

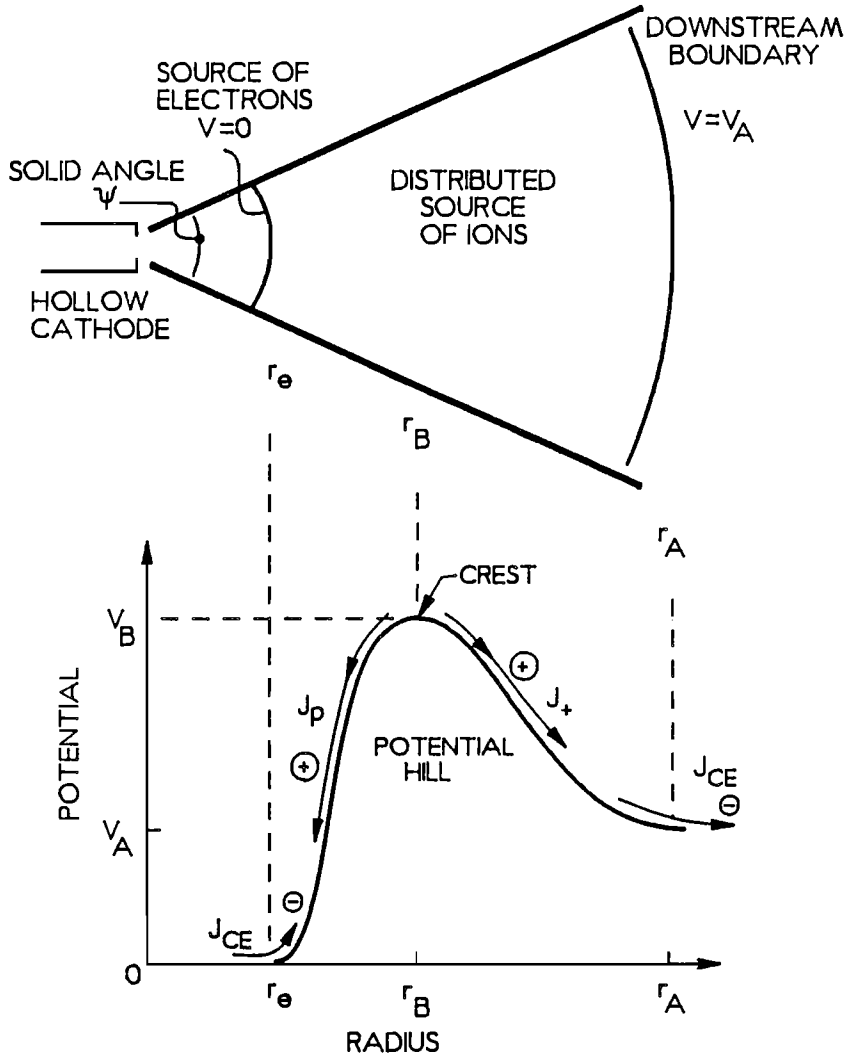

Fig. 4-6 Spherical Model Diagram of the Electron Emission Process

downstream boundary. As these electrons leave the source surface, they are accelerated up the potential hill and they gain sufficient energy to ionize neutral atoms. The resulting ions will flow down the hill from the point where they were produced. Ions produced to the left of the crest potential shown in Fig. 4-6 will flow to the cathode and those produced to the right of it will flow though the downstream boundary. The electrons, which accelerate to the crest and then decelerate after they pass it, will still have substantial kinetic energies as they pass the downstream boundary. They represent the streaming electrons mentioned in conjunction with Fig. 4-4.

The approach used to model this problem will be to write equations that describe the electron and ion densities throughout the region between the electron source and the downstream boundary and then apply Poisson's equation to solve for the associated potential profile. Because the electron and ion densities depend upon the potential profile, however, an iterative solution technique must be applied to accomplish this and obtain the steady-state, self-consistent solution for the density and potential profiles. This model of the electron emission process will be presented in terms of two sets of equations. One set will pertain to radial locations between the cathode and the potential peak (i.e. on the cathode side of the potential hill). The other set will pertain to radial locations between the potential hill and the downstream boundary (i.e. on the downstream boundary side).

The Cathode Side ($r_e < r < r_B$)

The electron density at any point in this region can be described approximately by assuming conservation of electron energy and current,

i.e.

$$\frac{1}{2}\, m_e\, [v_e(r)]^2 = e\, V(r) \qquad (4\text{-}1)$$

and

$$J_{CE} = e\, n_e(r)\, \psi\, r^2\, v_e(r) \qquad (4\text{-}2)$$

Combining these equations and solving for the electron density gives

$$n_e(r) = \frac{J_{CE}}{e\, \psi\, r^2} \sqrt{\frac{m_e}{2\, e\, V(r)}} \qquad (4\text{-}3)$$

This expression is only approximately correct because it ignores both electrons which are produced in ionization events and the effects of energy removal from the electron group due to ionization and other inelastic collisions. Neglecting these effects to make the problem more tractable limits its direct applicability to the case where the inelastic collision rate expressed as a current is small compared to the electron emission current. It is assumed that some mechanism for removing low energy electrons produced via ionization from the potential hill region is active. Although this mechanism is not defined, it is noted that the current of these electrons is typically very small compared to the emission current so a negligible fraction of the kinetic power in the streaming electrons would be required to remove them through elastic collisions.

The rate of ion generation per unit volume [R(r)] at radius r is given by

$$R(r) = n_e(r)\, n_o(r)\, \sigma_+(v_e)\, v_e(r) \qquad (4\text{-}4)$$

The ionization cross-sections of Rapp and Englander-Golden [32] were used to calculate ion generation rates. In addition, the neutral atom density n_0 appearing in this equation was modelled as the sum of the neutral densities due to the neutral flow from the hollow cathode (assumed to expand spherically from the orifice) and the background neutral density in the vacuum environment of the test. Specifically, the density n_0 at radius r was approximated by

$$n_o(r) = \frac{\dot{n}}{\psi_o \, r^2 \, v_{oc}} + \frac{P_o}{k \, T_o} \quad . \quad (4\text{-}5)$$

The density of ions at a radius r is determined by summing the contributions of all ions produced at radii of greater potential. Each of these ions will be accelerated from their point of creation r_1 to the radius of interest r. Hence, the contribution to the density of ions at a radial location r (for the region $r_e < r < r_B$) due to ions generated with a negligible initial velocity in a differential volume near r_1 is

$$dn_p(r) = r^{-2} \, \frac{R(r_1) \, r_1^2 \, dr_1}{v(r_1)} \quad (4\text{-}6)$$

and the velocity of the ions created at r_1 once they reach r is given by

$$v(r_1) = \sqrt{\frac{2e[V(r_1) - V(r)]}{m_p}} \quad . \quad (4\text{-}7)$$

The overall ion density at any radius r on the cathode side of the hill is now found by integrating the differential density dn_p from r to r_B. This yields

$$n_p(r) = r^{-2} \int_r^{r_B} \frac{R(r_1)\, r_1^2\, dr_1}{v(r_1)} \quad . \quad (4\text{-}8)$$

Combining Eqs. 4-3 through 4-8 and simplifying gives

$$n_p(r) = r^{-2} \frac{J_{CE}\sqrt{m_p}}{\sqrt{2}\,\psi\, e^{3/2}} \int_r^{r_B} \left[\frac{\dot{n}}{\psi_o r_1^2 v_{oc}} + \frac{P_o}{k\, T_o} \right] [V(r_1) - V(r)]^{-1/2} \sigma_+ \, dr_1 \quad . (4\text{-}9)$$

The electron and ion densities determined using Eqs. 4-3 and 4-9 can now be combined with Poisson's equation to describe the variation in plasma potential on the cathode side of the potential hill. Assuming spherical symmetry, Poisson's equation is

$$\frac{d^2V}{dr^2} + \frac{2}{r}\frac{dV}{dr} = \frac{e}{\varepsilon_o}\left(n_e(r) - n_p(r)\right) \quad . \quad (4\text{-}10)$$

In order to utilize the equations just developed, it is necessary to develop the equations describing conditions on the opposite (downstream boundary) side of the potential hill.

The Downstream Boundary Side ($r_B < r < r_A$)

Under the assumptions of this development, the equation that describes the electron density in the region between the potential crest and the downstream boundary is the same as the one developed for application upstream of the potential crest, namely Eq. 4-3. The ion density expression is obtained by repeating the logical sequence used to derive Eq. 4-9. It is found to differ from Eq. 4-9 only in the order of the integration, hence

$$n_+(r) = r^{-2}\,\frac{J_{CE}\sqrt{m_p}}{\sqrt{2}\,\psi\, e^{3/2}}\int_{r_B}^{r}\left[\frac{\dot{n}}{\psi_o r_1^2 v_{oc}}+\frac{P_o}{k\,T_o}\right][V(r_1)-V(r)]^{-1/2}\;\sigma_+\,dr_1 \quad (4\text{-}11)$$

Note that Eq. 4-11 shows an inverse square dependence with position and a linear dependence with emission current. This is in qualitative agreement with the functional dependencies indicated by the experimental data of Fig. 4-4a.

Equations 4-3, 4-9, 4-10, and 4-11 represent a relatively simple model of the electron emission process. They were solved by first dividing up the region r_e to r_A using closely and evenly-spaced node points. Next, the derivatives in Eq. 4-10 were approximated using finite-difference expressions. This allowed algebraic equations arranged in matrix form to be written for the potential at each node point. Electron and ion densities were then calculated at each node point using Eqs. 4-3, 4-9 and 4-11 and an initial estimate of the potential variation through the potential hill region. The procedure of solving for the densities and then the potentials at each node was repeated many times until the potential profile stabilized.

It should be noted that the solution procedure just described treats 1) the electron source location r_e, 2) the downstream boundary location r_A, 3) the solid angles ψ and ψ_0, and 4) the potential at the downstream boundary V_A as parameters. The electron source and downstream boundary locations are, however, not free parameters. The values of r_e and r_A are established physically by the requirement that the electric fields be zero at these locations (i.e. the space-charge limited condition applies). It was postulated that the other parameters, namely the downstream boundary potential V_A, and the solid angles ψ and ψ_0 were influenced by

such factors as the cathode orifice size, the anode configuration, and the plasma conditions beyond the downstream boundary and they were treated as free parameters. It is believed that an energy balance analysis could be used to find the downstream boundary potential, but this was not done in this preliminary study. In order to apply the model and compare its predictions to experimental observations, V_A was set at the experimentally measured potential in the expanding plasma region (typically measured at a radius of 20 cm) for each electron emission operating condition studied. The solid angles ψ and ψ_0 were arbitrarily set to 2π (corresponding to hemispherical geometry). There are other parameters appearing in Eqs. 4-3, 4-9, 4-10, and 4-11 that are not determined explicitly through the analysis (e.g. P_0 and T_0), but they were controlled during the experiment and unique values could be assigned to them.

Numerical Example

When Eqs. 4-3, 4-9, 4-10, and 4-11 were solved for the case of an emission current of 1 A and values of the parameters given in Table 4-1, the theoretical potential profile shown in Fig. 4-7a was computed. By forcing the boundary electric fields at r_e and r_A to be zero, the electron source and downstream boundaries were found to be located at 4.6 and 14.4 mm, respectively, and a crest potential of 153 V was computed at 7.4 mm. This large potential was caused by the anticipated net positive (ion) charge density in the region between 5 and 11.5 mm as shown in Fig. 4-7b. The neutral atom density variation throughout the potential hill region is shown in Fig. 4-7c. When this information was combined with the data shown in Figs. 4-7a and 4-7b the ion production rate per unit volume was calculated and it is plotted in Fig. 4-7d. By integrating the volumetric ion production rate over the entire

Table 4-1 Numerical Example Data Set

Inputs	Outputs
J_{CE} = 1.0 A	Fig. 8
$\dot{m}_c$ = 4.1 sccm (Xe) (i.e. $\dot{n}$ = 1.72×10^{18} s^{-1})	J_+ = 1.94 mA
P_o = 5.0×10^{-6} Torr (i.e. 6.7×10^{-4} Pa)	J_p = 2.16 mA
T_o = 300 K	r_e = 4.6 mm
v_{oc} = 458 m s^{-1}	r_B = 7.4 mm
$\psi = 2\pi$	r_A = 14.4 mm
$\psi_o = 2\pi$	V_B = 153 V
V_A = 22 V	

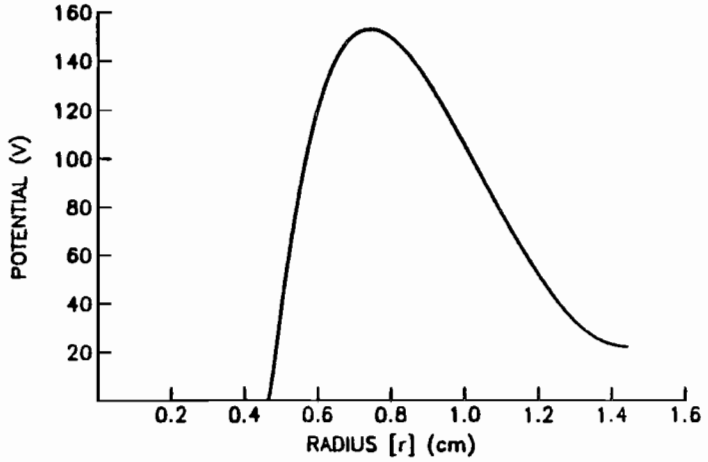

a. Potential Profile

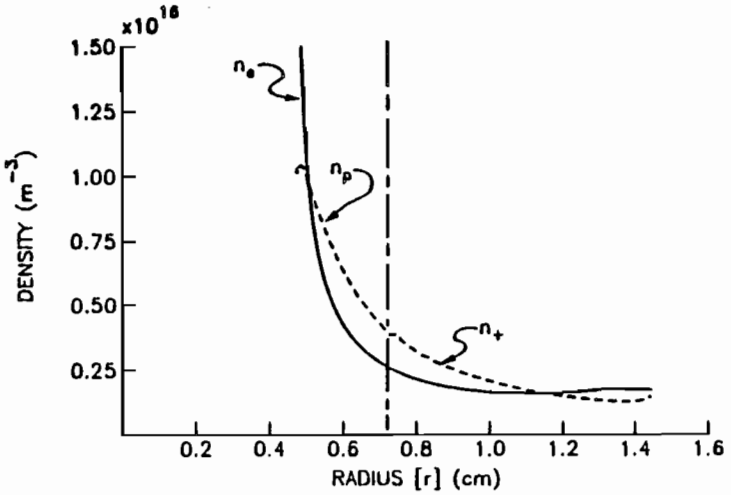

b. Charged Particle Densities

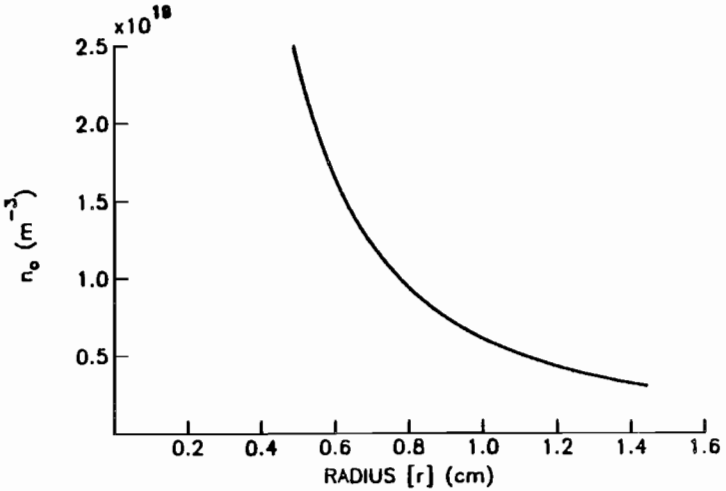

c. Neutral Density

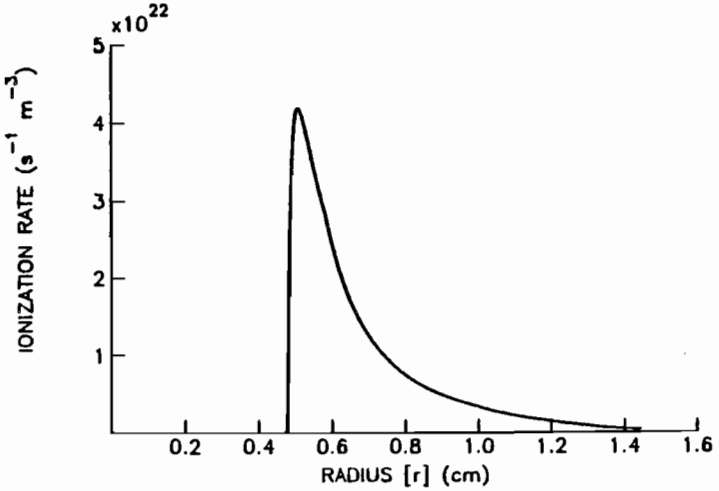

d. Ion Production Rate

Fig. 4-7 Typical Computed Electron Emission Results

volume of the potential hill region, the total ion current flowing from this region was calculated to be 4.10 mA. This ion current could be broken into components of 1.94 mA (J_+) and 2.16 mA (J_p) flowing from the potential hill region to the downstream boundary and to the electron source boundary, respectively. These ion creation rates (expressed as currents) are small compared to the emission current. This suggests that the assumptions made in deriving this model are probably valid and that very little power should be required from the streaming electrons to remove low energy electrons (resulting from inelastic collisions) from the potential hill as they are produced.

C. Comparison of Theory and Experiment

The procedures used to obtain the numerical results given in Table 4-1 and Fig. 4-7 were applied to obtain additional solutions over ranges of electron emission currents and flowrates. The effect of electron emission current and flowrate on the current density and maximum energy of ions flowing away from the hollow cathode discharge were also measured using the RPA described previously. The experimentally measured and theoretically predicted effect of emission current on these quantities are compared in Fig. 4-8 under conditions where the RPA was positioned at 20 cm downstream of the contactor. Figure 4-8a shows the high energy ion current density increasing with electron emission current, at a lesser slope than the "theoretical" curve. The theoretical predictions of high energy ion current density were made by first finding the ion current emitted from the potential hill region to the downstream boundary for the particular electron emission current as explained in the numerical example associated with Table 4-1 and Fig. 4-7. Next, this current was

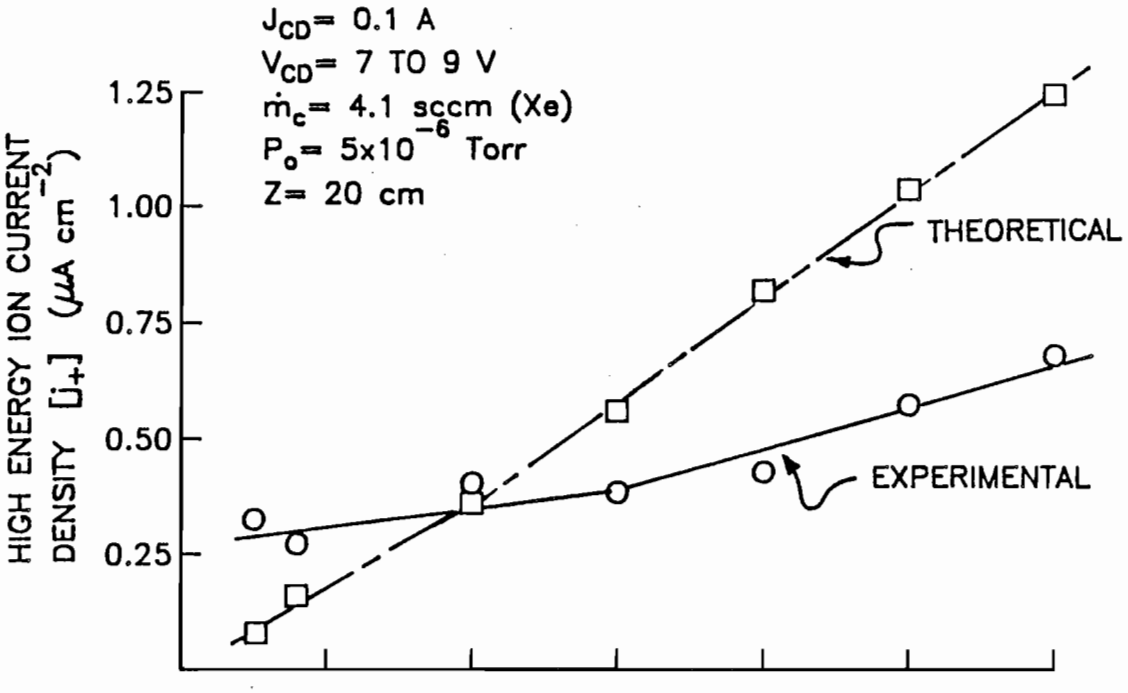

a. Ion Current Density

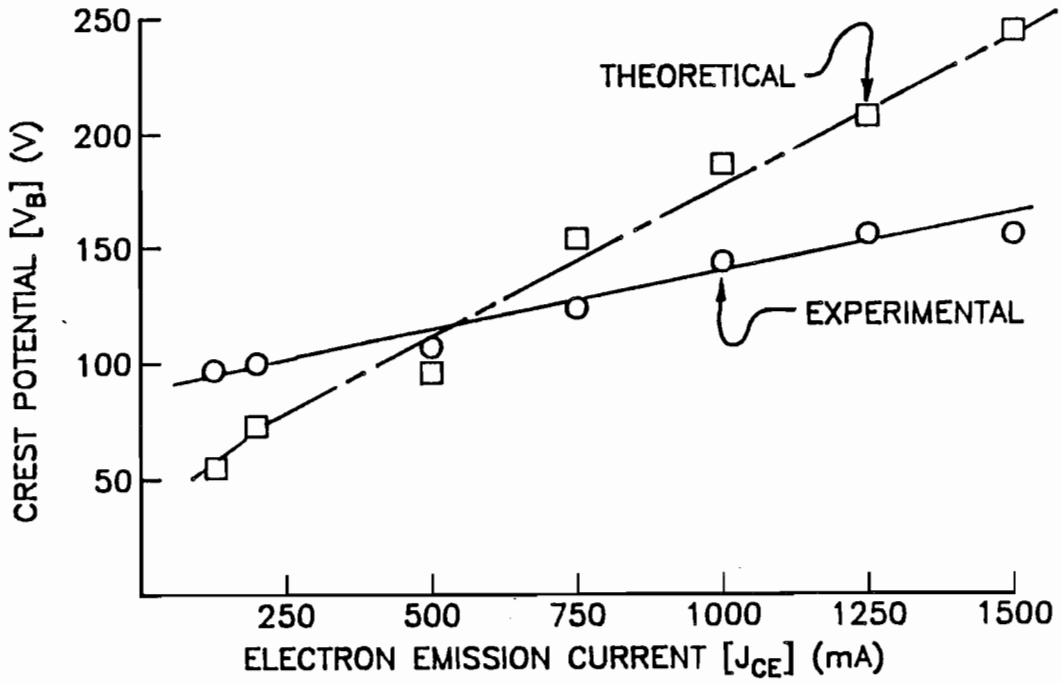

b. Crest Potential

Fig. 4-8 Computed Effects of Emission Current

divided by the surface area at a radius of 20 cm (i.e. $\psi r^2 \approx 2\pi[20]^2 \approx 2500$ cm^2) to obtain the current density at this location. Although the two curves shown in Fig 4-8a do not coincide, the agreement between the experiment and numerical model is considered to be good considering the assumptions made in the model. Uncertainties in experimental conditions as well as in the ionization cross sections could easily cause the level of error indicated in Fig. 4-8a. It is noted that better agreement could be achieved artificially in this simple one-dimensional model by adjusting the solid angle ψ with each electron emission current. However, it is felt that two-dimensional (or possibly three-dimensional) effects probably determine the subtle trends in the experimental data so attempts to adjust ψ to obtain better agreement cannot be justified.

Figure 4-8b contains a comparison of experimentally and theoretically determined crest potentials. Again, relatively good agreement and a similar trend for the crest potential to increase with electron emission current for both curves is shown. The computed positions of r_e, r_B, and r_A at the electron emission levels corresponding to Fig. 4-8 are shown in Fig. 4-9. The most notable trend in this figure is that larger values of r_A correspond to smaller values of electron emission current. Together with Fig. 4-8b, this suggests that not only are crest potentials greater at higher electron emission currents, but electric field strengths are also higher. Although it was generally not possible to measure the radii identified in Fig. 4-9 in the experiments, it is noted that the data of Fig. 4-1 (and visual estimations of the extent of the luminous region immediately downstream of the contactor) agree to first-order with the computed radii of Fig. 4-9.

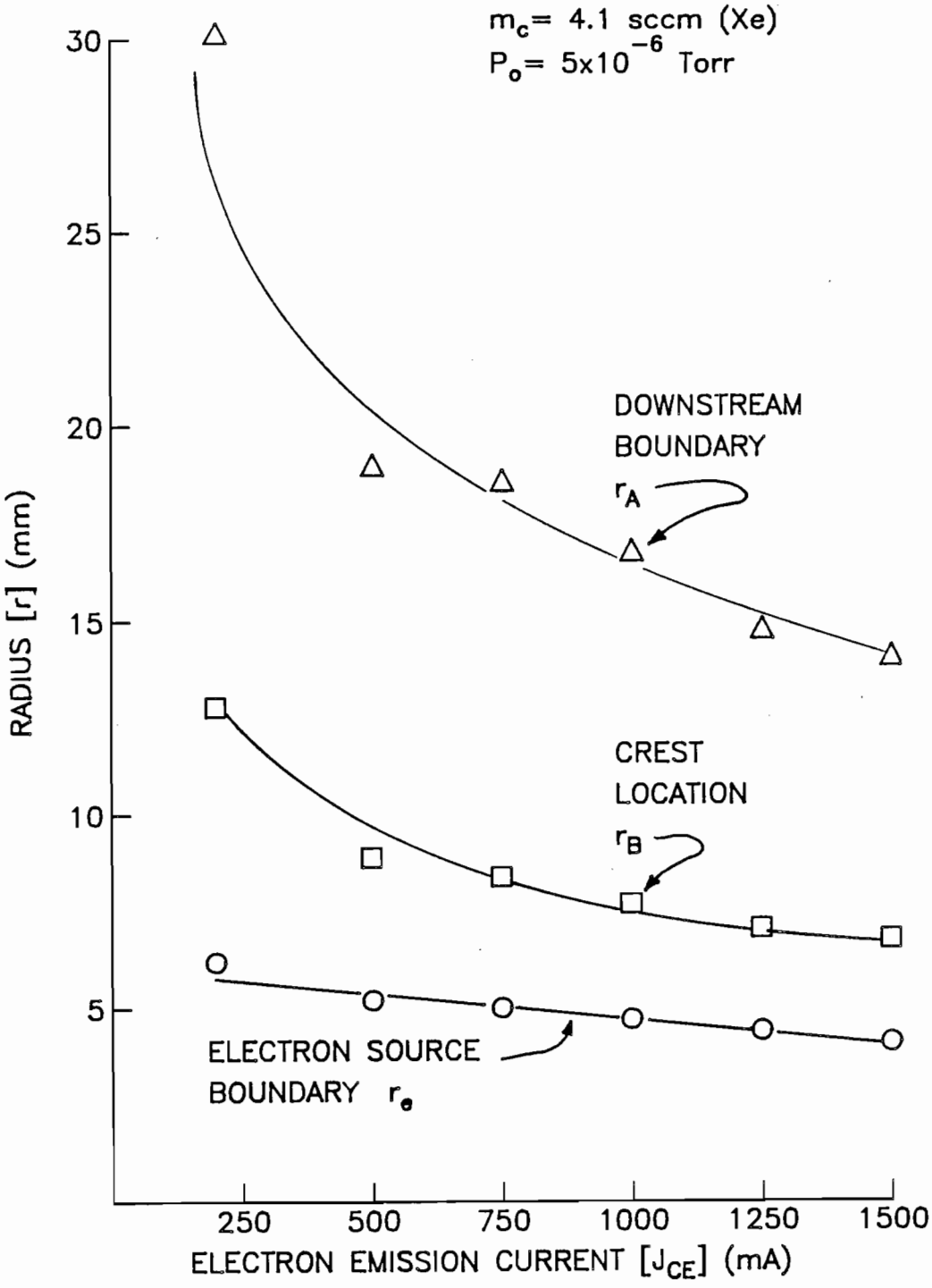

Fig. 4-9 Computed Values of Downstream, Crest and Electron Source Boundaries as Functions of Electron Emission Current

The effect of contactor flowrate on the experimentally measured and theoretically predicted high energy ion current and crest potential are shown in Fig. 4-10. The theoretical predictions (triangular and solid circular data points) and experimental measurements (circular and square data points) of high energy ion current density corresponding to the 130 and 1000 mA electron emission levels are shown to exhibit comparable magnitudes in Fig. 4-10a. The theoretical crest potential data for the 1000 mA condition shown in Fig. 4-10b also show good agreement with experiments, and the predicted and measured crest potentials show a similar trend (both decrease with flowrate). However, the predicted and measured crest potentials corresponding to the 130 mA condition do not show the same trends. Note that current density measurements made at an electron emission current of 130 mA (shown in Fig. 4-10a) indicate, at a contactor flowrate of 9.6 sccm, that no high energy ions are present. At this high flowrate and low electron emission level, apparently no potential hill structure is needed to assist electron emission from the high density plasma near the contactor hollow cathode. Numerical modelling of the 130 mA condition was impossible to perform at the higher flowrates of 8 and 10 sccm and, in order to obtain a steady solution, the downstream potential V_A had to be artificially increased to ~ 14 V (from ~ 8 to 10 V) to realize a convergent solution. Consequently, these data points were not included on Fig. 4-10. For the convenience of the reader, the computed values of r_e, r_B, and r_A corresponding to Fig. 4-10 are shown in Fig. 4-11. In this figure higher flowrates are shown to induce larger radii and these radii increase linearly with flowrate.

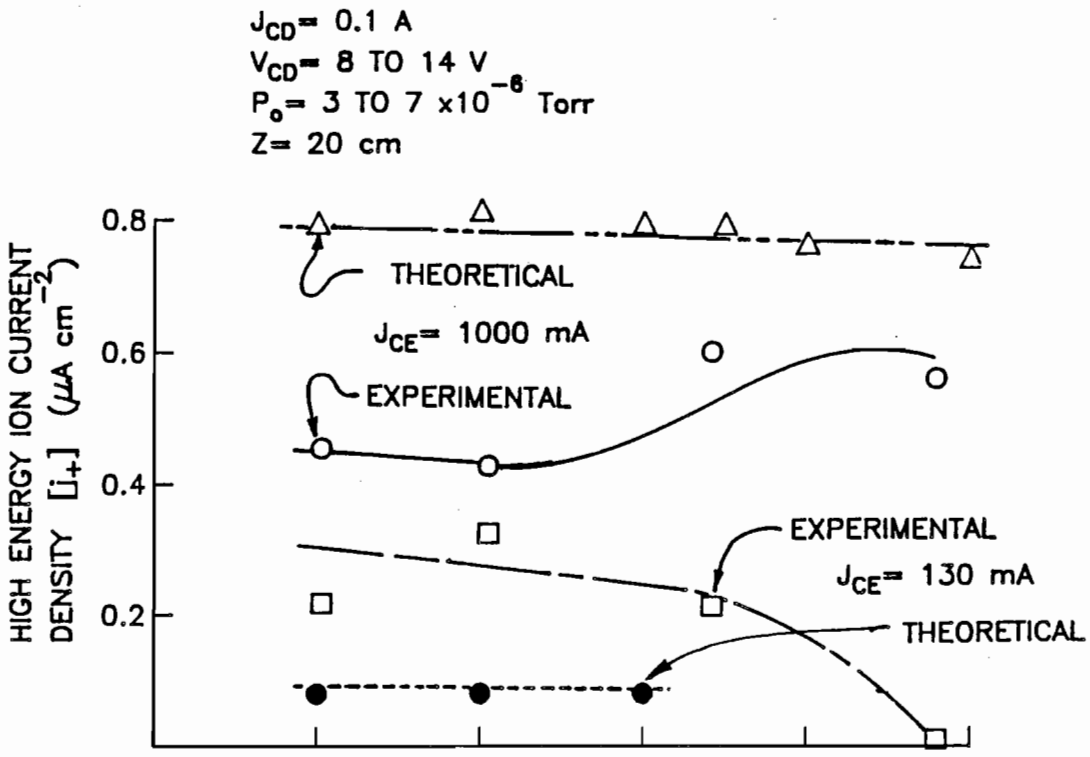

a. Ion Current Density

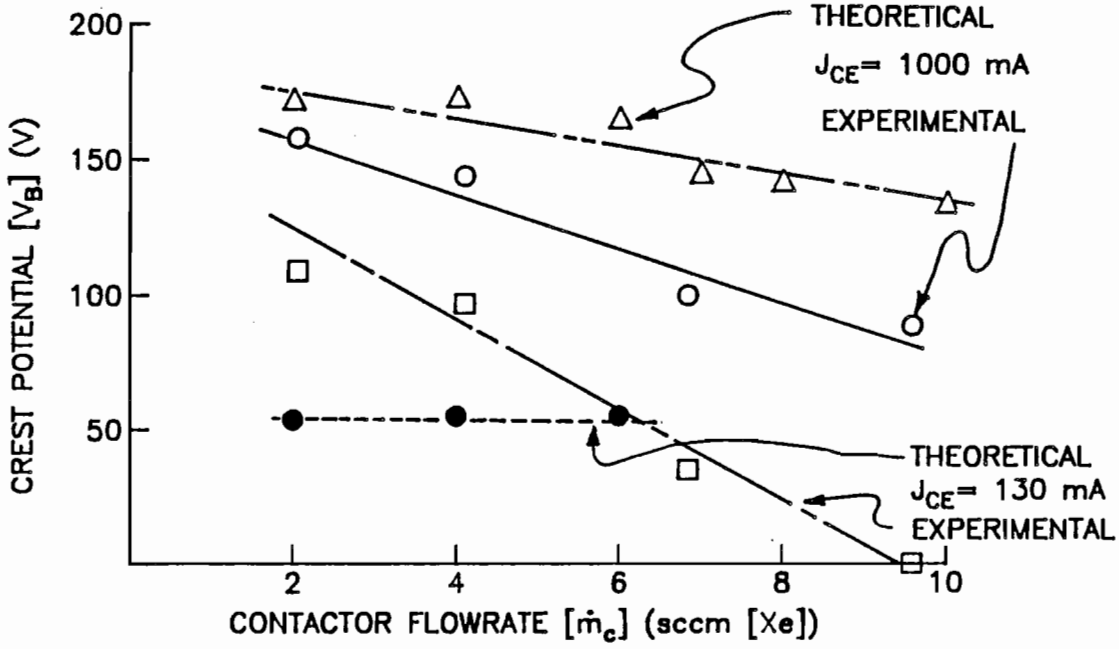

b. Crest Potential

4-10 Computed Effects of Contactor Flowrate

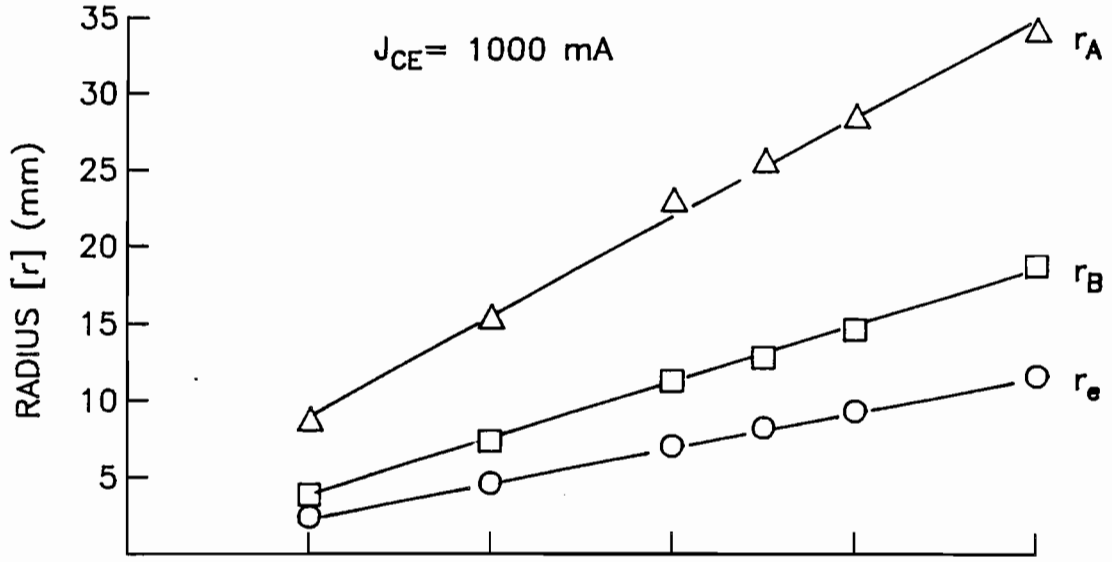

a. High Electron Emission Current Condition

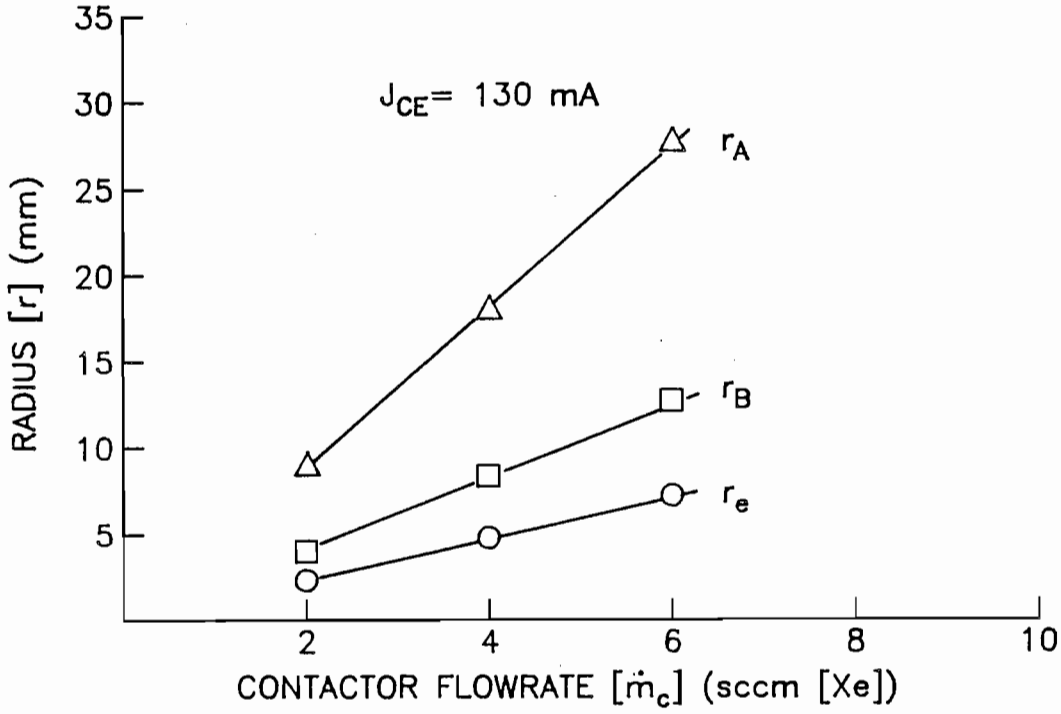

b. Low Electron Emission Current Condition

Fig. 4-11 Computed Values of Downstream, Crest and Electron Source Boundaries as Functions of Contactor Flowrate

Beyond the potential hill shown in Fig. 4-1 there is additional structure (shown in more detail in Fig. 4-12) that could affect the electron emission behavior of the contactor. For example, the plasma potential is relatively constant in the region from 15 to 60 cm. This region is called the plasma expansion region because the plasma density decreases in proportion to Z^{-2} there [33]. Generally, it appears that the plasma overexpands in this region. This is demonstrated by Langmuir probe data [33] which show that the plasma density at the downstream end of the plasma expansion region is below that in the ambient plasma region (the region of constant plasma potential extending beyond 100 cm in Fig. 4-12). It appears that the intermediate double layer (shown between 60 and 100 cm) enables accommodation of this difference in plasma densities. The criteria that determine the location, geometry and size of the intermediate double layer probably depend upon the ion creation and loss rates in the ambient and expanding plasma regions, the ion and electron current densities, and interactions with the vacuum test facility walls. However, the details of its characteristics have not been investigated.

Several experimental observations have been made which suggest that fundamentally different phenomena occur at certain emission current and contactor flowrate condition ranges. For example, high emission current and/or low flowrate operating conditions induce higher noise levels, higher anode voltages, and generation of energetic ions when compared to low emission current and/or high flowrate operating conditions. At low emission currents and high flowrate conditions a small, relatively bright (luminous) spot is observed just downstream of the contactor orifice. Operation of a hollow cathode discharge under these conditions has been termed the

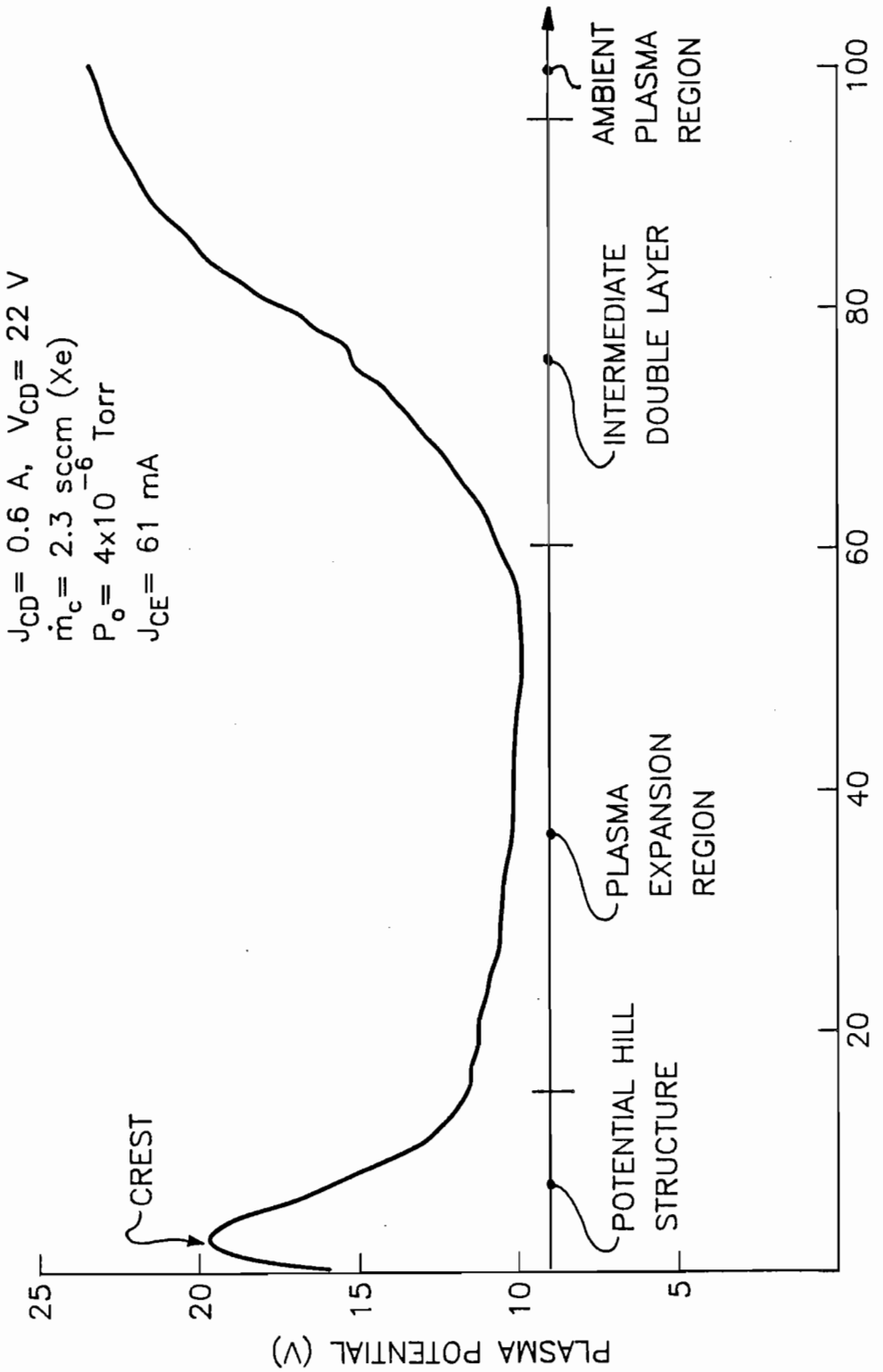

Fig. 4-12 Plasma Potential Profile on the Contactor/Vacuum Tank Centerline (Contactor Emitting Electrons)

"spot mode" [19], and a potential hill is not present under these conditions. Conversely, at high emission currents or low flowrates, a rather large (several cm in extent) luminous region develops downstream of the contactor cathode. Operation of a hollow cathode under these conditions has been termed the "plume mode" [19]. A majority of the experimental evidence presented here has been collected in the plume mode of operation, and the model has been developed to describe this operational mode. However, transitions from the plume to spot modes have also been observed experimentally and, in addition, the model appears to break down close to the operating condition corresponding to the spot mode. It is possible that operation in the spot mode occurs at high flowrates when the neutral density is very high near the contactor orifice region because the electrons suffer many kinetic energy degrading collisions here and cannot acquire the streaming energies needed to induce substantial ionization and create a potential hill.

V. CONCLUSIONS

A simple, first-order model of the electron collection process based on the assumption of spherical symmetry has been developed and shown to agree with experimental results. The essential elements of the model reflect an experimentally observed double layer that develops between the plasma produced by the contactor and the ambient plasma. The inner boundary of the double layer is located at a position where ion losses through the sheath will satisfy both the Bohm sheath stability criterion and the space-charge limit on ion extraction. The outer boundary of the double layer is located such that its surface area is sufficient to collect the electron current being demanded from the random current density in the ambient plasma. The voltage drop across the double layer is determined by the fact that both the ion and electron currents that counterflow through the double layer do so at their space-charge limited values. More elaborate one- and two-dimensional models of the electron collection process have also confirmed the basic processes described above and have been shown to agree well with experimental results.

From the experimental results presented, contactor performance (as reflected in the potential difference between the contactor and the ambient plasma) is shown to improve when contactor flowrate and/or anode diameter are increased. The performance improvement induced by increasing the flowrate can be explained using the simple model by recognizing that higher ion production rates are induced

throughout the contactor cloud due to higher concentrations of neutrals and that these additional ions have a greater likelihood of migrating to the sheath. This increase in ion flow causes the contactor cloud to expand and this in turn increases the double layer radius ratio and causes the double layer potential drop to decrease. Although the simple model agrees with experiment when the contactor plasma cloud/double layer boundaries are nearly spherical, it does not describe the decrease in performance induced by decreasing the anode diameter. It is possible that two-dimensional geometrical effects not reflected in the model become important when the anode diameter is more than a few times smaller than the double layer outer boundary.

Experimental observations of a hollow cathode-based plasma contactor emitting electrons to a ambient plasma suggest that a potential hill structure develops close to the contactor cathode. It is postulated that the potential hill is created by a region of positive space charge and ions produced in this region can gain substantial energies as they are accelerated away from their point of production. By measuring the energies of these ions, the height of the potential hill can be inferred. In general, an increase in contactor flowrate tends to reduce the potential at the crest of the hill, while larger emission current levels tend to increase it.

A simple model that reflects the effects of ionization, ion and electron acceleration and the space-charge induced by the ions and electrons describes the essential features derived from experimental observations of hollow cathodes emitting electrons. Specifically, it yields magnitudes of potential hill height and current density of ions flowing from the potential hill that agree with experimental results.

Further, the predicted effects of electron emission current and contactor flowrate on these features agree with experimentally observed trends. It is noted that the total current of ions emitted to the expanding plasma is estimated to be small compared to the electron emission current (i.e. typically less than 0.2 %). This suggests that only a small fraction of the electrons flowing from the contactor to the expanding plasma interact with and possibly ionize neutral atoms while they stream through the potential hill region.

VI. SUGGESTIONS FOR FUTURE RESEARCH

A valid criticism of the work presented in this dissertation is that magnetic field effects on plasma contactor phenomena have not been investigated experimentally and, consequently, an obvious suggestion for future research would be to investigate their effects. Some preliminary experimental results have been obtained [34], however, and they will be presented here to motivate discussion. The experiments were conducted in a cylindrical chamber (2 m dia. by 4 m long) located at the Institute of Interplanetary Space Physics (IFSI) in Frascati, Italy [35]. In this facility, the separation distance between the contactor and simulator was maintained at 2.7 m, the electrical connections were identical to those shown in Fig. 2-3, and the same contactor and discharge chamber simulator devices were utilized. However, in this facility, the magnetic field present in the region between the contactor and simulator could be controlled in both magnitude and direction by large Helmholtz coils which encircle the IFSI stainless steel chamber. In order to study its effect on the plasma contacting process, various magnetic field configurations were imposed. They included 1) a zero magnetic field, the geo-magnetic field was nulled; 2) axial fields, those directed along the axis joining the contactor and simulator; and 3) transverse fields, those aligned perpendicular to the axis joining the contactor and simulator.

The effects of magnetic field on the contactor plasma cloud and double layer at several axial and transverse magnetic field conditions can be seen by comparing the data displayed in Fig. 6-1. Figure 6-1a shows that the contactor plasma cloud extends further downstream and the double layer voltage drop increases from zero to 55 V as the electron collection current is increased from 50 to 200 mA in a 1 G axial field environment. This observation is in agreement with the unpublished results of previous electron collection experiments conducted at CSU and LeRC when low contactor flowrates were used and no ignited mode transition was observed. It is noted that results similar to those shown in Fig. 6-1a were also obtained when the magnetic field was set to zero.

Figure 6-1b shows plasma potential profiles obtained at a 1 G transverse magnetic field condition. The profile corresponding to 50 mA of electron collection displays one double layer. However, as the electron collection current is increased to 100 and 150 mA, two double layers develop. In addition to multiple double layers occurring at higher electron collection currents, higher plasma noise was also observed and, in general, the noise level tended to be greatest through the multiple double layer regions and much lower close to the contactor and in the ambient plasma regions. Unfortunately, the noise measurements were very crude and quantitative values can not be given. One particular direction for future work would be to measure the noise levels and their spectral distribution under both axial and transverse magnetic field orientations.

The maximum magnetic field that could be induced in the IFSI facility was 1.6 G, and plasma potential profiles corresponding to a transverse field of this

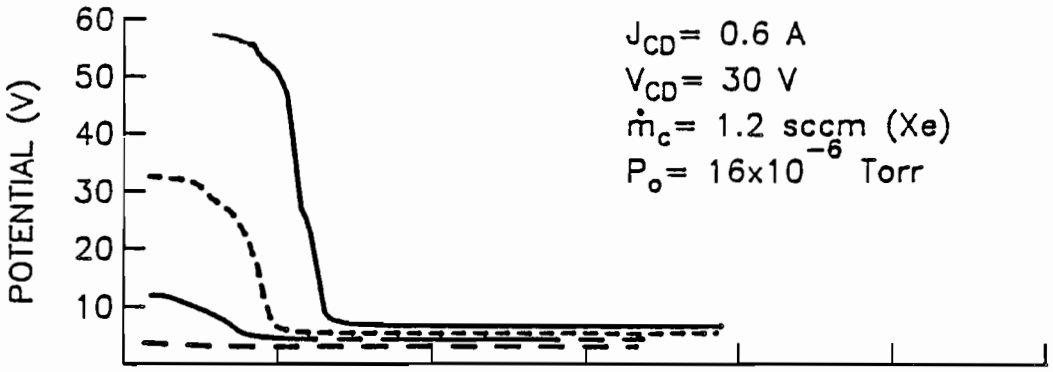

a. 1.0 G Axial Magnetic Field (i.e. $B_{//}$ = 1.0 G, $B_{\perp}$ = 0 G)

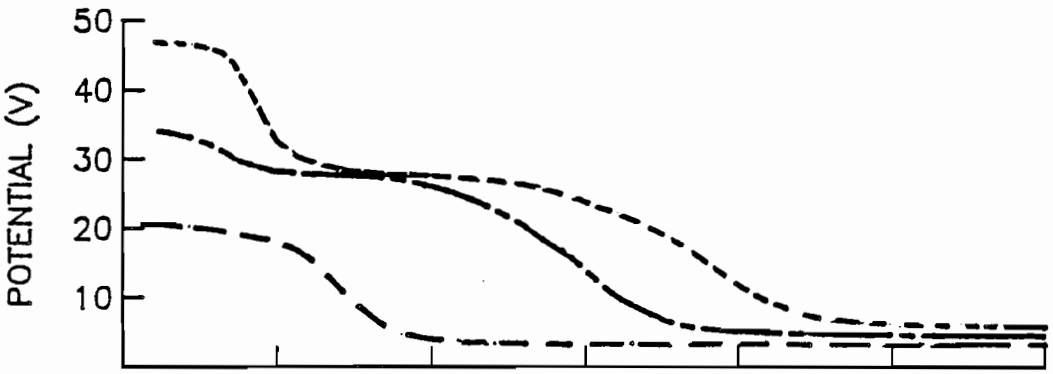

b. 1.0 G Transverse Magnetic Field (i.e. $B_{//}$ = 0 G, $B_{\perp}$ = 1.0 G)

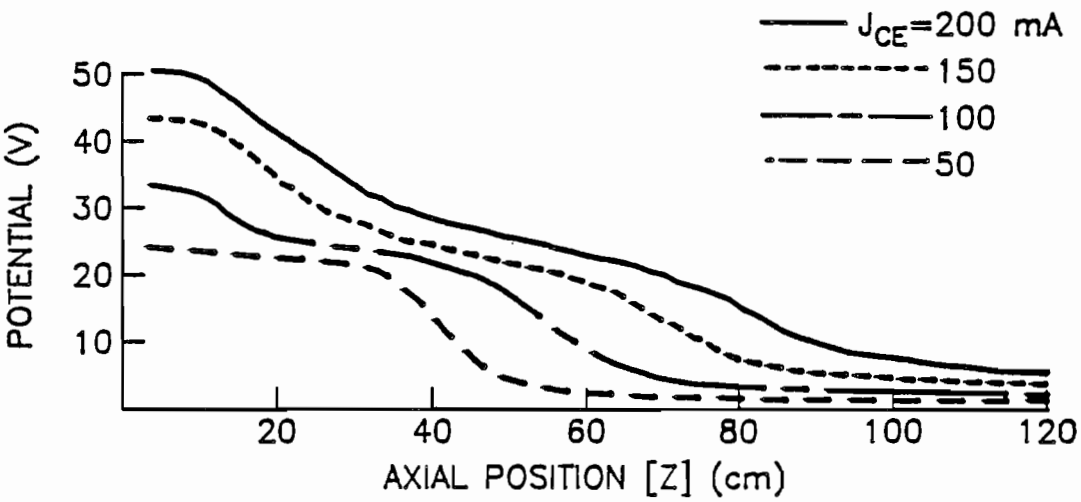

c. 1.6 G Transverse Magnetic Field (i.e. $B_{//}$ = 0 G, $B_{\perp}$ = 1.6 G)

Fig. 6-1 Effect of Electron Collection Current on Plasma Potential Profiles for Several Different Magnetic Field Conditions

magnitude are shown in Fig. 6-1c. The low electron collection current of 50 mA shows a single well-defined double layer which develops between 35 and 45 cm. At higher currents of 100, 150, and 200 mA, two double layers, which are less well-defined and extend further downstream, are shown to develop. In addition, as the current is increased, the total voltage drop across the double layer increases. This suggests that the transition to the ignited mode of operation has not occurred, or that it is being inhibited by the presence of the 1.6 G transverse magnetic field. Experiments in which even higher magnetic field strengths are used should be conducted in order to generate an experimental data base. This experience could then be used to verify existing theoretical models of the plasma contacting process that include effects of magnetic fields [16]. Specifically, these experiments could be used to determine critical data like turbulence levels (and their spectral distributions) and the extent to which oblique (with respect to the magnetic field) double layers will develop. This information could then be used to calibrate the numerical models which incorporate magnetic field effects, and allow realistic predictions to be made about how plasma contactors will operate in low Earth orbit applications.

In regard to electron emission phenomena, experiments and numerical simulations that investigate the effects of background neutral density, expellant gas, cathode orifice size, could be performed. In addition, more work could be performed to study the transition between the plume and spot modes, and how the parameters listed above affect this transition. This information could be important in hollow cathode applications where long lifetimes and high emission current levels are necessary. For example, if the main discharge hollow cathode of a high power

plasma contactor [36] began to operate in the plume mode, then energetic ions could bombard its interior structures, erode them, and cause the contactor to fail.

Finally, it should be recognized that an ideal experimental simulation of the in-space plasma contacting process would involve similarity of not only the current levels and contactor hardware involved, but also the space environment. Complete simulation of this environment implies 1) similar ambient ionic/atomic species concentrations, 2) similar ambient plasma density and temperature levels, 3) similar magnetic field intensity and relative contactor/magnetic field velocity conditions, and 4) an ambient plasma that is not perturbed by vacuum chamber walls or other apparatus during the conduct of the tests. In the present study these conditions have in general not been met. Experiments that employ more accurate simulation of space conditions should be performed in order to determine if they will adversely affect plasma contactor operation.

While some effects of changes in magnetic field strength on the plasma contacting process have been examined (as discussed above), the effects of its relative motion at space plasma density conditions are not reflected in any laboratory tests of plasma contactors. It is noted, however, that Stenzel and Urrutia [37] have developed a technique to perform experiments that simulate the relative motion of a tethered satellite system moving through a magnetized plasma. Unfortunately, no active plasma generating devices were placed on the electron collecting and electron emitting surfaces, but it may be possible to employ their technique to an experiment which tests the effectiveness of a plasma contactor under simulated motion relative to a magnetized plasma.

Finally, it is suggested that space-based plasma contactor experiments be conducted, in addition to the ground-based tests mentioned above. It is possible that results obtained from these space experiments may differ substantially from those measured in the laboratory. The laboratory results can, however, be used to identify phenomena that will probably be important in space, and they can serve to calibrate numerical models of the contacting process that can reflect the effects of magnetic fields, spacecraft motion, and accurate ionospheric properties.

REFERENCES

1. Purvis, C.K., and R.O. Bartlett, "Active Control of Spacecraft Charging," Progress in Astronautics and Aeronautics, Vol. 71, H.B. Garrett and C.P. Pike, Eds., AIAA, New York, 1980, pp. 299-317.

2. Olsen, R.C., C.E. McIlwain, and E.C. Whipple, "Observations of Differential Charging Effects on ATS 6," J. of Geophysical Research, Vol. 86, No. A8, 1981, pp. 6809-6819.

3. Martinez-Sanchez, M. and D.E. Hastings, "A Systems Study of a 100 kW Tether, J. of Astro. Sciences, V. 35, 1987, pp.75-96.

4. Friedly, V.J. and P.J. Wilbur, "High Current Hollow Cathode Phenomena," AIAA paper 90-2587, July 18-20, 1990.

5. Williams, J.D. and P.J. Wilbur, "Experimental Study of Plasma Contactor Phenomena," J. of Spacecraft and Rockets, Vol. 27, No. 6, Nov.-Dec. 1990, pp. 634-641.

6. Patterson, M.J., and R.S. Aadland, "Ground-based Plasma Contactor Characterization," appears in "Space Tethers for Science in the Space Station Era," L. Guerriero and I. Bekey, eds., Societa Italiana Di Fisica, Vol.14, Venice, Italy, Oct.4-8, 1987, pp. 261-268.

7. Vannaroni, G., et. al., "Experimental Characterization of Hollow-Cathode Plasma Sources at Frascati," appears in "Space Tethers for Science in the Space Station Era," L.Guerriero and I.Bekey, eds., Societa Italiana Di Fisica, Vol. 14, Venice, Italy, Oct. 4-8 1987, pp. 254-260.

8. Hershkowitz, N., "Review of Recent Laboratory Double Layer Experiments," Space Science Reviews, Vol. 41, 1985, pp. 351-391.

9. Guyot, M., and Ch. Hollenstein, "Experiments of Potential Gradients in a Current-Carrying Plasma. I. Potential Structures," Phys. Fluids, V. 26, No. 6, 1983, pp. 1596-1605.

10. Baker, K., et. al., "Studies of Strong Laboratory Double Layers with Computer Simulation," J. Plasma Physics, V. 26, Part 1, 1981, pp. 1-27.

11. Borovsky, J., and G. Joyce, "The Simulation of Plasma Double Layer Structures in Two Dimensions," J. of Plasma Physics, V. 29, Part 1, 1983, pp. 45-84.

12. Leung, P., A. Wong, and B. Quon, "Formation of Double Layers," Phys. Fluids, V. 23, No. 5, 1980, pp. 992-1004.

13. Hatakeyama, R., Y. Suzuki, and N. Sato, "Formation of Electrostatic Potential Barrier Between Different Plasmas," Phys. Rev. Lett., V. 50, No. 16, April 18, 1983, pp. 1203-1206.

14. Smith, J., N. Hershkowitz, and P. Coakley, "Inflection-Point Method of Interpreting Emissive Probe Characteristics," Rev. Sci. Instrum., V. 50, No. 2, 1979, pp. 210-218.

15. Williams, J.D., "Electrodynamic Tether Plasma Contactor Research," appears in "Space Plasma Contactor Research-1987," P.J. Wilbur, ed., NASA CR-182148, Jan. 1988, pp. 1-59.

16. Gerver, M.J., D.E. Hastings, and M.R. Oberhardt, "Theory of Plasma Contactors in Ground-Based Experiments and Low Earth Orbit," J. of Spacecraft and Rockets, Vol. 27, No. 4, July/August 1990, pp. 391-402.

17. Katz, I. and V.A. Davis, "A Van der Waals-Like Theory of Plasma Double Layers," Phys. Fluids, Vol. B1, Oct. 1989, pp. 2121-2125.

18. Davis, V.A., I. Katz, M. Mandell, and D. Parks, "A Model of Electron Collecting Plasma Contactors," accepted by J. of Spacecraft and Rockets, preview paper dated Oct. 3, 1989.

19. Siegfried, D.E., and P.J. Wilbur, "A Model for Mercury Orificed Hollow Cathodes: Theory and Experiment," AIAA Journal, Vol. 22, 1984, pp. 1405-1412.

20. Davis, W.D., and H.C. Miller, "Analysis of Electrode Products Emitted by dc Arcs in a Vacuum Ambient," J. Appl. Phys., Vol. 40, No. 3, April 1969, pp. 2212-2221.

21. Tanberg, R., "On the Cathode of an Arc Drawn in Vacuum," Physical Review, Vol. 35, May 1930, pp. 1080-1089.

22. Brophy, J.R. and P.J. Wilbur, "An Experimental Investigation of Cusped Magnetic Field Discharge Chambers," Int'l Electric Propulsion Conference, IEPC 84-70, Tokyo, Japan, 1984.

23. Aston, G., and P.J. Wilbur, "Ion Extraction from a Plasma," J. Appl. Phys., Vol. 52, No. 4, 1981, pp. 2614-2626.

24. Beattie, J., "Numerical Procedure for Analyzing Langmuir Probe Data," AIAA Journal, V. 13, No. 7, 1975, pp. 950-952.

25. Boyd, R., "The Collection of Positive Ions by a Probe in an Electrical Discharge," Proc. Roy. Soc., V. 201A, 1950, pp. 329-347.

26. Williams, J.D., "Plasma Contactor Research-1989," P.J. Wilbur, ed., NASA CR-185212, Feb. 1990, pp. 1-54.

27. Chan, C., N. Hershkowitz, and K. Lonngren, "Electron Temperature Differences and Double Layers," Phys. Fluids, V. 26, No. 6, 1983, pp. 1587-1595.

28. Wei, R. and P. Wilbur, "Space-Charge-Limited Current Flow in a Spherical Double Sheath," J. of Appl. Phys., V. 60, No. 7, Oct. 1, 1986, pp. 2280-2289.

29. Bohm, D. "Minimum Ionic Kinetic Energy for a Stable Sheath," appears in The Characteristics of Electrical Discharges in Magnetic Fields, A. Guthrie and R.K. Wakerling, eds., McGraw Hill, New York, 1949, pp. 77-86.

30. Williams, J., P. Wilbur, J. Monheiser, "An Experimental Validation of a Phenomenological Model of the Plasma Contacting Process," appears in "Space Tethers for Science in the Space Station Era," L. Guerriero and I. Bekey, eds., Societa Italiana Di Fisica, V. 14, Venice, Italy, Oct. 4-8, 1987, pp. 245-253.

31. Hershkowitz, N., "How Langmuir Probes Work," appears in Plasma Diagnostics: Discharge Parameters and Chemistry, O. Auciello and D. Flamm, eds., V. 1, Academic Press Inc., New York, 1989, pp. 113-183.

32. Rapp, D. and Englander-Golden, P., "Total Cross Sections for Ionization and Attachment in Gases by Electron Impact. I. Positive Ionization," J. of Chem. Phys., Vol. 34, No. 5, 1965, pp. 1464-1479.

33. Williams, J.D., and P.J. Wilbur, "Ground-based Tests of Hollow Cathode Plasma Contactors," AIAA 89-1558-CP, Third Int'l Conf. on Tethers in Space, San Fransico, May 17-19, 1989, pp. 77-87.

34. Williams, J.D. "Plasma Contactor Research-1990," P.J. Wilbur, ed., NASA CR-187097, Jan. 1991, pp. 1-54.

35. Vannaroni G., et. al., "Data Analysis of Hollow Cathode Experiment to Support Electrodynamic Tether Applications", Istituto D. Fisica Dello Spazio Interplanetario, IFSI-89-16, Frascati, Italy, Sept. 1989.

36. Beattie, J.R., W.S. Williamson, J.N. Matossian, E.J. Vourgourakis, J.L. Burch, and W.C. Gibson, "High-Current Plasma Contactor Neutralizer System," appears in additional conference proceedings of the Third International Conference on Tethers in Space, San Fransico, May 1989, pp. 42-48.

37. Stenzel, R.L. and J.M. Urrutia, "Currents Between Tethered Electrodes in a Magnetized Laboratory Plasma," J. of Geophysical Research, Vol. 95, No. A5, 1990, pp. 6209-6226.

38. Anderson, J.R., "A Fourier Series Technique for Differentiating Experimental Data," Appendix C in NASA CR-182254, P.J. Wilbur, ed., Feb. 1989, pp. 67-79. See also Lanczos, C., Applied Analysis, Prentice Hall Inc., Englewood Cliffs, New Jersey, 1964, pp. 219-221.

39. Swift, J.D., and M.J.R. Schwar, Electrical Probes for Plasma Diagnostics, Elsevier Press, New York, 1970, p. 76.

40. Crawford F. "Modulated Langmuir Probe Characteristics," J. Appl. Phys., V. 34, No. 7, 1963, pp. 1897-1902.

41. Kasha, M.A., The Ionosphere and its Interaction with Satellites, Gordon and Breach, New York, 1969, pp. 9-29.

42. Sagdeev, R.Z., "The 1976 Oppenheimer Lectures: Critical Problems in Plasma Astrophysics. I. Turbulence and Nonlinear Waves," Rev. of Mod. Phys., V. 51, No. 1, Jan. 1979, pp. 1-9.

APPENDIX A

Langmuir, Emissive, and RPA Probes

Figure A-1 contains illustrative mechanical and electrical schematics of the diagnostic probes used to measure plasma properties. The Langmuir probe is shown in Fig. A-1a, and it is used to measure plasma densities and electron temperatures and energies. It is constructed of a 3.1 mm dia., stainless steel sphere which is attached to a conductive lead. This lead is shielded from the plasma by a quartz tube so that the only conductive surface exposed to the plasma is that of the sphere. The probe is operated by placing it in a plasma and recording the current which flows to it over a range of bias voltages. The resulting current/voltage data can then be used to determine plasma properties as described by Refs. [24,31]. Further details of this type of probe are provided in a separate section below.

Mechanical and electrical schematics of an emissive probe are shown in Fig. A-1b. The emissive probe was constructed by attaching the ends of a ~ 1 cm long, 76 μm dia tungsten wire to two conducting support wires which are insulated from one another and a surrounding plasma by a two-hole, alumina rod and some ceramic adhesive. The probe is operated by forcing about 1 A of current through the filament by adjusting the 25 Ω power pot shown on the right of Fig. A-1b. At this value (~ 1 A) the current J_H heats the filament to a white hot temperature (~ 2800 K) where it is typically able to emit as much electron current as it is collecting from the

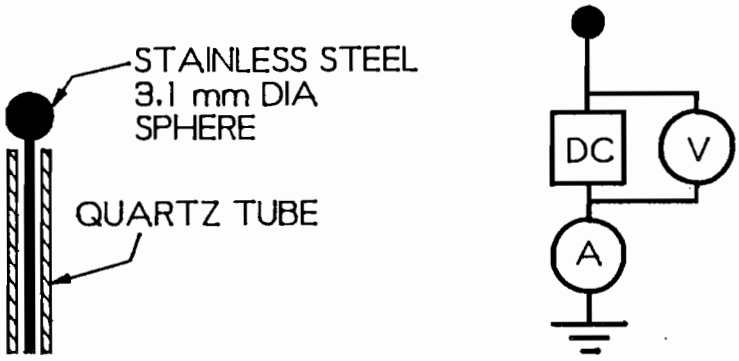

a. Langmuir Probe

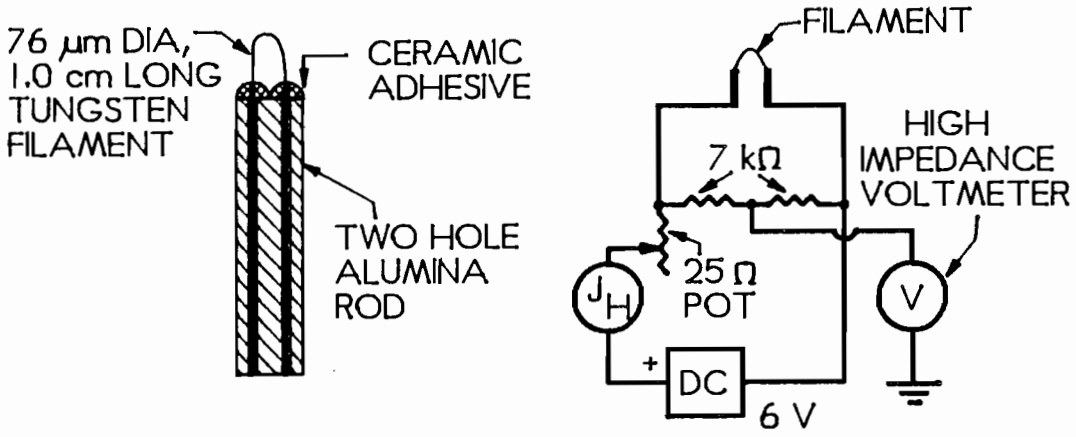

b. Emissive Probe

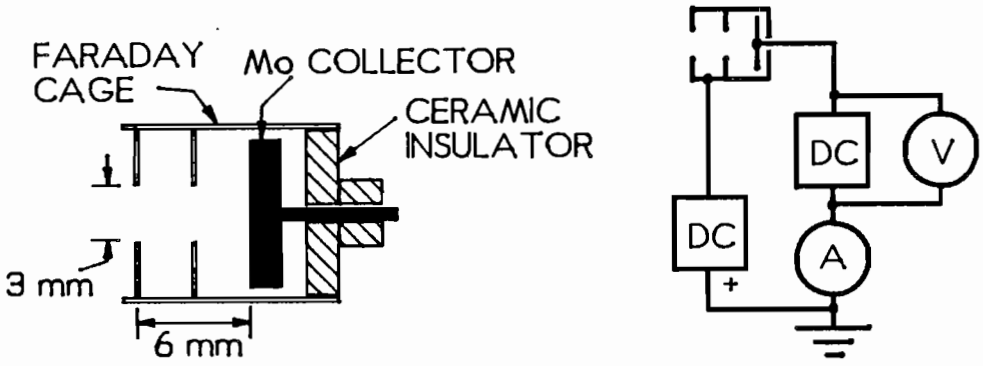

c. Retarding Potential Analyzer

Fig. A-1 Mechanical and Electrical Drawings of Emissive, Langmuir, and RPA Plasma Diagnostic Probes

surrounding plasma. At a sufficiently hot temperature, it will "float" close to plasma potential, and this floating potential can be measured with the high impedance voltmeter connected to the point between the two, 7 kΩ high precision resistors and a reference potential as shown in Fig. A-1b. By simultaneously recording the position and the potential of the emissive probe, plasma potential contours and profiles like the ones shown in Figs. 3-2 and 3-4 can be constructed. A more detailed discussion of this probe is also contained in a separate section below.

The retarding potential analyzer (RPA) is shown in Fig. A-1c. It consists of a molybdenum collector which is surrounded by a stainless steel Faraday cage. The Faraday cage is equipped with two, 3 mm dia orifices--the orifice diameter of 3 mm was selected to be smaller than the Debye length of the plasma in which the RPA is typically used. The Faraday cage was held about 40 V below the potential of the plasma in which it was immersed in order to repel any electrons from the Mo collector. The probe is operated by recording the ion current which flows to the collector under various bias conditions, and the resulting current/voltage data can be used to characterize the ion energy distribution [4,25]. One particularly useful application of the RPA involves the measurement of the current density of ions with temperatures/energies greater than ambient ones. This is accomplished by simply biasing the collector positive of the local plasma potential, recording the ion current to the RPA, and dividing this current by the orifice area of the Faraday cage. A more detailed description of the RPA similar to that for the Langmuir and emissive probes is included in a separate section below.

In general, fairly large errors are typically associated with the use of the plasma diagnostic probes listed above (i.e. 50% error levels are considered to be typical and acceptable). In addition, several data sets presented in the electron collection and emission sections and in this appendix indicate that sometimes plasma potential, plasma density, electron temperature, and ion emission current density data could be reproduced within only a factor of 2 in similar experiments conducted on different dates. However, these same quantities could be measured with relative errors of less than 10% between two separate tests made during the same, very carefully controlled experiment (both conducted on the same day, without exposing the experiment to the atmosphere). It is suggested on this basis that the trends indicated in specific experiments by these instruments are accurate. The following sections provide rough estimations of error levels and, in addition, describe some subtle details of Langmuir, emissive and RPA probes.

A. Langmuir Probe

Not only is it possible for plasmas to contain electrons and ions that are not in equilibrium with each other but, in addition, two different electron groups can co-exist under low effective collision rate and high input power conditions. This fact makes determination of plasma densities and electron temperatures/energies from Langmuir probe data difficult. Fortunately, however, most plasmas can be adequately described by using a simple model [24] which is based on the assumption that only two electron groups are present in the plasma. One group is modelled as Maxwellian, while the other one (the primary group) is assumed isotropic and mono-energetic. The procedure for analysis of Langmuir probe data measured in such a plasma

involves solving for the Maxwellian group temperature and density and the primary group energy and density using a non-linear, least-squares curve-fit to the portion of the Langmuir probe data in the electron retarding region. The specific equation which is fit can be written as follows

$$J_e = \frac{1}{4}\, e\, n_e\, A_p \sqrt{\frac{8\,k\,T_e}{\pi\, m_e}}\, \exp\left[\frac{e\,(V-V_p)}{k\,T_e}\right] + \frac{1}{4}\, e\, n_p\, A_p \sqrt{\frac{2\,e\,E_p}{m_e}}\, \left[1 + \frac{e\,(V - V_p)}{e\,E_p}\right] \qquad \text{(A-1)}$$

Equation A-1 is valid for probe potentials (V) between plasma potential and the potential at which all primary electrons are repelled.

This fitting technique was used to determine the plasma densities in the contactor plasma cloud and ambient plasma regions. However, Langmuir probe data can also be used to estimate the actual distribution function of the electrons presents in these plasmas. In order to estimate the electron energy distribution function directly in a relatively low density, isotropic plasma using a spherical Langmuir probe, it is necessary to compute the second derivative of its current/voltage characteristic curve. It is generally very difficult to differentiate experimental data twice without amplifying the inherent noise in it to the point where it dominates any useful information. However, when clean, smooth experimental data are obtained using a device with a very low-pass filter and averaging capabilities like those available on Keithley 617 or 237 programmable electrometers and special numerical

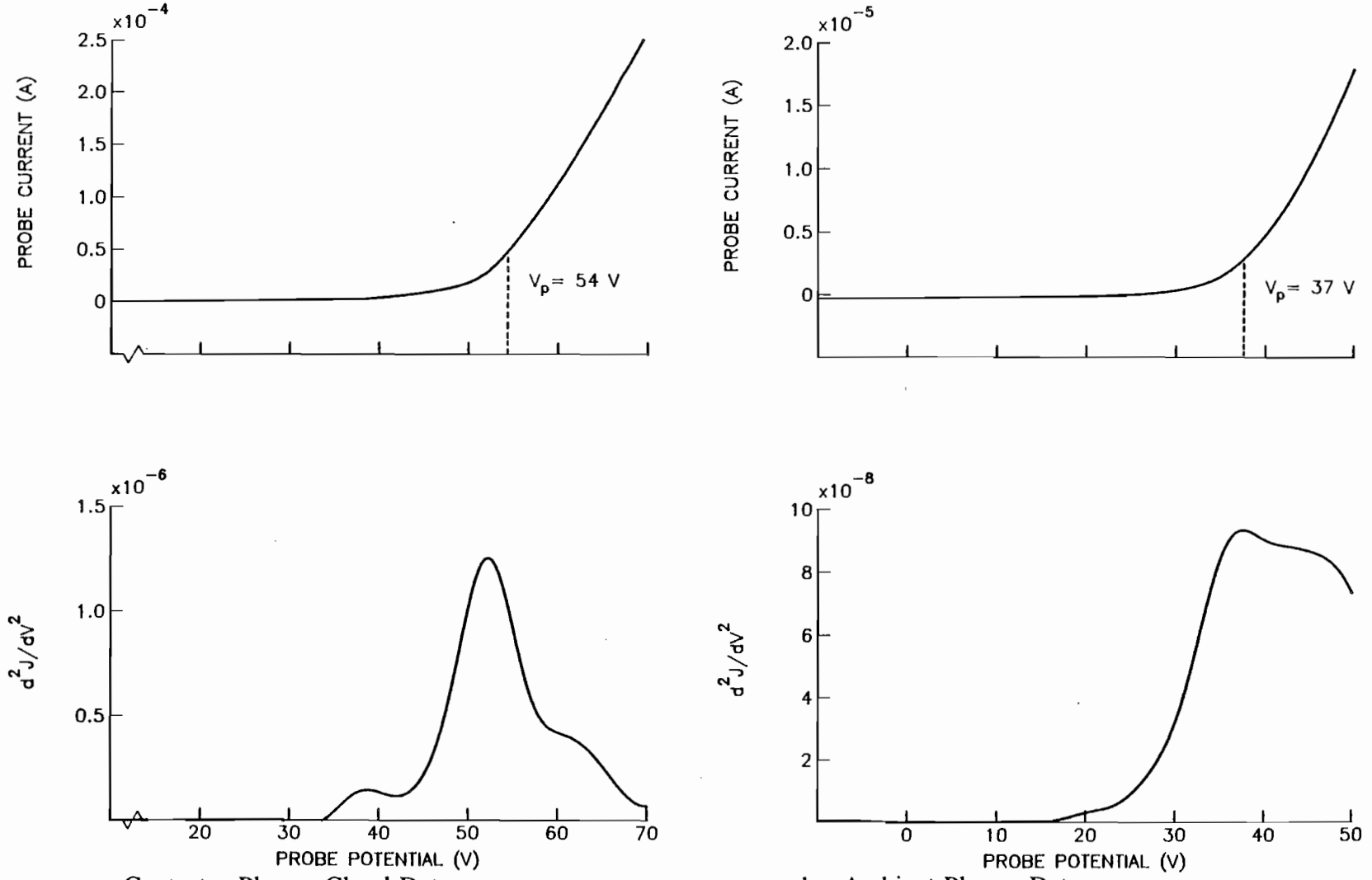

a. Contactor Plasma Cloud Data

b. Ambient Plasma Data

Fig. A-2 Langmuir Probe Current/Voltage Data Corresponding 2nd Derivatives

procedures are performed [38], realistic electron energy distributions can be generated.

A Langmuir probe trace typically consists of many discrete current/voltage data pairs [V_n, $J(V_n)$ -- n = 1, 2, ... , N] (equally-spaced in voltage). Figure A-2 shows two thick-sheath Langmuir probe traces, that are typical of those collected in the present experiments, constructed from plotting discrete current/voltage data sets. The probe voltage for these traces is referenced to the tank ground of the CSU facility, and they were measured in the contactor plasma cloud and ambient plasmas during a test in which a 50 mA electron current was being collected by the contactor from the ambient plasma. The trace obtained in the contactor plasma cloud contains features which suggest that a low-energy group (probably Maxwellian) and a higher energy group of electrons are present, while the trace corresponding to the ambient plasma appears to contain only one, low-energy group. These characteristics can be seen by examining the second derivative curves shown beneath the current voltage traces. The second derivative curves can be used along with plasma potential measured by an emissive probe to compute the electron energy distribution function [39] using the equation

$$F(E) = \frac{2^{3/2} m_e^{1/2}}{e^{3/2} A_p} \sqrt{V_p - V} \; \frac{d^2 J}{dV^2} \qquad \text{(A-2)}$$

In Eq. A-2, E is defined as the electron energy expressed in eV. It is noted that Eq. A-2 gives F(E) in units of [m^{-3} V^{-1}], however, values were typically normalized with respect to the maximum value of F(E).

In order to obtain the second derivative required in Eq. A-2, the discrete data points in a Langmuir probe trace were modified using the following procedure. First, a straight line, which connects the two end points of the trace, was subtracted from the data set:

$$y = J(x) - \frac{(J(V_N) - J(V_1))}{V_N - V_1} (V_N - x) \tag{A-3}$$

In Eq. A-3, x and y represent potential and modified current, respectively. The x and y data pairs are next represented as a continuous function (a Fourier sine series which was found using a least-squares fit)

i.e.

$$y \approx \sum_{j=1}^{m} A_j \sin\left[\frac{2\pi j x}{V_N - V_1}\right] \tag{A-4}$$

The number of terms in the series (m) was chosen to be half of the number of points in the data set (N) in order to avoid aliasing. Finally, the coefficients of the sine series were multiplied by the following convergence factor given by Lanczos [38]

$$B_j = \left[A_j \frac{\sin(\frac{j\pi}{N})}{\frac{j\pi}{N}}\right]^2 \tag{A-5}$$

The new sine series composed of the B_j coefficients can be differentiated analytically. Finally, the overall procedure can be repeated to obtain the second derivative required in Eq. A-2.

Figure A-3 contains two electron energy distribution functions which correspond to the Langmuir probe traces shown in Fig. A-2 that were normalized to their most probable value. When the Langmuir probe traces were analyzed using traditional techniques, they exhibited a temperature of about 3 to 4 eV for the low-energy (Maxwellian) electron groups. However, the most probable energy of both distributions is about 3.5 eV and this value is higher than expected (if the low-energy group electrons were Maxwellian, this result suggests that their temperature would be about 2 * 3.5 eV = 7 eV). Distributions can also be characterized by their full-width, half-maximum (FWHM) value. Those shown in Fig. A-3 display FWHM values of 7 to 8 eV and these correspond to Maxwellian distribution temperatures of 3.9 to 4.5 eV (i.e. $T_e \sim$ FWHM/1.8). This latter result agrees rather well with the Langmuir probe analysis temperature estimates of 3 and 4 eV.

The use of the Lanczos convergence factor is equivalent to smoothing the experimental data, and it causes smoothing errors. In addition, errors caused by inaccuracies in plasma potential measurements and natural rounding of the Langmuir probe trace near plasma potential in a noisy plasma probably introduce some inaccuracies into the electron distributions functions. Although these errors reduce the accuracy of the computed distribution functions, the procedure outlined above does provide useful, qualitative estimates of electron energy distributions.

It is noted here that the data in Fig. 3-4c show the Maxwellian electron temperature rises in the contactor plasma cloud region as the double layer boundary is approached. The same result was observed in separate plasma contactor experiments performed at IFSI and described in Ref. [34]. This rise in electron temperature is

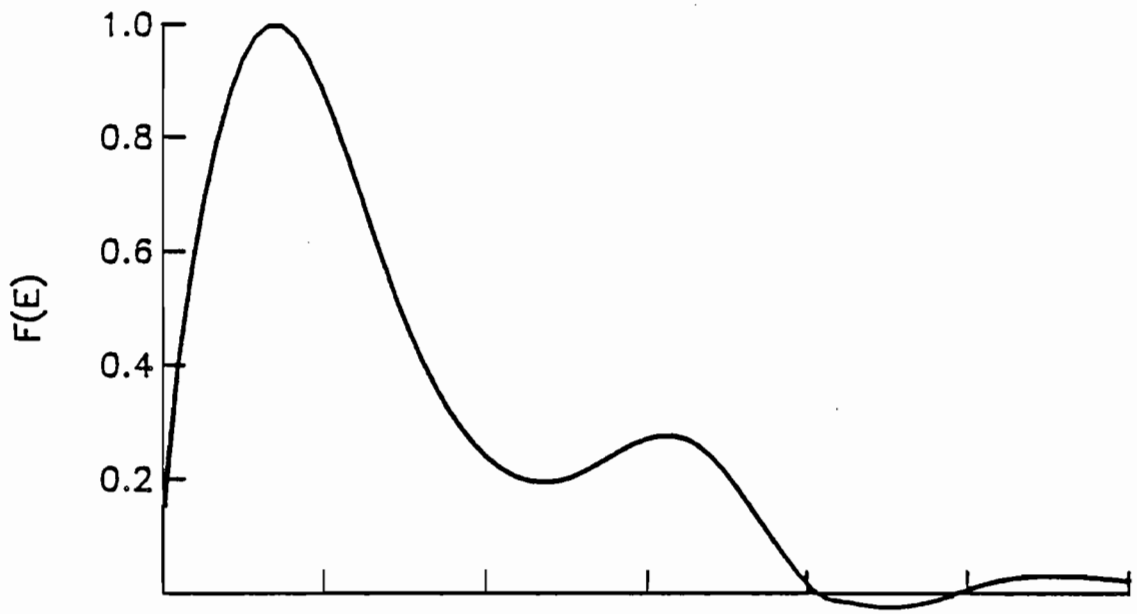

a. Contactor Plasma Cloud Data

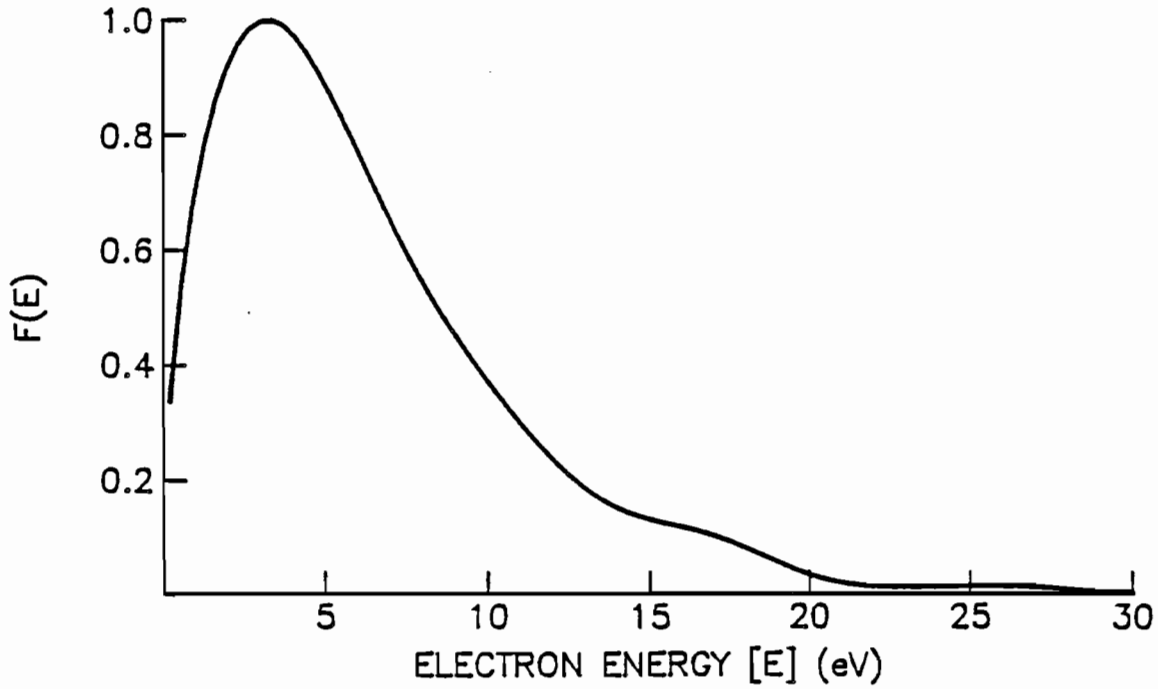

b. Ambient Plasma Data

Fig. A-3 Electron Energy Distribution Functions Measured in the Contactor Plasma Cloud and Ambient Plasmas

consistent with observations made in double layer experiments which were conducted in triple plasma devices [8,9]. It is possible that electron heating is occurring near the double-layer boundary possibly as a result of turbulent interactions between the high energy and Maxwellian electrons present in the contactor plasma cloud. Indications of higher electron temperatures could also be due to an error in the Langmuir probe analysis program that becomes significant when the high energy electron signal begins to dominate the colder electron group signal at locations close to the double layer boundary.

As mentioned previously, noisy plasmas can cause large errors to occur in Langmuir probe estimates of plasma properties. In order to estimate the noise level present in the contactor plasma cloud and ambient plasmas, the root-mean-square fluctuation level in the current flowing to the Langmuir probe (when it was held at plasma potential) was divided by the time-averaged value. Typically, 0.2 and 0.3 noise intensity levels were measured and they suggest that the ambient plasma was indeed noisy (i.e. plasma potential, density, etc. were fluctuating randomly with time), and according to Crawford [40] this noise could cause errors in the plasma properties which were determined from time-averaged Langmuir probe traces. Specifically, over-estimates of the plasma density by factors of 2 or more are likely. The Langmuir probe traces were measured using either a Keithley Programmable Electrometer 617 that was controlled by a mini-computer or a ranging ammeter used in series with an X-Y recorder. These instruments filtered out high frequency noise from the Langmuir probe signal and density data like those shown in Fig. 3-3 could be reproduced within a factor of 2 from similar experiments conducted on different

dates, and within 10% in separate, very carefully controlled experiments conducted on the same day as mentioned previously. In addition, similar noise levels (about 0.2) have been reported by Guyot and Hollenstein [9] in experiments investigating double layer phenomena that included plasma density data. In view of these experimental results and the level of precision in the present experiments, it is suggested that the relative values of plasma density can be used to understand trends observed with changing contactor conditions, and that absolute densities are accurate to at least the order of magnitude level.

The procedure applied to determine the current of streaming electrons to the Langmuir probe when it was placed in the highly non-equilibrium, plasma expansion region downstream of an electron emitting plasma contactor utilized distribution functions obtained in the manner described above. Recall that the streaming electron current [J_{str}] is defined to be the saturation electron current flowing to the Langmuir probe minus the current due to low energy (possibly Maxwellian) electrons present in the plasma expansion region. The fraction of current due to streaming and Maxwellian electrons can be found by first finding a good fit for the Maxwellian distribution, and then subtracting it from the total distribution to obtain an approximate description of the high energy electron group. Once the high energy and Maxwellian electron groups are separated, direct integration of the products of the distribution functions and the square root of the electron energy gives an estimate of the relative fraction of current due to each group.

B. Emissive Probe

As mentioned previously the emissive probe is operated by first heating it to a white hot temperature. At this high temperature, it can easily emit an electron current equal to the random electron current it collects from the plasma in which it is immersed. This heating current generally induces a 1 to 2 V potential drop across the ~1.0 cm long filament. Once the probe is sufficiently hot, the high impedance voltmeter is used to measure the potential of the filament with respect to some convenient reference potential. This technique of measuring plasma potential is termed the floating point method. In general, however, the emissive probe floats at a potential below true plasma potential by an amount that is sensitive to the probe temperature and the plasma density. In the case of the relatively low plasma densities investigated here, the potential difference between the true plasma potential and the probe floating potential is typically small and lower plasma densities reduce the error. In order to determine the magnitude of this error, the emissive probe was placed in a relatively high density plasma ($n_e \sim 1x10^9$ cm^{-3}) and the high impedance voltmeter in Fig. A-1b was replaced with a system capable of biasing it over a range of voltages and measuring the net current to it. This system could be used measure the current/voltage characteristic curve for the emissive probe just as it would for a Langmuir probe. When the filament was cold ($J_H < 0.5$ A), the typical Langmuir probe trace shown in Fig. A-4 as the solid curve was obtained. This curve displays a floating potential of 4.3 V--the potential at which the electron and ion currents collected by the probe from the plasma are equal. The solid curve begins to saturate between 11 and 14 V, and this feature provides as estimate of plasma potential.

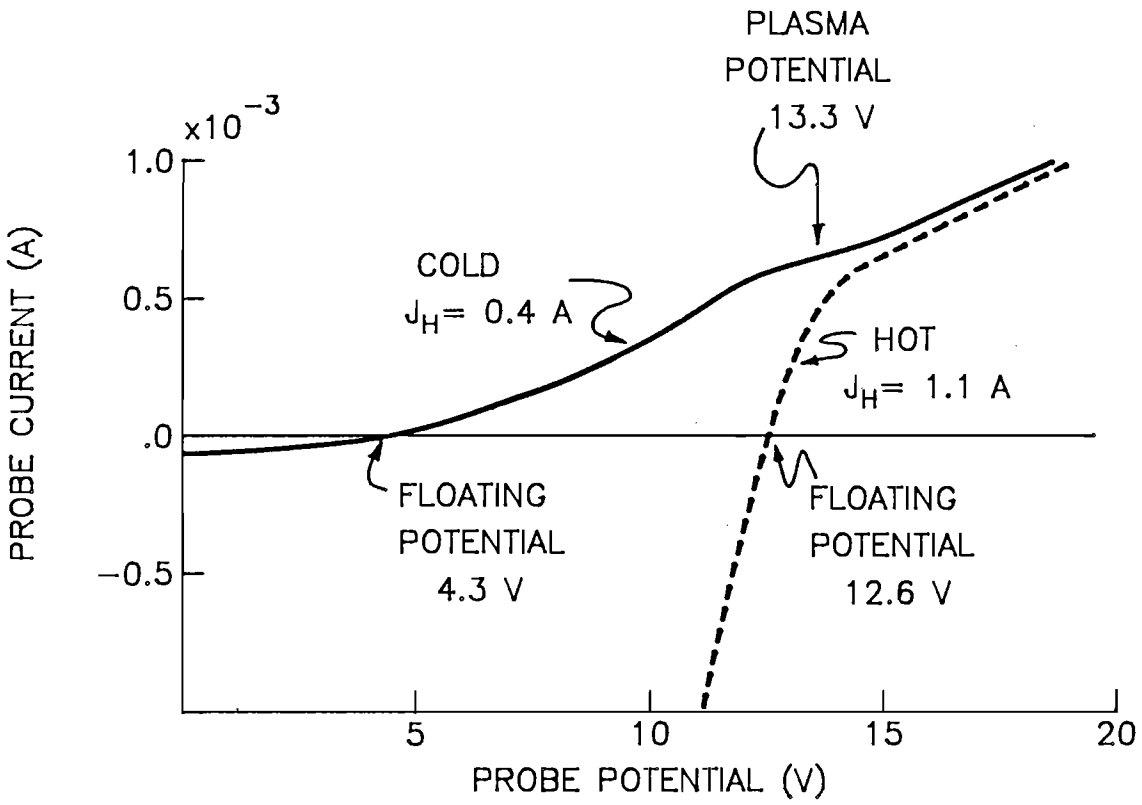

Fig. A-4 Current/Voltage Characteristic Curves for Cold and Hot Emissive Probes

Unfortunately, the electron current collected on the small diameter probe filament at potentials above plasma potential does not saturate completely and, consequently, this estimate is therefore inadequate.

When the filament was heated by passing a 1.1 A current through it, the dotted curve was obtained. It displays a floating potential of 12.6 V--the potential where the electron current emitted from the probe matches the net electron current collected from the plasma. It is important to note that the electron currents collected by the emissive probe when it is held at potentials above plasma potential are nearly the same for both the hot and cold conditions. This occurs because the electrons which are being "boiled" off the hot emissive filament have insufficient kinetic energy to escape from it and flow to the more negative surrounding plasma. However, when the hot emissive probe is held at potentials below plasma potential, it readily emits an electron current that exceeds the random electron current flowing from the plasma to the probe. The hot and cold traces begin to separate at a potential near 13.3 V and this potential is taken to be a good estimate of plasma potential. An error of about 0.7 V exists between this measure of plasma potential and the floating potential of the hot probe at this plasma density condition.

C. Retarding Potential Analyzer

Figure A-5 displays a typical RPA curve that was measured when the RPA was positioned in the ambient plasma (at Z=20 cm) and sighted at the contactor for the data shown in Fig. 3-4 together with its corresponding derivative . The RPA curve and corresponding derivative indicate that two groups of ions are present. The first group induces the peak occurring near 35 V in the lower plot and represents low

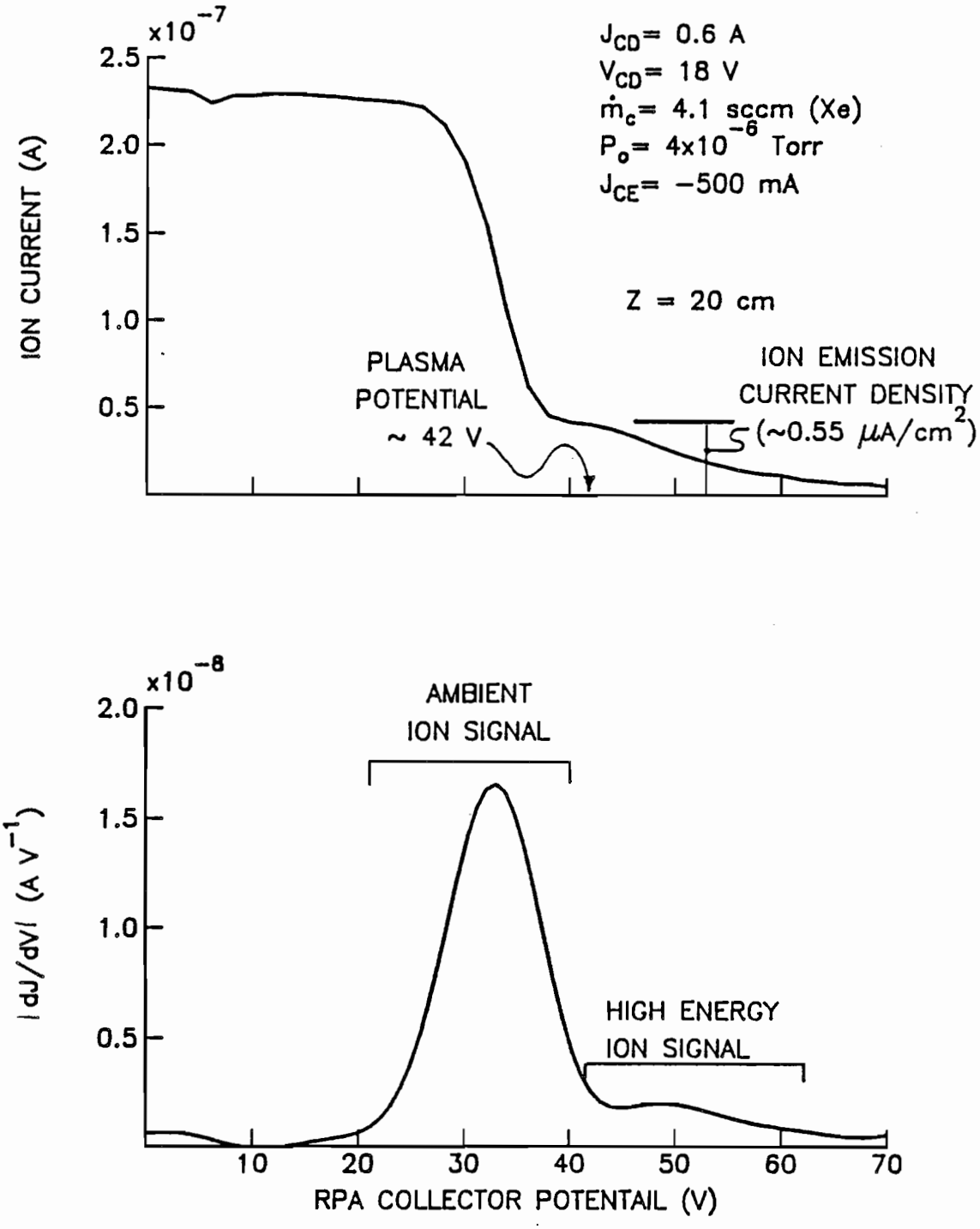

Fig. A-5 Retarding Potential Analyzer Current/Voltage Curve Along with its Corresponding Derivative

energy, thermal ions present in the ambient plasma. Note that plasma potential in the vicinity of the RPA was about 40 V, and when the RPA collector potential was greater than this potential most of the ambient ions could not reach the collector. A second group of ions is also present which extends from 45 to 65 V. It is postulated that these higher energy ions are created in the contactor plasma cloud and that they are accelerated from there through the double layer and into the ambient plasma where they are detected. The ion emission current density (j_+) of 0.55 $\mu A/cm^2$ was calculated by measuring the ion current flowing to the RPA collector when it was held slightly positive of plasma potential and dividing by the RPA Faraday cage aperture area. It is noted, however, that Fig. 3-12 indicates an ion emission current density of about 2 $\mu A/cm^2$ which was measured at a condition similar to the one corresponding to Fig. A-5. It is about 4 times higher than the one indicated in Fig. A-5. This relatively large difference is caused in part by slightly different axial positions of the RPA, and when this is taken into account the ion emission current densities agree to within a factor of 2. This is consistent with the level of error expected between two similar experiments conducted at different times as mentioned earlier.

APPENDIX B

Comparison of Typical Laboratory and LEO Plasma Conditions

The ranges of plasma conditions in typical laboratory ambient plasmas and in low Earth orbit (LEO) at about 400 km [41] are listed in Table B-1 in order to stimulate discussion of ionospheric simulation. The ambient plasma density within the laboratory is typically several orders of magnitude higher than space plasma conditions, and it was dependent upon the current being emitted or collected by the contactor. Although this is unfortunate from the point of view of accurate simulation, these relatively high plasma densities correspond to small Debye lengths (~ 1 cm) and this helps to shield out the effects of the vacuum tank wall on the experiment. In addition to higher ambient plasma densities, higher electron temperatures were typically measured in the laboratory. Although this difference also suggests poor simulation conditions, these higher electron temperatures were fortunate because they increase the ion production rate throughout the ambient plasma and help make it more uniform.

The ambient neutral pressure (and the neutral density) is also much higher in the laboratory than in LEO. However, the total inelastic mean-free path between the ambient electrons and the xenon atoms is still very large in the laboratory (about 1 km which is much larger than the chamber dimension). It is noted that the electron plasma frequency corresponding to the laboratory conditions can be as high as

Table B-1 Comparison of Laboratory and LEO Plasma Conditions

	LABORATORY CONDITIONS	LOW EARTH ORBIT CONDITIONS
Plasma Density n_{eo}	$5x10^6$ to $3x10^8$ cm^{-3}	$1x10^4$ to $1x10^6$ cm^{-3}
Electron Temp. T_{eo}	3 to 6 eV	0.1 to 0.2 eV
Ambient Pressure P_o	$5x10^{-6}$ Torr ($7x10^{-4}$ Pa)	$1x10^{-9}$ Torr ($1x10^{-7}$ Pa)
Ambient Temp. T_o	~300 K	~1000 K
Ambient Density n_o	$1.6x10^{11}$ cm^{-3}	$1x10^7$ cm^{-3}
Mag. Field Strength	0 to 1.6 G	0.4 G

90 MHz, and this number can be used to calculate an effective collision frequency of 0.9 MHz due to ambient electrons interacting with turbulent electrostatic waves (ion acoustic turbulence)--~0.01 times the electron plasma frequency [42]. This effective collision frequency can in turn be used to compute an effective ambient electron mean-free-path of ~2 m, which is comparable to the vacuum tank dimensions but still large compared to the contactor plasma cloud size.

The neutral temperatures indicated in Table B-1 are comparable. However, it is noted that the neutral background in the laboratory tests was mostly xenon while in LEO it is atomic oxygen.

Finally, the magnetic field within the CSU stainless steel vacuum chamber was ~0.4 G and it was oriented nearly transverse to a line joining the contactor and simulator. In separate tests conducted at IFSI [34], the magnetic field could be varied between zero and 1.6 G and oriented either transverse to or axial along a line joining the contactor and simulator. Although the experiments were conducted under the presence of magnetic fields comparable to those in LEO, the magnetic field was not moving relative to the contactor plasma cloud as it will be in LEO applications.

APPENDIX C

Nomenclature

$B_{//}$ Axial magnetic field strength--component along the line joining the contactor and the simulator (G)

$B_{\perp}$ Transverse magnetic field strength--component perpendicular to the line joining the contactor and the simulator (G)

e Magnitude of electronic charge (1.602×10^{-19} C)

J_{CD} Contactor discharge current (A)

J_{CE} Electron current emitted by contactor (A)

J_H Emissive probe heating current (A)

J_p Ion current at r_e due to ions produced between r_e and r_B which flows from the potential hill region to the cathode (A)

J_{SD} Simulator discharge current (A)

J_{SE} Electron current collected by simulator (A)

J_{SF} Simulator filament cathode heating current (A)

J_+ Ion current at r_A due to ions produced between r_B and r_A which flow from the potential hill region to the downstream boundary (A)

J_{+p} Ion current produced within the contactor plasma cloud (by streaming electrons) which flow through the double layer and into the ambient plasma (A)

j_+ Current density of high energy ions flowing from the vicinity of the contactor to regions downstream of it (A m^{-2})

j_o Non-dimensional current parameter (from Wei and Wilbur, 1986)

k	Boltzmann's constant (1.38×10^{-23} J K^{-1})
$\dot{m}_c$	Flowrate of neutrals supplied to contactor (sccm [Xe]--standard cubic centimeters per minute)
m_e	Mass of electron (9.11×10^{-31} kg)
m_p	Mass of ion (xenon: 2.18×10^{-25} kg)
$\dot{n}$	Neutral atom supply rate (from hollow cathode) (s^{-1})
n_e	Electron density (m^{-3})
n_{ei}	Electron density in the contactor plasma cloud near the double layer boundary (m^{-3})
n_{eo}	Electron density in ambient plasma (m^{-3})
n_o	Neutral atom density (m^{-3})
n_p	Density of ions on the cathode side of the potential hill [i.e. those that flow toward the cathode] (m^{-3})
n_+	Density of ions on the downstream side of the potential hill [i.e. those that flow toward the downstream boundary] (m^{-3})
P_o	Ambient pressure measured far from the hollow cathode (Pa)
$R(r)$	Volumetric production rate of ions at radius r (s^{-1} m^{-3})
r	Radius measured from the hollow cathode (m)
r_1	Radius measured from the hollow cathode (used as a dummy integration variable) (m)
r_A	Radial position of the spherical shell at the downstream boundary (i.e. at the base of the potential hill) (m)
r_B	Radial position of the potential hill peak (or crest) (m)
r_e	Radial position of the spherical shell boundary from which electrons are supplied (m)
r_i	Radial position of the inner boundary of the double layer (m)
r_o	Radial position of the outer boundary of the double layer (m)

T_{ei} Electron temperature in contactor plasma cloud near the double layer boundary (eV or K)

T_{eo} Electron temperature in ambient plasma (eV or K)

T_o Neutral atom temperature measured far from the hollow cathode (K)

V Potential measured with respect to (wrt) the contactor cathode (V)

V_i Potential difference across double layer (V)

V_A Potential at r_A (wrt contactor cathode) (V)

V_B Potential at r_B, crest potential (wrt contactor cathode) (V)

V_C Bias supply voltage (wrt contactor cathode) (V)

V_{CD} Contactor discharge voltage, downstream boundary potential (wrt contactor cathode) (V)

V_{SD} Simulator discharge voltage (wrt simulator cathode) (V)

v_e Electron velocity (m s^{-1})

v_{oc} Velocity of neutrals flowing from the hollow cathode (m s^{-1})

Z Axial position measured from the contactor cathode along the tank/contactor centerline (m)

Greek symbols:

α Normalized Current Ratio (from Wei and Wilbur, 1986)

$\Delta\phi$ Non-Dimensional Double Layer Strength ($=eV_i/kT_{ei}$)

δ Position where ions created by streaming electrons will recombine on contactor surfaces rather than migrate to the contactor plasma cloud/double layer boundary (order of 0.01 m) (m)

ε_o Permittivity of free space (8.85×10^{-12} F m^{-1})

γ Bohm Pre-Sheath Correction Factor

ψ Solid angle of the spherical sector through which electron collection or emission occurs (steradian)

ψ_o Solid angle of the spherical sector through which neutral atoms expand as they exit the orifice of the hollow cathode (steradian)

σ_+ Electron/Neutral atom ionization cross-section (m^2)

Langmuir Probe Analysis Variables and Definitions:

A_p Surface area of spherical Langmuir probe- CSU probe: 3.1×10^{-5} m^2

E Electron energy (eV)

E_p Primary (or mono-energetic) electron energy (eV)

F(E) Electron energy distribution function (Normalized)

J_{sat} Electron current flowing to a 3.1 mm dia., spherical Langmuir probe being held at plasma potential (A)

n_e Maxwellian electron density (cm^{-3})

n_p Primary (or mono-energetic) electron density (cm^{-3})

T_e Maxwellian electron temperature (eV or K)

V_P Plasma potential measured by emissive probe (V)

IFSI Acronym for Istituto di Fisica dello Spazio Interplanetario of the Consiglio Nazionale Delle Ricerche of Italy

CSU Acronym for Colorado State University

LeRC Acronym for Lewis Research Center of the National Aeronautics and Space Administration